ADVANCED ENERGY MATERIALS
www.advenergymat.de

Fabrication of Composite Cathode for All-Solid-State Sodium Batteries

Gaoming Sun, Yuan Ma, Hehe Zhang, Shengan Wu, Shiyong Chu, Stefano Passerini,* and Yanjiao Ma**

All-solid-state sodium-ion batteries (ASSSBs) are regarded as highly promising candidates for large-scale energy storage systems owing to their expected lower cost and enhanced safety. In recent years, the advent of novel fast ion-conducting solid electrolytes (SEs) has further accelerated the rapid development of this field. Nevertheless, several critical challenges remain, preventing the performance of ASSSBs from surpassing that of their liquid-electrolyte counterparts. Among these, a key obstacle lies in the design of cathode systems that ensure optimal compatibility between the SE and the cathode active material (CAM). This review focuses on the essential properties and persistent challenges of CAM in ASSSBs employing inorganic SEs and highlights the current strategies developed to address these issues. Particular attention is given to the design considerations at the cathode, particle, and interface levels, including aspects related to the microstructure, mechanical integrity, and (electro)chemical interactions with the SE. Finally, the review outlines future directions and design principles for the development of next-generation cathode materials in ASSSBs.

1. Introduction

With the development of lithium-ion electrode materials approaching their theoretical performance limits, and in light of the growing demand for enhanced safety, higher energy density, and reduced cost, there has been a growing research focus on exploring and developing alternative battery systems based on more abundant and widely available resources.[1,2]

Among the various emerging battery technologies, sodium-ion batteries (SIBs) have been identified as a promising alternative to mitigate the challenges posed by lithium resource scarcity. This is primarily due to the high relative abundance of sodium in the Earth's crust (2.75%) and its physicochemical properties, which closely resemble those of lithium. Sodium is the lightest alkali metal after lithium and has a low electrode potential (−2.71 V vs Standard Hydrogen Electrode, SHE).[3,4] Moreover, SIBs share similar structures and working principles with lithium-ion batteries (LIBs), enabling cost-effective development by leveraging the extensive experience gained from LIBs.[5] Compared to conventional liquid-electrolyte SIBs, ASSSBs employ solid electrolytes (SEs), which offer superior thermal stability and non-flammability, significantly reducing the risk of thermal runaway and enhancing overall battery safety.[6] Additionally, ASSSBs enable the use of sodium metal anodes and high-voltage cathode active materials (CAMs) to enhance energy density. The mechanical properties of SEs also effectively suppress the formation of alkali metal dendrites, thereby preventing short circuits and extending battery lifespan.

Unlike conventional, i.e., porous SIBs cathodes, SEs require an accurate mixing of with the CAM to construct a composite

G. Sun, H. Zhang, S. Wu, S. Chu, Y. Ma
School of Energy and Mechanical Engineering
School of Chemistry and Materials Science
Nanjing Normal University
Nanjing 210023, China
E-mail: yanjiao.ma@njnu.edu.cn

The ORCID identification number(s) for the author(s) of this article can be found under https://doi.org/10.1002/aenm.202503756

DOI: 10.1002/aenm.202503756

Y. Ma
Confucius Energy Storage Lab
Key Laboratory of Energy Thermal Conversion and Control of Ministry of Education
School of Energy and Environment & Z Energy Storage Center
Southeast University
Nanjing, Jiangsu 211189, China
E-mail: yuan.ma@seu.edu.cn

S. Passerini
Helmholtz Institute Ulm (HIU)
Helmholtzstrasse 11, 89081 Ulm, Germany
E-mail: stefano.passerini@ait.ac.at

S. Passerini
Karlsruhe Institute of Technology (KIT)
76021 Karlsruhe, Germany

S. Passerini
Austrian Institute of Technology (AIT) Transportation Technologies
Giefinggasse 4, Wien 1210, Austria

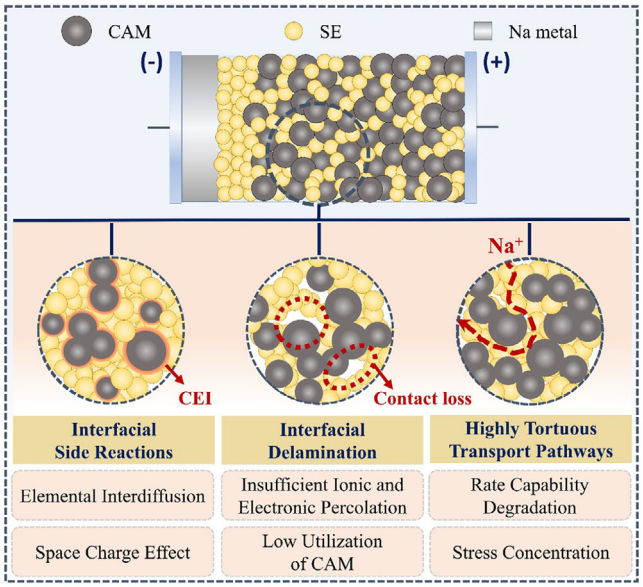

Figure 1. Interfacial issues in composite cathodes for ASSSBs.

cathode with an efficient ion transport network. Furthermore, composite cathodes incorporate conductive additives and binders to enhance electronic conductivity and maintain structural integrity, leading to the formation of multiple interfacial structures. Therefore, a major challenge lies in optimizing the internal structure and composition of the cathode to achieve stable interface architectures and efficient ion/electron transport networks (**Figure 1**).[7] Additionally, ensuring the homogeneous distribution and intimate contact of all the cathode components in a 3D framework remains a critical consideration.

Currently, commonly used SEs include oxides, sulfides, halides, complex hydrides, and polymeric SEs, each type exhibits distinct properties.[8] For instance, oxide SEs offer excellent electrochemical and chemical stability but suffer from high mechanical strength (i.e., high Young's modulus), which can lead to interfacial delamination from SEs. Additionally, their fabrication requires high-temperature sintering, which increases processing costs.[9] Sulfide SEs, on the other hand, benefit from the low electronegativity and large ionic radius of sulfur, which weaken the electrostatic interactions between the framework and Na, resulting in exceptionally high ionic conductivity, in some cases surpassing those of liquid electrolytes. Examples include Na_3PS_4 (NPS, $\sigma_{ion} > 1$ mS cm^{-1}), $Na_{2.88}Sb_{0.88}W_{0.12}S_4$ ($\sigma_{ion} = 32$ mS cm^{-1}), $Na_{11}Sn_2PS_{12}$ ($\sigma_{ion,\ 25°C} = 3.7$ mS cm^{-1}), and $Na_3SbS_{3.75}Se_{0.25}$ ($\sigma_{ion} = 4.03$ mS cm^{-1}), all of which meeting the fast charge/discharge requirements of batteries.[10–14] Furthermore, sulfides possess relatively soft mechanical properties, ensuring good physical contact with CAM. However, their narrow electrochemical stability window and poor chemical/electrochemical stability remain key challenges. Halide and complex hydride SEs exhibit relatively high ionic conductivities, but the latter's complex synthesis and high cost hinder large-scale applications.[15] In contrast to inorganic SEs, polymer SEs offer advantages such as mechanical flexibility, low density, and simple processing. However, their Na^+ conductivity at room temperature (RT) is typically in the range of 10^{-5} to 10^{-7} S cm^{-1}, which is insufficient for practical ASSSBs applications.[16]

CAMs for ASSSBs include conventional oxide-based materials (e.g., layered oxides and NASICON-type structures), sulfides, and organic compounds. In recent years, Prussian blue analogs (PBAs) and sulfide CAMs have also garnered significant attention.[17–19] Sodium-based layered transition metal oxides (Na_xMO_2, where M = Ni, Co, Mn, Fe, Cr, V, etc.) can reversibly host Na^+ while exhibiting high redox potentials and theoretical capacities. However, at high cut-off voltages, Na^+ extraction often induces phase transitions and structural changes, resulting in irreversible lattice collapse and accelerated capacity fading. Additionally, oxygen species (O_2, O_2^-, and O^-) released during structural collapse may chemically oxidize SEs. Metal sulfide (MS_x) has gained interest due to their high theoretical capacities and natural abundance, which stem from their multi-electron redox reactions. However, their large volume expansion, inherently low electronic conductivity, and sluggish Na^+ diffusion kinetics present challenges in achieving superior electrochemical performance. Organic CAMs, known for their resource abundance, environmental friendliness, and structural diversity, have also been explored for sodium storage applications. Nevertheless, several challenges remain, including the need for novel molecular structures and reaction mechanisms to enhance Na storage properties. In practical applications, the selection of CAMs must balance performance targets with cost considerations. For instance, layered oxide CAMs are suited for high-energy-density applications, sulfide CAMs are ideal for large-scale energy storage, and organic CAMs are promising for low-power and environmentally friendly storage solutions.

In summary, the wide range of available CAMs and SEs provides opportunities to design composite cathodes with tailored properties, enabling high-power and high-energy-density configurations. However, these combinations also give rise to a variety of interfacial challenges. To overcome these issues, numerous strategies have been proposed, including the optimization of intrinsic properties of CAMs (e.g., through doping and high-entropy approaches), the construction of stable interfaces, and the application of surface coating techniques.[20–25] This review systematically summarizes optimization strategies across multiple scales—from the atomic or sub-nanometer scale (e.g., material modification via doping and entropy tuning), to the nanometer scale (e.g., interfacial engineering via surface coatings), and the micrometer scale (e.g., composite cathode fabrication methods). The underlying mechanisms governing interfacial stability and electrochemical performance are elucidated, providing theoretical insights and practical guidance for the future design of high-performance solid-state cathode systems.

2. Inorganic Solid Electrolytes (SEs)

2.1. Fundamental Properties

As research on SEs progresses, numerous materials with high ionic conductivity have been developed (**Figure 2**). However, ASSSBs assembled using these SEs often exhibit subpar performance, including rapid capacity decay, significant voltage polarization, and low initial Coulombic efficiency. These performance

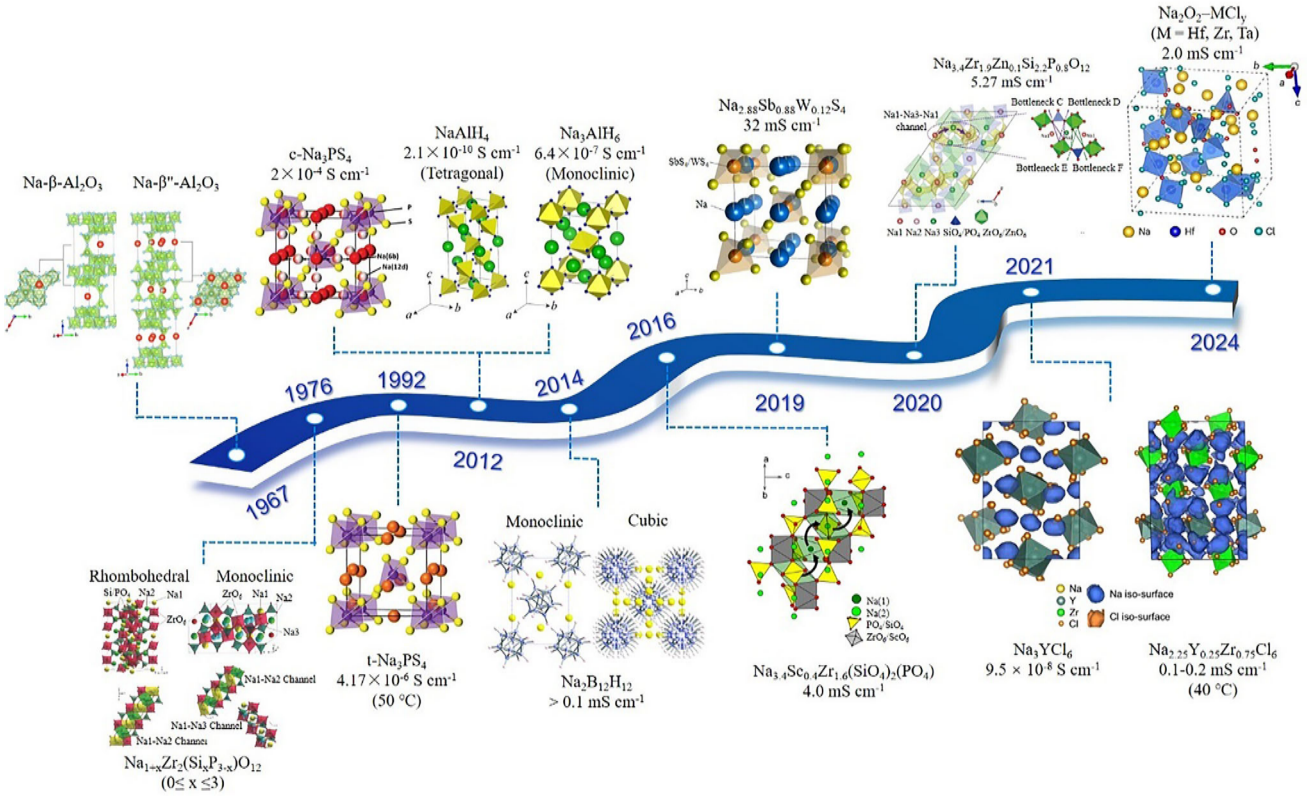

Figure 2. Development of solid-state Na^+ electrolytes.[4,9,11,12,28–37] (Reproduced with permission.[4] Copyright 2018, Wiley-VCH. Reproduced with permission.[37] Copyright 2023, Royal Society of Chemistry. Reproduced with permission.[33] Copyright 2014, Royal Society of Chemistry. Reproduced with permission.[9] Copyright 2016, American Chemical Society. Reproduced with permission.[34] Copyright 2020, American Chemical Society. Reproduced with permission.[32] Copyright 2012, American Institute of Physics).

issues are primarily attributed to the deteriorated migration dynamics of Na^+ at the electrode–electrolyte interface, leading to increased electrochemical impedance. The root cause of this unfavorable behavior lies in the interfacial incompatibility between the electrode and the SE. An ideal two-phase interface should be both thermodynamically stable and chemically compatible. Accordingly, SEs must exhibit not only high ionic conductivity and electrochemical stability but also sufficient mechanical strength to maintain intimate and stable contact at the interface.[26,27] Subsequently, the physicochemical properties of inorganic SEs are compared, as shown in Figure 9.

2.1.1. Na^+ Transport Mechanisms

In inorganic SEs, Na^+ transport primarily depends on the concentration of mobile Na^+ and the density of lattice defects.[10] At the atomic scale, this conduction process manifests as directional hopping of Na^+ along diffusion pathways within the anionic lattice framework, specifically involving transitions between ground-state stable sites and metastable intermediate sites.[38] Lattice defects—particularly Na vacancies and interstitial Na^+ generated through doping substitution—provide crucial migration pathways. Driven by chemical and electrochemical potential gradients, Na^+ achieve effective migration through these defect channels.[37]

These ionic hopping processes mainly occur through two distinct mechanisms: 1) single-ion migration, including vacancy migration and interstitial migration mechanism; and 2) multi-ion concerted migration (**Figure 3**a). The vacancy migration relies on vacancies created by Schottky defects, where Na^+ hop from their original equilibrium sites to adjacent vacancies, simultaneously generating new vacancies at their former positions (Figure 3b). The interstitial migration, based on Frenkel defects, can be further categorized into direct interstitial mechanism and interstitial knock-off mechanism (Figure 3c,d).[39] In the direct interstitial mechanism, interstitial ions—typically smaller than the host lattice atoms—jump directly between adjacent interstitial sites, forming interstitial solid solutions. In the interstitial knock-off mechanism, an interstitial ion displaces a neighboring lattice atom from its position and occupies it, while the displaced atom moves to another interstitial site.

Nevertheless, Na^+ transport in SEs predominantly occurs through the concerted migration.[40] This mechanism is typically observed in SEs with high sodium ion concentrations, involving the simultaneous hopping of Na^+ from both low-energy and high-energy sites to adjacent lattice positions. During this process, Na^+ at high-energy and low-energy sites may undergo "identity exchange," where the energy released by the former partially compensates for the energy required by the latter, thereby reducing the overall migration barrier.[41]

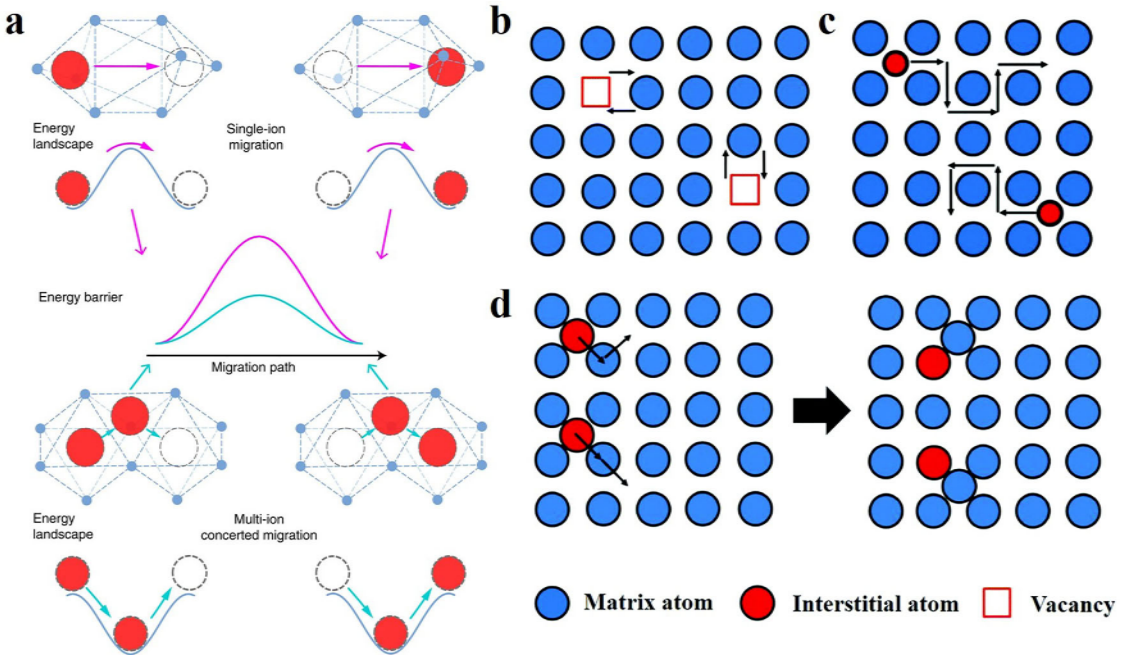

Figure 3. Schematic illustration of a) the energy barrier comparison between single-ion migration and multi-ion migration. Reproduced with permission.[41] Copyright 2017, Springer Nature. b) Vacancy mechanism, c) direct interstitial mechanism, d) interstitial knock-off mechanism. Reproduced with permission.[39] Copyright 2020, The Royal Society of Chemistry.

Na^+ conduction in SEs constitutes a complex multiscale process, influenced by both intrinsic material properties (crystal structure, defect concentration) and external conditions (temperature, electric field). A profound understanding of the physical nature of these conduction mechanisms provides essential theoretical guidance for designing novel high-performance SEs. Through precise regulation of lattice defects and ion distribution, more efficient Na^+ conduction can be achieved.

2.1.2. Ionic Conductivity

Ionic conductivity is a critical parameter for SEs, as it governs ion transport kinetics, reduces polarization during cycling, and supports efficient and stable battery operation. In inorganic SEs, ionic conductivity is mainly determined by defect types and concentrations, the density of mobile ions, and the ion diffusion energy barrier.[42] This relationship can be described by the equation: $\sigma = \sigma_0 \exp(-E_a/k_B T)$, where σ_0 represents the pre-exponential factor in the Arrhenius equation, encompassing parameters such as carrier concentration; E_a denotes the activation energy for diffusion, indicating the threshold required for effective ion diffusion; and k_B and T represent the Boltzmann constant and absolute temperature, respectively. Therefore, achieving high ionic conductivity requires an ample supply of mobile Na^+, accessible neighboring sites/defects, and a lower migration barrier.[29]

Experimentally, ionic conductivity can be measured using techniques such as solid-state nuclear magnetic resonance, quasi-elastic neutron scattering, and secondary ion mass spectrometry. Among them, electrochemical impedance spectroscopy (EIS) is the most widely used technique for evaluating ionic conductivity in inorganic SEs.[43,44]

2.1.3. Electrochemical Stability Window

The electrochemical stability window refers to the voltage range within which a SE remains chemically inert, undergoing neither oxidation nor reduction reactions. Understanding this stability window is crucial for guiding the selection of CAMs and determining the operational voltage of the battery. As illustrated in **Figure 4**, the oxidative stability of an electrolyte is typically described by the position of its highest occupied molecular orbital (HOMO) or valence band maximum (VBM). When the CAM chemical potential (denoted as μ_c) falls within this stability window, the system remains thermodynamically stable.[45,46] Conversely, if $\mu_c <$ HOMO (or VBM), electrons are transferred from the SE to the CAM, leading to oxidative decomposition of the electrolyte and the formation of a cathode electrolyte interphase (CEI).[45] The formation of the CEI indicates that a portion of Na^+ within the electrolyte participates in interfacial reactions, resulting in a reduction in the bulk ionic conductivity of the electrolyte. Simultaneously, the charge transfer resistance at the interface increases, both of which significantly contribute to the overall rise in the battery's electrochemical impedance. Moreover, if the CEI exhibits mixed electronic and ionic conductivity, continuous decomposition of the SE occurs, ultimately leading to mechanical instability and catastrophic performance degradation of the battery. It is important to note, however, that not all interphase formations are detrimental. In some cases, the CEI can function as a favorable ion conductor with high thermodynamic and kinetic stability. A favorable CEI is characterized by a uniform, dense

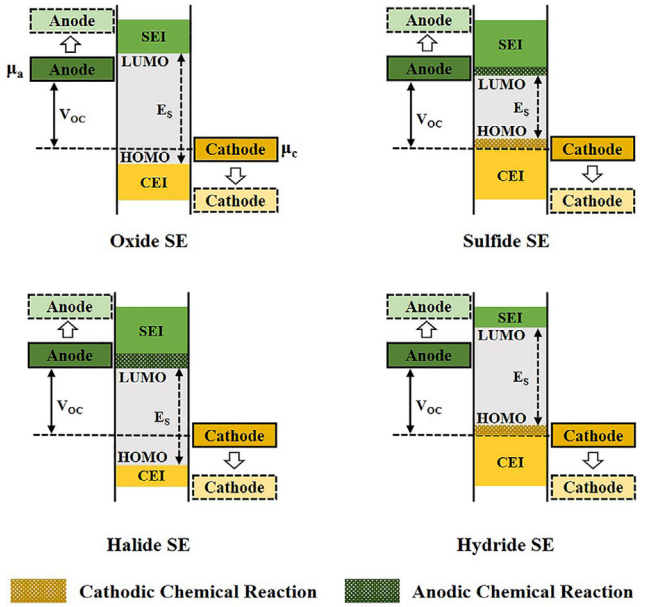

Figure 4. Schematic illustration of major inorganic Na^+-conducting SEs electrochemical stability windows and interphases formation processes.

interfacial layer that promotes efficient ion transport. If it is thermodynamically stable and electronically insulating, the interphase can passivate the SE, thereby extending its oxidative stability window.

The electrochemical stability window of SEs is typically evaluated using cyclic voltammetry (CV) or linear sweep voltammetry techniques in a blocking electrode configuration, with sulfide-based SEs serving as a representative example. CV tests utilizing blocking electrodes indicate that NPS possesses an electrochemical stability window of up to 5 V (vs Na^+/Na).[11] However, recent theoretical studies and experimental results based on NPS reveal that the anodic decomposition potentials are 2.3 and 2.7 V (vs Na^+/Na).[7,47] These CV tests may overestimate the electrochemical stability limits of the electrolyte due to several reasons: 1) Poor contact with the metal electrode or excessively rapid scan rates may cause the SE to remain in a non-equilibrium state during testing; 2) The limited electronic conductivity of the SE restricts decomposition reactions to very thin interfacial regions, making it challenging to observe the weak decomposition currents generated by slow kinetic processes; 3) The formed interfacial phases may exhibit passivation effects that broaden the electrochemical stability window. To address these issues, a mixed layer of SE and conductive carbon has been introduced between the blocking electrode and the Na^+-conducting SE. The addition of conductive carbon significantly increases the interfacial contact area between the SE and the electronic conductor, thereby enhancing the decomposition kinetics of the SE. As a result, the electrochemical stability window of SEs can be determined with greater accuracy.

The oxidative stability of SEs at high voltages is strongly dependent on the nature of the anionic species, which is primarily influenced by electronegativity and charge density.[48,49] Typically, the electrochemical stability is constrained by the anion with the lowest ionization potential, following the trend: halides > oxides > sulfides > nitrides. This ordering is consistent with the variations in charge density among N^{3-}, S^{2-}, O^{2-}, and Cl^-.[50,51]

2.1.4. Other Physical Properties

The mechanical properties and densification of SEs play a pivotal role in the fabrication and performance of ASSSBs. On the one hand, the ductility of SEs determines their ability to achieve densification through cold pressing at room temperature, thereby enabling improved compaction and enhanced electrode/electrolyte interfacial contact during processing. The Young's modulus is equally critical: oxide SEs with high Young's modulus often struggle to accommodate the stresses arising from volume fluctuations of CAMs during cycling, which may result in interfacial cracking, reduced contact area, and increased impedance. By contrast, sulfide SEs with lower Young's modulus exhibit greater mechanical compliance, allowing stress to be more effectively mitigated and interfacial stability to be preserved. On the other hand, both density and densification exert significant influence on the electrochemical performance of SEs. Density is an intrinsic material property, whereas densification reflects the extent of porosity elimination and compaction achieved during fabrication. Well-densified SEs, such as NASICON-type $Na_{1+x}Zr_2Si_xP_{3-x}O_{12}$ (NZSP) and β''-Al_2O_3, typically display low porosity and superior mechanical integrity, which collectively reduce grain boundary resistance, suppress dendritic penetration, and enhance overall ionic conductivity. For example, the cold sintering process has been employed to fabricate highly densified $Na_{3.4}Zr_{1.9}Zn_{0.1}Si_{2.2}P_{0.8}O_{12}$, enabling low-temperature processing while significantly improving ionic conductivity and interfacial stability.[52] It should be noted, however, that although higher densification levels help minimize porosity, excessively rigid microstructures may lack the adaptability required to accommodate electrode volume changes, thereby increasing the risk of interfacial failure. Furthermore, electrolyte design must also account for the effect of density on energy density: provided sufficient mechanical robustness and ionic conductivity are maintained, lower-density materials may offer potential advantages by reducing inactive mass and improving the gravimetric energy density of the battery system.

2.2. Oxide SEs

2.2.1. β-Alumina

Since their discovery in the 1960s, β-Al_2O_3 and β''-Al_2O_3 have been utilized as SEs for rechargeable high-temperature sodium-sulfur (Na-S) batteries due to their high ionic conductivity and favorable thermal properties.[28,53,54] As shown in **Figure 5b**, β-Al_2O_3 ($Na_2O(8\text{-}11)Al_2O_3$) possesses a hexagonal structure with $P6_3/mmc$ symmetry, while β''-Al_2O_3 ($Na_2O(5\text{-}7)Al_2O_3$) exhibits a rhombohedral structure with R-3m symmetry.[29,55] Both structures consist of alternating spinel blocks and conductive layers, where the spinel block is formed by the stacking of four layers of O^{2-} and Al^{3+}. The conductive planes comprise stacked oxygen and sodium ions, with the main differences arising from the stoichiometry and the stacking order of the O^{2-} in the conductive layers (Figure 5a).[16,56] Due to the highest Na^+ content in

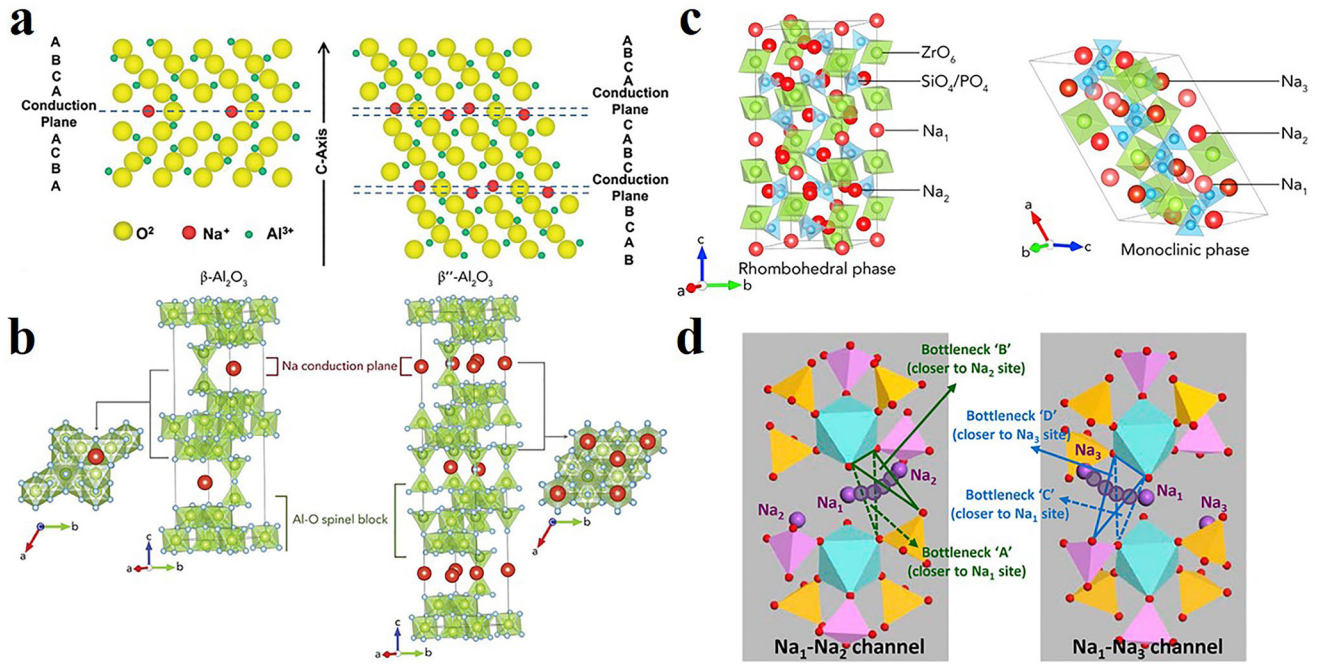

Figure 5. a) Schematic diagram of stacking sequence and Na^+ conduction plane for β-Al_2O_3 and β''-Al_2O_3. Reproduced with permission.[16] Copyright 2018, Elsevier. b) Crystal structures of β-Al_2O_3 and β''-Al_2O_3. Reproduced with permission.[29] Copyright 2018, Cell Press. c) Crystal structures of the representative NASICON ($Na_3Zr_2Si_2PO_{12}$) with rhombohedral and monoclinic phase. Reproduced with permission.[29] Copyright 2018, Cell Press. d) Four different types of bottlenecks in Na^+ conducting pathways in the monoclinic NASICON structure. Reproduced with permission.[61] Copyright 2016, American Chemical Society.

the conductive planes of β''-Al_2O_3, this compound exhibits superior ionic conductivity. Specifically, single-crystal β''-Al_2O_3 can achieve ionic conductivities of up to 1 S cm^{-1} at 300 °C, typically 2 to 5 times higher than that of polycrystalline structures.[54,56,57] This enhanced conductivity is primarily attributed to the avoidable high grain boundary resistance present in polycrystalline materials.[58]

It is noteworthy that β''-Al_2O_3 is thermodynamically unstable and tends to partially decompose into thermodynamically stable β-Al_2O_3 and $NaAlO_2$ impurities.[8] Consequently, despite significant efforts to synthesize pure-phase β''-Al_2O_3, the resulting products typically consist of a mixture of β''-Al_2O_3, β-Al_2O_3, and other impurities. However, optimizing the ratio of β''-Al_2O_3 to β-Al_2O_3 and adjusting the microstructure, the ionic conductivity can be effectively enhanced.[56,59,60]

2.2.2. NASICON

NZSP, commonly known as NASICON, has attracted extensive research since it was reported as a Na^+ conductor by Goodenough et al. in 1976.[30,62] Compared to the 2D Na^+ transport pathways in β/β''-Al_2O_3 structures, the NASICON features a 3D open framework formed by corner-sharing SiO_4/PO_4 tetrahedra and ZrO_6 octahedra, which facilitates the high reversibility and rapidity of Na^+ insertion and extraction.[54,63] From the perspective of crystal structure and composition, NZSP is regarded as a binary solid solution of $NaZr_2P_3O_{12}$ and $Na_4Zr_2Si_3O_{12}$.[64] Variations in Si content allow NZSP to exhibit different crystalline phases, specifically rhombohedral (R-3c) and monoclinic (C2/c) phases (Figure 5c).[29] When x = 2, $Na_3Zr_2Si_2PO_{12}$ demonstrates the highest ionic conductivity, achieving $\approx 10^{-1}$ S cm^{-1} at 300 °C and $\approx 10^{-4}$ S cm^{-1} at RT.[30,62] Consequently, modifications to NASICON materials have primarily focused on $Na_3Zr_2Si_2PO_{12}$.

In NASICON-type SEs, Na^+ migration is dominated by Na^+ mobility and concentration, which are largely influenced by the size of bottlenecks and the Na content within the unit cell.[65] For instance, in the monoclinic phase of NASICON, four distinct bottleneck regions exist, comprising two Na_1-Na_2 and two Na_1-Na_3 channels (Figure 5d).[61] The size of these bottlenecks is directly related to the migration barrier, thereby affecting ionic conductivity. Moreover, promoting Na^+ migration at grain boundaries is crucial for enhancing the conductivity of NASICON. The main obstacles arise from insulating impurities and defects such as pores and microcracks at the grain boundaries, which severely impede Na^+ transport by disrupting the transport network. Generally, optimizing the ionic conductivity of NASICON can be achieved by adjusting the concentration of mobile Na^+, modifying bottleneck sizes, reducing impurity content, and minimizing grain boundary defects.

2.3. Sulfide SEs

Sulfide SEs are considered very promising for sodium batteries due to their high Na^+ conductivity, mild synthesis conditions, low grain boundary resistance, and excellent plasticity. In contrast

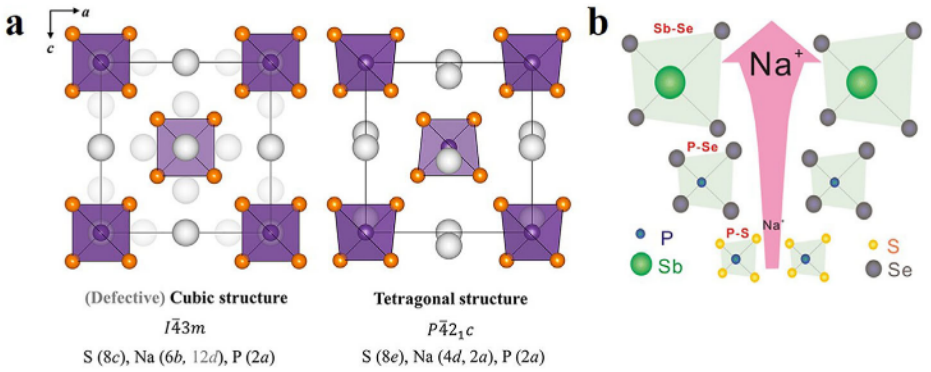

Figure 6. a) Crystal system of c- and t-NPS along the b-axis perspective. Reproduced with permission.[66] Copyright 2018, American Chemical Society. b) Schematic diagram of Na^+ diffusion in different compounds. Reproduced with permission.[67] Copyright 2017, Springer Nature.

to oxide SEs, the high Na^+ conductivity of sulfide SEs primarily arises from the lower electronegativity and larger ionic radius of S^{2-} ions, which weaken the electrostatic interactions between the sulfide framework and Na^+ cations, thereby widening the Na^+ migration pathways. The most common sulfide SE is NPS. As illustrated in **Figure 6a**, NPS exhibits two crystal structures: cubic and tetragonal, with the tetragonal phase transitioning to the cubic phase at temperatures equal to or greater than 530 K.[66] However, several issues remain to be addressed, including insufficient ionic conductivity at RT, susceptibility to reaction with H_2O in the air, producing toxic H_2S, and a relatively narrow electrochemical stability window. Experimental studies indicate that doping is an effective strategy for enhancing ionic conductivity. As shown in Figure 6b, doping at the P site with Sb can expand the unit cell and channels, thus improving ionic conductivity.[67]

2.4. Halide SEs

Compared to S^{2-}/O^{2-}, halide anions exhibit weaker interactions with Na^+ and possess larger ionic radii, which facilitates the formation of expansive 3D frameworks conducive to ion transport.[68] Consequently, halide SEs not only inherit the high electrochemical oxidative stability of oxides, but also offer advantages such as improved deformability and mechanical sintering.[69]

Halide SEs can be generally represented as Na_3MX_6 (M = Y, Zr, Al, Sc, Er; X = F, Cl, Br, I), where both M and X can consist of one or multiple elements. Variations in the radii of M and X give rise to different crystal structures, including trigonal P-31c, monoclinic $P2_1/n$, and monoclinic C2/m phases.[70] As illustrated in **Figure 7**, the crystal structure of halide SEs is primarily composed of stable NaX_6 and MX_6 octahedra, and the manner in which NaX_6 units are connected influences Na^+ migration pathways and transport properties.[71]

Due to their wide electrochemical stability window and compatibility with high-voltage CAMs, halides are considered promising SEs.[48,72] First-principles calculations have revealed that the oxidative stability limits of Na_3YCl_6 (NYC) and Na_3YBr_6 (NYB) are 3.75 and 3.36 V, respectively, which are significantly higher than those of previously reported sulfide SEs, such as NPS (2.25 V) and Na_3AsS_4 (2.1 V).[7,71] Subsequently, Yu et al.

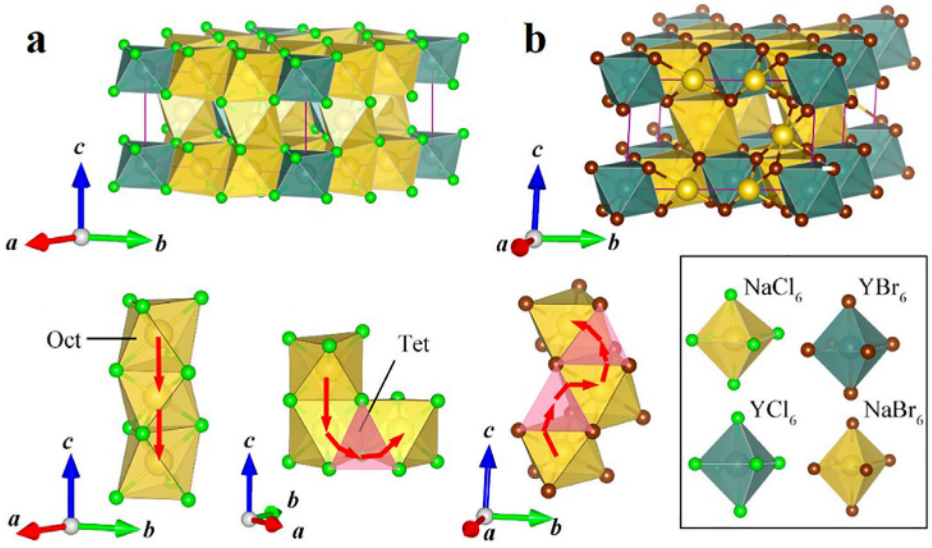

Figure 7. The crystal structure of a) Na_3YCl_6 and b) Na_3YBr_6. Reproduced with permission.[71] Copyright 2020, American Chemical Society.

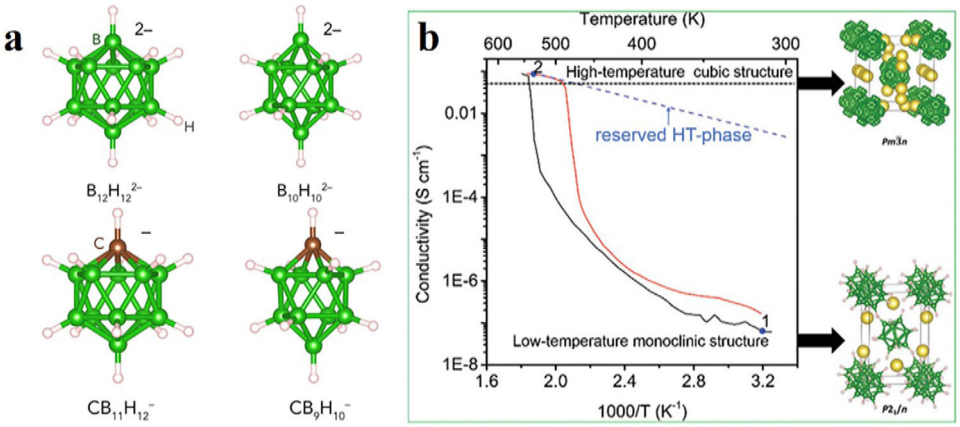

Figure 8. a) Polyanions constituting complex hydride SEs. Reproduced with permission.[29] Copyright 2018, Cell Press. b) Temperature dependence of the Na^+ conductivity of $Na_2B_{12}H_{12}$ in the 308–554 K. Reproduced with permission.[86] Copyright 2020, Wiley-VCH.

employed grand potential diagrams to evaluate the electrochemical stability windows of Na_3MX_6 (X = Cl, Br, or I) as a function of Na chemical potential, the oxidative stability generally follows the trend: $Na_3MCl_6 > Na_3MBr_6 > Na_3MI_6$.[73]

Various strategies have been reported to enhance the ionic conductivity of halide SEs. For example, aliovalent substitution has been employed to optimize crystal structure parameters and introduce additional vacancies, thereby facilitating Na^+ migration and improving ionic conductivity. Zr^{4+} is among the most commonly used dopants, as demonstrated in $Na_{3-x}Er_{1-x}Zr_xCl_6$ and $Na_{3-x}Y_{1-x}Zr_xCl_6$.[74] Additionally, anionic mixing has been explored to further enhance conductivity.[75] For instance, Inoishi et al. introduced polyanionic SO_4^{2-} into Na_2ZrCl_6 to weaken the bonding between Na^+ and Cl^-, leading to the synthesis of a superionic conductor, $Na_{0.67}Zr(SO_4)_{0.33}Cl_4$, with an ionic conductivity of 1.6 mS cm^{-1}.[76] From a structural perspective, Na^+ in amorphous SEs are randomly distributed rather than confined within fixed channels or planes, resulting in higher ionic conductivity and softer mechanical properties compared to their crystalline counterparts.[77,78] Lin et al. reported amorphous Na^+ conductors based on a mixed halide-oxide framework (Na_2O_2-MCl_y, M = Hf, Zr, and Ta).[36] Through dual-anion chemistry and the synergistic effects of bridging and non-bridging oxygen species, rapid Na^+ transport was achieved, yielding an ionic conductivity as high as 2 mS cm^{-1} at RT (25°C).

2.5. Hydride SEs

Hydrides represent a class of SEs that remain largely unexplored; however, they exhibit highly attractive material properties, including compatibility with Na metal anodes, low density, soft mechanical characteristics, and excellent thermal and chemical stability.[79–81] With the discovery that complex hydrides containing larger anions can achieve significantly enhanced ionic conductivity, their application as SEs in ASSSBs, has garnered increasing attention.

In 2012, Orimo et al. first reported on the use of complex hydrides, specifically $NaAlH_4$ and Na_3AlH_6, as SEs for SIBs.[32] Their conductivities were measured at only 2.1×10^{-10} and 6.4×10^{-7} S cm^{-1} at RT, respectively. This work paved the way for further research into composite hydrides as SEs for SIBs.

Composite hydride SEs are composed of Na^+ and polyanions, with the size of the polyanion significantly influencing the performance of the SE. Compared to smaller anions such as AlH_4^-, AlH_6^-, BH_4^-, and NH_2^-, composite hydrides formed from Na^+ and larger quasi-spherical anions (such as $B_{10}H_{10}^{2-}$, $B_{12}H_{12}^{2-}$, $CB_9H_{10}^-$, and $CB_{11}H_{12}^-$) demonstrate higher ionic conductivities due to their disordered phase structure (**Figure 8a**).[29,82,83] This is partly attributed to the larger anion size, which results in open frameworks presenting less obstruction to migration pathways. Additionally, the highly disordered sublattice and unoccupied Na^+ sites in the high-temperature phase reduce the energy barrier for Na^+ migration and enhance the Na^+ mobility.[84,85] As illustrated in Figure 8b, the conductivity of $Na_2B_{12}H_{12}$ increases sharply by nearly three orders of magnitude when transitioning from a tetrahedral to a cubic phase, reaching over 0.1 S cm^{-1} between 540 and 573 K.[33,86] Based on these principles, lowering the phase transition temperature to maintain a disordered structure at RT can achieve high Na^+ conductivity. Furthermore, increasing the anion/cation size ratio presents another strategy for enhancing conductivity, which can be accomplished through anionic chemical modifications, anionic mixing, and microcrystallization nanostructuring or disordering methods.[87–92]

2.6. Summary

SEs for ASSSBs primarily include oxides, sulfides, halides, and hydrides, each exhibiting distinct characteristics and limitations. A comparative evaluation of their physicochemical properties is presented in **Figure 9**.

Oxide SEs demonstrate high thermodynamic stability and a wide electrochemical stability window, effectively preventing oxidative decomposition at high-voltage CAMs. However, their high Young's modulus results in significant mechanical rigidity, which can easily induce interfacial cracking during cycling and lead to poor physical contact with electrode materials. Consequently, high-temperature sintering or interfacial modifications

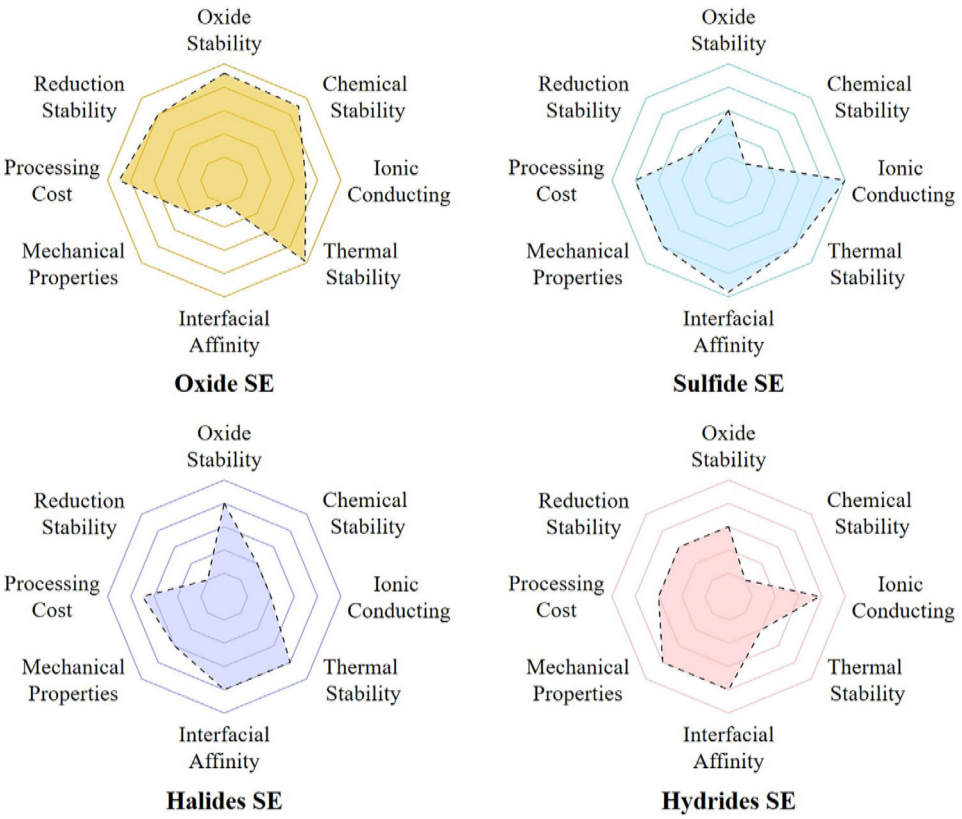

Figure 9. Comparison of the differences in physical properties among various SEs.

are typically required to address these issues. Sulfide SEs offer a low Young's modulus and good interfacial compliance, coupled with exceptionally high ionic conductivity that supports rapid charge–discharge operations. Nevertheless, their sensitivity to air, including tendencies to react with moisture to form by-products, increases manufacturing costs. Furthermore, under charging processes, their limited chemical stability may lead to the formation of an unstable CEI.[93] Halide SEs possess relatively low ionic conductivity but demonstrate high oxidative stability and good mechanical deformability.[69,94] However, most halide SEs are highly hygroscopic, with some undergoing irreversible chemical degradation upon exposure to ambient atmosphere.[95] Hydride SEs possess the advantages of potentially high ionic conductivity and lightweight characteristics. However, they are extremely sensitive to air and moisture, and some hydrides require a structural transition from an ordered to a disordered phase at elevated temperatures to achieve high ionic conductivity.[96,84] In addition, their complex synthesis processes, the high toxicity of precursors, and the still unclear ion migration mechanisms severely limit their practical application in ASSSBs.[97]

Considering key performance metrics such as ionic conductivity, chemical and electrochemical stability, and interfacial compatibility, NASICON-type oxides (e.g., NZSP) and sulfides (e.g., NPS) currently appear to be the most promising candidates for commercial application. To address the high rigidity and poor interfacial contact of oxide SEs, strategies such as introducing flexible interfacial buffer layers, employing gradient interfaces, or designing micro/nanostructures can be used to relieve stress and improve interfacial adhesion. For sulfide SEs, issues related to chemical stability and interfacial side reactions can be mitigated by constructing stable interfacial protective layers, optimizing electrode architectures, and using low–working-potential CAMs to suppress undesirable reactions and enhance long-term cycling stability. Future research can further advance SE performance along two complementary directions: at the structural design level, optimizing transport kinetics by constructing multidimensional ion channels, increasing charge carrier concentration, modulating lattice spacing, and weakening ion-lattice interactions; at the materials engineering level, employing strategies such as doping, solid solution formation, and nanostructuring to simultaneously enhance ion migration efficiency and chemical stability. The evaluation framework established in this study provides a systematic reference for balancing performance metrics and guiding the selection of SEs for practical applications.

3. Cathode Active Materials (CAMs)

The CAM serves as the host for Na^+ storage and transport, with its theoretical capacity and operating voltage being the key determinants of the battery's energy density. The specific capacity of an CAM is governed by its molecular weight and number of available electrons in the valence band; low molecular weight and high number of "valence" electrons contribute to high specific capacity. Moreover, a high specific capacity coupled with a high operating voltage further enhances the specific energy. The cycling stability of CAMs depends on their structural stability, which is

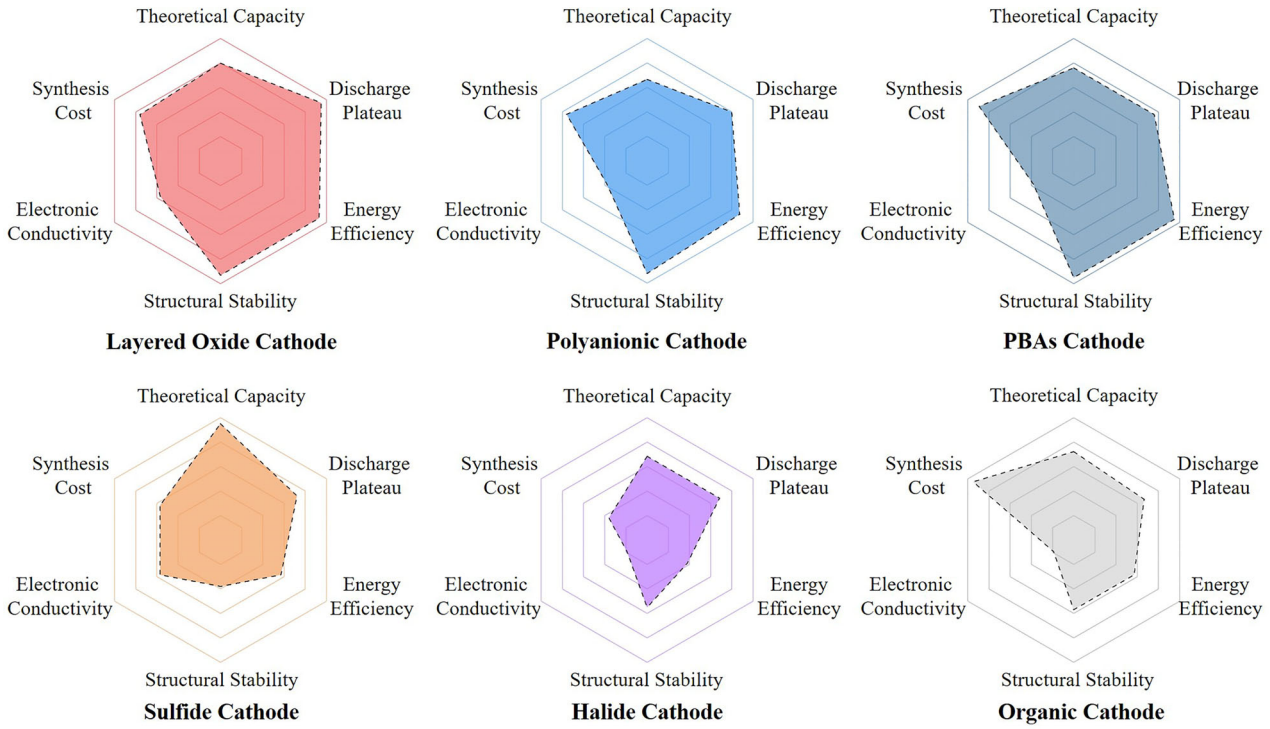

Figure 10. Comparison of the electrochemical performance parameters and physical properties of various types of CAMs.

typically influenced by factors such as crystal structure, charge–discharge depth, and fabrication processes. Additionally, the rate capability of the CAM is affected by kinetic factors, including ion diffusion rates and electronic conductivity. Accordingly, we compared the key electrochemical performance parameters and manufacturing costs of common CAMs (as shown in **Figure 10**).

To date, the development of CAMs has been primarily focused on liquid-electrolyte, SIBs. Research efforts have been concentrated on issues such as the formation of the CEI, volume changes of the CAM, migration and dissolution of transition metals, and phase transformations. However, the transition from liquid electrolyte to ASSSBs imposes different requirements on the properties of CAMs due to the distinct characteristics of solid and liquid electrolytes, including differences in electrochemical stability and mechanical strength.

In the following sections, we will provide a comprehensive overview of the properties of various types of CAMs and the current research trends in their application for ASSSBs, **Table 1** summarizes the electrochemical performance of various CAMs in ASSSBs. Specifically, we will discuss layered transition metal oxides, sulfides, halides, and organic CAMs, highlighting their Na storage mechanisms. Additionally, we will explore the design strategies for each type of CAMs, their advantages and limitations in ASSSBs, and propose potential solutions to address these challenges.

3.1. Insertion-Type CAMs

Insertion-type CAMs represent the mainstream choice for SIBs, primarily including layered or tunnel-structured oxides (e.g., $Na_{0.44}MnO_2$, $NaMnO_2$, and $Na_2Ti_3O_7$[118–120]), polyanionic compounds (e.g., $Na_3V_2(PO_4)_3$ (NVP)[169,170]), and PBAs (e.g., $Na_2Fe[Fe(CN)_6]$[121]). These CAMs offer advantages such as long cycle life, superior rate performance, high structural stability, and a well-established research foundation. However, each class also exhibits certain limitations. For instance, layered oxides often suffer from phase transitions during cycling and are highly sensitive to moisture; some polyanionic compounds involve relatively high-cost elements; and PBAs may suffer from structural defects and lower working voltages. Despite these drawbacks, insertion-type CAMs have been widely adopted in SIBs due to their stability and reversibility. Future research efforts will focus on enhancing energy density, reducing costs, and optimizing environmental adaptability.

3.1.1. Oxide CAMs

Transition metal oxides (Na_xMO_2, $x \leq 1$, M = Mn, Ni, Fe, Co, Ti, V, Cr, etc.) have attracted significant attention as CAMs for SIBs due to their high energy density and ease of synthesis. Based on their structural characteristics, Na_xMO_2 can be categorized into layered transition metal oxides and tunnel-type oxides. The layered structure consists of alternating sodium and transition metal layers, where the transition metal forms MO_6 octahedra composing the transition metal layers, while Na^+ occupy interlayer positions. Depending on the coordination environment of Na^+ (octahedral or prismatic) and the number of transition metal layers per unit cell, layered oxides can be further classified into P2, P3, O2, and O3 structures.[122] In contrast, tunnel-structured Na_xMO_2 adopts an orthorhombic framework composed of MO_6 octahedra and

Table 1. Summary of the electrochemical performance of different types of cathodes in ASSSBs.

Sodium storage mechanisms	Categories	Formula	Voltage range	Initial efficiency [%]	Performance	Ref.
Insertion-type	Oxide	$Na_{0.85}Mn_{0.5}Ni_{0.4}Fe_{0.1}O_2$	2.0–4.0 V (vs. $Na^+/Na_{15}Sn_4$)	99.9% (0.1C)	86.58 mAh g^{-1} 0.2C, 700 cycles	[36]
		$Na_{0.66}Ni_{0.33}Mn_{0.67}O_2$	2.5-3.8 V (vs. Na^+/Na)	/	52.2 mAh g^{-1} 6C, 10000 cycles	[98]
		$NaCrO_2$	2.0-3.25 V (vs. Na^+/Na)	88.89% (0.05C)	68 mAh g^{-1} 0.2C, 250 cycles	[99]
		$Na_{0.67}Ni_{0.23}Mg_{0.1}Mn_{0.67}O_2$	2.0-4.5 V (vs. Na^+/Na)	/	47 mAh g^{-1} 48 mA g^{-1}, 1000 cycles	[100]
		Na_xCoO_2	2.0-4.2 V (vs. Na^+/Na)	/	112 mAh g^{-1} 0.15C, 100 cycles	[101]
	Polyanionic compounds	$Na_3V_2(PO_4)_3$	2.5-3.7 V (vs. Na^+/Na)	97.5% (0.2C)	≈90 mAh g^{-1} 10C, 10000 cycles	[102]
		$Na_3Ti_2(PO_4)_3$	1.5-2.5 V (vs. Na^+/Na)	90.99% (0.1C)	≈100 mAh g^{-1} 0.1C, 50 cycles	[103]
		$Na_3V_2O_2(PO_4)_2F$@rGO	2.5-4.5 V (vs. Na^+/Na)	/	88.1% (capacity retention) 4C, 1000 cycles	[104]
		$Na_{2+2\delta}Fe_{2-\delta}(SO_4)_3$	1.5-4.0 V (vs. $Na_2Ti_3O_7$)	/	87.2 mAh g^{-1} (80°C) 2C, 100 cycles	[105]
		$NaFePO_4$/C	1.5-4.0 V (vs. Na^+/Na)	98% (0.2C)	131 mAh g^{-1} 0.2C, 1 cycle	[106]
		$Na_3(VOPO_4)_2F$	2.5-4.15 V (vs. Na^+/Na)	91.4% (0.1C)	78 mAh g^{-1} 0.2C, 800 cycles	[107]
	Prussian blue analogues	HQ-NaFe	2.0-4.2 V (vs. Na^+/Na)	/	84.6% (capacity retention) 1C, 1100 cycles	[108]
		$Na_2MnFe(CN)_6$	2.5-4.0 V (vs. Na^+/Na)	96% (0.1C)	89.2% (capacity retention) 0.5C, 200 cycles	[109]
		$Fe_4[Fe(CN)_6]_3$	1.25-4.25 V (vs. Na^+/Na)	/	84.6% (capacity retention) 0.05 mA cm^{-2}, 20 cycles	[110]
Conversion-type	Sulfide/halide	NPS-nano-Na_2S-C	0.5–3.0 V (vs. Na^+/Na-Sn-C)	/	438.4 mAh g^{-1} 50 mA g^{-1}, 50 cycles	[111]
		$NiCl_2$ (Ni@RGO)	2.0 -2.8 V (vs. Na^+/Na)	/	132.7 mAh g^{-1} 0.6C, 500 cycles	[112]
		FeF_3	1.2-4.0 V (vs. Na^+/Na)	65.2% (0.1C, 60°C)	150 mAh g^{-1} 0.1C, 100 cycles	[113]
		FeF_3	1.2-4.0 V (vs. Na^+/Na)	/	> 175 mAh g^{-1} 96 mA g^{-1}, 100 cycles	[114]
		FeF_3	1.2-4.0 V (vs. Na^+/Na)	/	145 mAh g^{-1} 110 mA g^{-1}, 90 cycles	[115]
Other	Organic	$Na_4C_6O_6$	1.5–2.6 V (vs. $Na^+/Na_{15}Sn_4$)	99% (0.1C, 60°C)	107 mAh g^{-1} 0.2C, 400 cycles	[47]
		PTO	1.1-3.1 V (vs. Na^+/Na)	82% (0.1C, 60°C)	294.88 mAh g^{-1} 0.1C, 100 cycles	[116]
		PBQS	1.0 -3.8 V (vs. Na^+/Na)	/	182.24 mAh g^{-1} 50 mA g^{-1}, 100 cycles	[117]

MO_5 square pyramids, with Na^+ residing in S-shaped and pentagonal tunnels formed by MO_5 pyramids and MO_6 octahedra.

The electrochemical and physicochemical properties of different Na_xMO_2 structures vary significantly due to their structural differences. O3-type Na_xMO_2, for instance, offers a higher theoretical capacity due to its abundant Na^+ insertion sites. However, charge-discharge cycling induces multiple phase transitions, such as O3-P3, which introduce energy barriers affecting bulk ionic diffusion. Additionally, significant structural changes during multiphase transitions can lead to structural collapse, ultimately resulting in severe capacity degradation and reduced cycle life. In contrast, P2-type materials exhibit enhanced cycling stability due to their resistance to phase transitions. The transformation between P2 and other phases requires MO_6 octahedral rotation and M—O bond breaking, which is kinetically hindered. Consequently, P2-phase materials undergo minimal structural change during Na^+ insertion/extraction, contributing to their superior cycle stability.[123] Furthermore, the larger interlayer

spacing of P2-phase materials facilitates Na^+ diffusion, as Na ion migrates between adjacent prismatic sites, leading to excellent rate capability.[124,125] However, their lower Na content results in reduced specific capacity, necessitating additional pre-sodiation treatments. Furthermore, sodium layered transition metal oxides are prone to react with H_2O and CO_2 in ambient conditions, leading to material expansion, cracking, and deterioration of electrochemical performance.[126] As a result, an inert atmosphere is required during handling and processing, increasing manufacturing and transportation costs. Unlike most layered transition metal oxides, tunnel-type transition metal oxides exhibit superior structural stability both in air and during Na (de)intercalation. However, their inherently low initial sodium content limits their theoretical capacity, posing a significant challenge for practical applications.

The application of oxide CAMs in ASSSBs faces several challenges: 1) The oxidation potential of oxides significantly exceeds the oxidative decomposition potential of sulfide SEs, leading to the formation of an irreversible resistive interfacial layer, particularly in the presence of conductive carbon. 2) A high-resistance space-charge layer is typically formed at the interface between the oxide CAM and an electrolyte with lower chemical potential, impairing ion transport. 3) The high Young's modulus of oxide CAMs generates substantial interfacial stress during cycling, which can disrupt mechanical contact between the CAM and SE particles, causing ion transport pathways to fail. These interfacial issues can be mitigated by applying protective coatings on CAMs or introducing a buffer layer between the CAM and SE. However, these solutions increase processing costs, and additional interfaces may negatively impact ionic diffusion kinetics.

3.1.2. Polyanionic Compounds

Polyanionic materials have been extensively studied as cathodes for SIBs due to their high structural stability, thermal safety, and elevated operating voltage, which arise from the strong inductive effects of highly electronegative anionic groups.

Currently available polyanionic compounds primarily include phosphates (e.g., $NaFePO_4$ and NVP), pyrophosphates (e.g., $Na_2MP_2O_7$ and $Na_4M_3(PO_4)_2P_2O_7$), fluorophosphates (e.g., Na_2MPO_4F and $Na_3(VO_x)_2(PO_4)_2F_{3-2x}$, where M = Fe, Co, Mn), and sulfates (e.g., $Na_2Fe_2(SO_4)_3$ and $Na_2Fe(SO_4)_2{\cdot}2H_2O$).[127] However, due to the separation of metal polyhedra and the strong electronegativity of anions, these CAMs generally exhibit poor electronic conductivity, which limits electron transport rates and increases electrochemical polarization. Consequently, polyanionic compounds typically suffer from inferior rate performance.

To address these limitations, various strategies have been employed to enhance reaction kinetics and improve rate capability. These approaches include carbon incorporation, nanoparticle downsizing, and the design of porous micro-/nanostructures.[128] The nanoscale reduction of particle size significantly shortens the Na^+ diffusion pathways within the bulk material, while porous architectures increase the specific surface area and expand the electrode-electrolyte contact interface, thereby facilitating more efficient ion and electron transport.

3.1.3. PBAs

PBAs, with the general chemical formula $A_xM1[M2(CN)_6]{\cdot}zH_2O$ (where A represents an alkali metal, and M1 and M2 are transition metals), have attracted significant attention as CAMs for SIBs due to their open-framework structure, higher theoretical capacity, and low cost.[129,130] For instance, $Na_2Fe[Fe(CN)_6]$ can deliver a specific capacity of ≈160 mAh g^{-1} with an average operating voltage of 3.10 V,[131] while $Na_2Mn[Mn(CN)_6]$ exhibits a highly reversible capacity of 209 mAh g^{-1}.[132]

However, the inherent poor electronic conductivity and structural disorder of PBAs typically require strategies such as cation doping, transition metal substitution, and compositing with conductive carbon materials (e.g., coating or supporting) to improve their electrochemical performance.[133–136] For example, Goodenough et al. nucleated PBA nanoparticles on carbon nanotubes (CNTs), where the CNT network provided superior electrical connectivity between the anchored PBA nanoparticles and the current collector, achieving a specific capacity of 142 mAh g^{-1} and an energy density of 408 Wh kg^{-1}.[135] While this strategy improves conductivity, it also reduces the proportion of CAM, thereby compromising overall energy density. In recent years, a novel approach involving the introduction of a high-entropy strategy into crystal structures has been proposed to significantly enhance the electrochemical properties of PBAs.[137–139] Ma et al. developed a high-entropy $Na_x(FeMnNiCuCo)[Fe(CN)_6]$ (HE-PBA) via a straightforward co-precipitation method, where the incorporation of five equimolar transition metal cations into nitrogen-coordinated lattice sites achieved a marked increase in the system's configurational entropy.[134] This structural design demonstrated near-zero strain characteristics during Na (de)intercalation, leading to significantly improved cycling stability and rate capability.

More critically, the intrinsic water content of most PBAs, typically ≈15 wt.%, is difficult to fully eliminate. This residual water can trigger severe side reactions in ASSSBs, leading to poor cycling stability, particularly when paired with moisture-sensitive SEs such as sulfides.[140,141]

3.2. Conversion-Type CAMs

Conversion-type CAMs represent a crucial class of cathodes for SIBs, with their Na storage mechanism based on reversible conversion reactions. These reactions involve phase transformations between sodium and various compounds—such as metal oxides, sulfides, and halides—during charge and discharge. Compared to conventional insertion-type CAMs, conversion-type CAMs generally offer higher theoretical specific capacities. However, they face significant challenges related to cycling stability, electrochemical reversibility, and sluggish reaction kinetics.

3.2.1. Sulfide CAMs

MS_x has garnered significant attention in SIBs due to their high theoretical capacities and environmental compatibility. Their Na storage mechanisms typically involve multi-electron processes, including intercalation, conversion, and in some cases, alloying reactions.[142] For materials such as MoS_x, WS_x, FeS_x, CoS_x,

and NiS_x, sodiation generally proceeds via a combination of intercalation and conversion, with Na_2S and metallic M as the primary products. In contrast, sulfides such as Sb_2S_3 undergo intercalation-conversion-alloying reactions, yielding final products such as Na_2S and Na_xM.[143] NbS_2, on the other hand, stores Na through a pure intercalation mechanism, with the M–S framework remaining intact throughout cycling. This structural retention enables excellent electrochemical stability and cycling performance.[144,145]

MS_x with multi-step reaction mechanisms generally possesses higher theoretical specific capacities. For example, Sb_2S_3 has a theoretical capacity of 946 mAh g^{-1}. However, this advantage is inevitably accompanied by significant volume changes (>400%) during cycling, leading to structural collapse and rapid capacity fading.[146–148] Additionally, MS_x face challenges such as low electrical conductivity and limited ionic diffusion coefficients. To address these issues, carbon modification and nanostructuring strategies are commonly employed.[149] Carbon materials are considered ideal additives for buffering the significant volumetric changes during cycling. Furthermore, their excellent electrical conductivity can effectively compensate for the poor conductivity of MS_x. Meanwhile, materials with nanoscale structures can reduce electron transport distances, shorten ionic diffusion pathways, and mitigate the mechanical stresses induced by large volume fluctuations during repeated sodiation/desodiation.

It is worth noting that when MS_x is utilized in sulfide SE battery systems, it can effectively mitigate the (electro)chemical incompatibility between electrodes and electrolytes. This, to some extent, alleviates the degradation of electrochemical performance caused by interfacial issues.

3.2.2. Halide CAMs

In addition to metal oxides and sulfides, metal halides (MHs) have emerged as promising electrode materials in battery chemistry due to their high abundance and versatile properties. The electronegativity of halide ions is comparable to that of chalcogenide ions, enabling stable coordination with a wide range of cations and making MHs suitable for application in rechargeable batteries. High-performance electrodes based on MHs can be achieved through appropriate material synthesis and engineering strategies.

As early as 1997, Shigeto Okada and colleagues reported the use of MF_3 (M = Fe, V, Ti, Mn, and Co) as CAMs for LIBs, with FeF_3 demonstrating a reversible capacity of 80 mAh g^{-1}, corresponding to 34% of its theoretical capacity for the Fe^{3+}/Fe^{2+} redox couple.[150] Subsequently, the electrochemical performance of these cathodes was investigated in SIBs. Experimental results revealed that FeF_3 with a carbon coating delivered a discharge capacity of 145 mAh g^{-1}, achieving 61% of its theoretical value.[151] These findings confirmed the feasibility of using MHs as CAMs in SIBs. Furthermore, a variety of metal fluorides, such as CuF_2, Li_3VF_6, Li_2MnF_5, Li_3CrF_6, and $Li_{2-2x}Fe_{1+x}Cl_4$ have been extensively reported as CAMs for LIBs.[152–155] This success has spurred interest in exploring their analogs for SIBs systems. Beyond metal fluorides, metal chlorides and bromides, including $NiCl_2$, $NiBr_2$, $FeCl_2$, $ZnCl_2$, and $CuCl_2$, have also garnered significant attention in SIBs research.[112,156–159] For instance, Kim et al. demonstrated a novel Na-$CuCl_2$ rechargeable battery utilizing a $CuCl_2$/C cathode and an inorganic $NaAlCl_4{\cdot}2SO_2$ liquid electrolyte, achieving an energy density of 580 Wh kg^{-1}. The battery exhibited a capacity retention of ≈75% after 1,300 cycles at 1C.[156] Furthermore, they demonstrated that this battery chemistry could be extended to other copper halides, including CuF_2 and $CuBr_2$. With continuous advancements in battery technologies, metal halide materials are anticipated to find applications in ASSSBs.

However, MH materials face several challenges, including poor structural stability, low electronic conductivity, and restricted ion migration, which significantly limit their performance and development. Current studies suggest that lattice modulation, morphology engineering, and composite electrode design are effective strategies for addressing these issues.

3.3. Organic CAMs

Organic CAMs have garnered increasing attention due to their intrinsic advantages, including stable redox properties, multi-electron reaction mechanisms, and abundant natural reserves.[160] In the context of ASSSB systems, the low Young's modulus of organic CAMs enables intimate interfacial contact with SEs, thereby improving cycling stability and mitigating issues associated with the dissolution and shuttle effects of small organic molecules in liquid-phase systems.[161,162] For instance, Fang et al. demonstrated that the low-elastic-modulus PTO organic cathode (4.2 ± 0.2 GPa) maintained close interfacial contact with NPS throughout cycling, overcoming mechanical stress and achieving up to 500 cycles of stable performance.[116]

Compared to inorganic CAMs, organic materials offer several additional benefits. First, they are typically synthesized using mild methods, such as polymerizations at room or moderate temperatures, which reduce energy consumption and CO_2 emissions. Second, organic compounds can be directly extracted from biomass or synthesized without generating excess CO_2, offering environmental friendliness and cost-effectiveness.[163,164] Many organic compounds store Na^+ through redox mechanisms, exhibiting faster reaction kinetics than inorganic intercalation CAMs, making them potential candidates for high-power electrodes. Moreover, organic materials feature high specific capacities due to their multi-electron reactions, moderate operating potentials owing to redox-active functional groups, and high specific energy and intrinsic safety. For example, Song et al. reported that poly(benzoquinonyl sulfide) (PBQS) achieved a high energy density of 557 Wh kg^{-1} (2.08 V × 268 mAh per g of CAM) in rechargeable sodium batteries, surpassing most intercalation-type inorganic CAMs.[117] However, organic materials also face significant challenges. Their low density reduces the volumetric energy density of ASSSBs. More critically, nearly all organic materials are electrical insulators, severely limiting the utilization of CAMs and rate performance. A common approach to address this issue involves adding substantial amounts of conductive materials to enhance electron transport within the electrode and improve CAM utilization. Yet, the low mass density and large surface area of organic materials necessitate excessive conductive material, which significantly reduces the proportion of CAM in the cathode and adversely impacts energy density.[165]

While organic polymers often exhibit good conductivity, particularly conductive polymers, their theoretical and reversible capacities are generally much lower than those of small-molecule organic compounds. This limitation arises from the fact that redox reactions in polymers are typically governed by a p-doping and dedoping mechanism involving large electrolyte anions, which is characterized by low doping levels and slow kinetics and charge balancing electrolyte amounts, resulting in the overall poor capacity performance.[166]

3.4. Summary

In ASSSBs, the selection of CAMs critically determines energy density, cycling stability, and rate capability of the cells. Insertion-type CAMs—including conventional layered oxides, polyanionic compounds, and PBAs—typically feature stable crystal frameworks and enable reversible Na^+ insertion/extraction reactions. Currently, most studies employ $NaCrO_2$[167,168] or NVP[169,170] as CAMs due to their excellent cycling stability and good compatibility with various SEs. However, these materials exhibit relatively limited energy density, and their operating voltages are mostly below 4.0 V (vs Na^+/Na). Their ionic and electronic conductivities still require enhancement, which can be achieved through micro/nanostructure optimization and carbon coating or conductive composite encapsulation to shorten Na^+ diffusion pathways, improve interfacial contact, and establish efficient electronic transport networks.[171]

Layered oxides, with their high specific capacity, high tap density, the highest voltage of up to 4.5 V (in ASSSBs),[172] and facile synthesis, represent one of the most promising CAM categories for achieving both high energy density and high operating voltage. Nevertheless, oxygen-induced anionic redox reactions readily occur at high voltages (typically above 4.0 V),[173] involving electrochemical activity of O 2p lone-pair states or non-hybridized 2p orbitals.[174] These anionic redox processes inevitably lead to oxygen loss from the lattice, irreversible phase transitions, and structural distortion, ultimately resulting in structural collapse and capacity degradation.[175,176] Moreover, in ASSSBs employing non-oxide SEs, oxygen release accelerates electrolyte decomposition and side reactions, increasing interfacial impedance and causing severe voltage hysteresis.

PBAs feature an open 3D framework structure and low Na^+ migration barriers, enabling fast charging/discharging with minimal voltage hysteresis. However, they generally exhibit limited specific capacity, and residual water in their structure may compromise interfacial compatibility with SEs. It should be noted that PBAs are easily synthesized, environmentally friendly, and possess certain cost advantages.

Conversion-type CAMs (mainly sulfides and halides) achieve high theoretical capacity through chemical conversion reactions, significantly boosting battery energy density. Sulfide materials, benefiting from relatively weak M—S bonds, demonstrate favorable kinetics during Na^+ insertion/extraction. However, conversion reactions upon deep charging/discharging can induce volume expansion exceeding 100%, leading to particle pulverization and loss of interfacial contact. Halide CAMs, while offering high theoretical capacity, face challenges such as difficulty in densification due to intrinsic brittleness and high synthesis costs.

Organic CAMs, with advantages of light weight, tunable chemical structures, and low density, show potential for high specific energy and environmentally benign battery designs. However, they generally exhibit lower operating voltage than inorganic CAMs, along with insufficient Na^+ mobility and electronic conductivity, pronounced voltage hysteresis, and poor cycling stability. Although organic materials are typically low-cost and renewable, their performance is highly sensitive to processing conditions.

In ASSSBs, insertion-type materials are generally preferred as CAMs, with oxide insertion-type materials being particularly prominent due to their low cost, high operating voltage, and high energy density. Although interfacial issues may arise when these materials are in contact with SEs—such as severe interfacial delamination with oxide SEs or side reactions with sulfide SEs—these challenges can be partially mitigated through hot-pressing techniques or surface coating of the CAM. Additionally, sulfide CAMs also exhibit competitive advantages, not only offering high theoretical capacities but also forming more stable interfaces when paired with fast-ion-conducting sulfide SEs. Notably, in solid-state sodium–sulfur batteries employing S_8 as the CAM, a cathode-specific capacity exceeding 1600 mAh g^{-1} has been reported, demonstrating the considerable potential for high energy density.

4. Challenges in ASSSB Cathodes: Interfacial Compatibility and Ionic Transport

During the solidification process of batteries, researchers have primarily focused on modifying and designing SEs with high ionic conductivity, often neglecting the series of interface issues arising from the solid-solid contact between the SE and CAM when assembled into a battery. These interfacial issues typically include voids resulting from rigid contact or insufficient densification, as well as chemical and electrochemical reactions between the CAM and SE, which lead to high interfacial resistance and even structural degradation of the SE and/or the CAM.

4.1. General Challenges

4.1.1. Chemo-Mechanical Effects

The preparation of ASSSBs involves a pressure molding process, which includes mixing CAM with SE powders to form the composite cathode, followed by sequentially stacking the composite cathode, SE, and anode to construct the battery. Even though SEs with good ductility, such as sulfide SEs, are used, seamless interface contact cannot be achieved through cold pressing alone. This inevitably results in the formation of voids, leading to insufficient contact areas and limited ion transport pathways, which increase polarization during charge and discharge cycles. On the cathode side, this polarization significantly elevates the risk of oxidative decomposition of the SE. Additionally, volumetric or morphological changes driven by (electro)chemical processes during cycling have profound effects on performance and degradation.[177] On the cathode side, such changes are primarily associated with Na^+ deintercalation from the CAM, with the extent depending on the

depth of charge/discharge. However, interfacial side reactions between the CAM and the SE, as well as the decomposition of the SE itself, also contribute to volumetric changes. These changes can cause particle cracking and the formation of voids between SE and CAM particles, resulting in contact loss and increased tortuosity.[178] Such issues severely impede ion and electron diffusion kinetics, ultimately leading to poor electrochemical performance and rapid capacity fading. Therefore, in ASSSB systems, it is crucial to account for common (chemo-)mechanical effects, such as particle-to-particle stress and expansion/contraction of CAMs.

Traditional insertion-type CAMs exhibit minimal volumetric changes due to their unique crystal structures and reversible ion storage mechanisms. During ion insertion and extraction, the crystalline framework remains largely intact, undergoing only lattice distortion or phase transitions, resulting in negligible volume changes. In contrast, conversion-type materials experience significant volumetric changes due to bond breaking and the formation of new phases. Notably, these changes are not necessarily isotropic; the resulting strain may vary greatly along different crystallographic directions, inducing substantial anisotropic stress and mechanical damage.[179,180]

Given the impact of (chemo-)mechanical processes on battery performance, strategies to mitigate degradation mechanisms are essential. Two primary approaches can be adopted. First, the structural stability of CAMs can be enhanced through modification, such as doping and coating.[181,182] For instance, Zhang et al. designed O3-$Na_{0.9}Ni_{0.32}Zn_{0.08}Fe_{0.1}Mn_{0.3}Ti_{0.2}O_2$ (ZT-NFM) to regulate phase transitions for stable cycling. Zn doping triggered O/P coexisting phase transitions (P3-OP2), alleviating internal lattice strain during cycling. Meanwhile, the flexible TiO_6 octahedra buffered internal deformation of other TMO_6 octahedra, effectively suppressing microcracks in ZT-NFM and enhancing structural integrity for long-term cycling stability.[183] Second, the structural design of CAMs, such as nanostructuring, porosity engineering, or hollow structures, can buffer volumetric expansion.[184] However, these high-porosity materials increase the electrode's volume to some extent, which conflicts with the pursuit of high volumetric energy density. Therefore, the development of material combinations that minimize or even eliminate detrimental (chemo-)mechanical effects in solid-state composite cathodes is of paramount importance.

4.1.2. Electro-Chemical Effects

In addition to the dominant role of (chemo-)mechanical effects, the electro-chemical compatibility between CAMs and SEs represents another critical challenge. From a chemical perspective, the ideal scenario for battery operation is achieving thermodynamic stability at the interface between CAMs and SEs upon contact. However, a chemical potential difference typically exists between SEs and CAMs, leading to spontaneous reactions at the CAM-SE interface. These reactions result in the formation of a CEI on the cathode side. The reaction products can be categorized as ionic conductors or mixed conductors (i.e., conducting both ions and electrons). These latter pose a significant risk as their electronic conductivity enables continuous reactions with the electrolyte, ultimately depleting the electrolyte and causing structural collapse, leading to battery failure.[185] To mitigate cathodic side reactions, the application of stable oxide coatings on CAMs, the incorporation of specific buffer layers, and the design of optimized SE structures have been shown to improve interfacial stability.

Composite cathodes, comprising CAM, SEs, current collectors, binders, and conductive additives, inherently generate multiple interfaces. Among these, the interfaces between electronic and ionic conductors facilitate electrochemical reactions. Although SEs and electronic conductors are typically chemically inert, oxidative decomposition of the SE may still occur at the interfaces with conductive additives and current collectors when the operating voltage exceeds the intrinsic stability window of the electrolyte[177]. This process results in the formation of a complex CEI, which significantly increases charge transfer resistance.[186–188] Oh et al. demonstrated that when charged beyond 4.5 V, $Li_{10}GeP_2S_{12}$ (LGPS) undergoes continuous electrochemical decomposition at its interface with the carbon additive, acetylene black, leading to irreversible capacity loss.[189] Additionally, increasing the carbon content in the composite cathode exacerbates interfacial resistance and reduces the initial Coulombic efficiency during the first cycle. This effect is attributed to the accelerated decomposition kinetics of the SE on carbon surfaces.[187] Thus, the judicious use of high electronic conductivity materials in composite cathodes is critical for minimizing SE decomposition while maintaining high cathode performance. Koerver et al. further revealed that in batteries utilizing NCM811, increasing the voltage from 4.3 V to 4.8 V during prolonged cycling induces the continuous growth of the CEI and oxidation of the SE on the current collector, ultimately leading to capacity degradation.[186] These findings highlight how electrochemical side reactions constrain the operational voltage window of batteries, reducing both capacity and energy density. Such limitations contradict the fundamental objectives of developing high-performance ASSSBs.

4.1.3. Cathode Microstructure and Charge Transport

The electrochemical performance of ASSSBs is largely governed by the microstructure of the composite cathode, which directly dictates the transport behaviors of both ions and electrons. Typically, the composite cathode consists of CAM, SEs, and conductive additives. The spatial distribution, particle size, and interfacial contact among these components collectively regulate the kinetics of charge storage and release.[190,191]

Efficient Na^+ conduction relies on the formation of continuous and interconnected SE networks within the composite cathode. However, pores and discontinuous contacts severely hinder ion migration, increase transport tortuosity, and induce polarization. In high-loading cathodes, the increased CAM content and reduced SE fraction further interrupt ion-conduction pathways and limit the effective penetration depth, thereby reducing CAM utilization.[192,193] In the process of charge transport, the microstructure and particle size of the CAMs play a decisive role.[194] It has been reported that combining small SE particles with spherical CAM particles, while maintaining a large CAM/SE particle size ratio, is conducive to achieving high packing density.[190,191] Such a configuration can effectively reduce pore formation and increase the interfacial contact area, thereby

enhance the energy density. In addition, the influence of crystal structure should not be overlooked, particularly the differences in charge transport behavior between single-crystalline and polycrystalline CAMs. Single-crystalline particles possess continuous lattice structures that allow Na^+ to migrate without crossing grain boundaries, thereby avoiding dislocation-related barriers commonly found in polycrystalline materials and significantly enhancing the intrinsic electrochemical performance. However, if the particle size of single crystals is excessively large, the ion diffusion pathway becomes extended, thus limiting the kinetics of electrochemical reactions. In contrast, polycrystalline particles, despite containing numerous grain boundaries, can locally shorten the diffusion distance and improve ionic transport kinetics. In solid-state environments, the rigid mechanical support and interfacial confinement of SEs help suppress structural fracture in polycrystalline frameworks.[195] Nevertheless, particle agglomeration of both CAMs and SEs within composite cathodes of ASSSBs leads to heterogeneous charge distribution among polycrystalline CAM particles, which may further induce structural degradation.[196] Therefore, employing single-crystalline materials with precisely controlled particle sizes can achieve a balance between cycling stability and structural integrity, while maintaining favorable ionic diffusion kinetics in solid-state systems. Within SEs, grain boundaries represent intrinsic defects and are widely regarded as major barriers to Na^+ transport.[197] First-principles calculations and phase-field simulations strongly support this view, demonstrating that the energy barrier for Na^+ migration across NPS grain boundaries (0.580 eV) is approximately ten times higher than that for bulk diffusion (0.058 eV).[198] In addition, significant volume changes occur during Na^+ insertion and extraction in certain CAMs, especially in conversion-type CAMs, which tend to generate in situ voids and microcracks, thereby disrupting the ion-transport network. This issue becomes more severe in high-loading cathodes, where longer diffusion pathways and the formation of cracks or voids readily create transport bottlenecks. Therefore, strategies such as grain-boundary modification and porosity reduction are essential to effectively lower interfacial resistance and sustain efficient Na^+ transport.[102,199]

Electron transport, on the other hand, is primarily governed by the intrinsic electronic conductivity of the CAM and the distribution of conductive additives. Many polyanionic and layered oxide cathodes suffer from inherently low electronic conductivity, necessitating the introduction of carbon-based additives. However, excessive carbon can induce oxidative decomposition of sulfide SEs, accelerating capacity fading. In high-loading cathodes, electronic transport is further constrained, as the proportion of conductive agents is limited and electrons cannot efficiently reach the current collector through the thick electrode, resulting in severe potential gradients and polarization.[200,201] Constructing continuous and stable conductive networks while maintaining interfacial chemical stability is therefore critical to enhancing electronic transport.

The transport of Na^+ and electrons within the composite cathode is strongly coupled, and effective charge transfer can only be achieved when intimate contact is established at the CAM-SE-carbon triple-phase boundary. However, unavoidable chemo-mechanical effects during cycling—such as anisotropic lattice strain, particle cracking, and volumetric expansion/contraction—can disrupt the transport networks, leading to interfacial failure and increased charge-transfer resistance. These challenges are exacerbated in high-loading cathodes, where the transport channels deep within thick electrodes are more prone to stress accumulation and rupture, thereby limiting capacity utilization. Intercalation-type cathodes typically exhibit smaller structural distortions due to their robust host frameworks, whereas conversion-type cathodes often suffer from severe anisotropic stress, which rapidly deteriorates charge-transfer pathways.

To mitigate these challenges and improve charge transport in ASSSB composite cathodes, various microstructural engineering strategies have been proposed. For example, reducing particle size or constructing nanostructures can shorten Na^+ diffusion pathways, though this often comes at the expense of increased interfacial reactivity.[190] Surface coatings or buffer layers can stabilize the CAM-SE interface and preserve a continuous transport network.[40] Furthermore, rational optimization of the CAM/SE/conductive additive ratio has been demonstrated to balance energy and power densities while simultaneously reducing polarization and tortuosity.[202] Nevertheless, for high-loading cathodes, additional strategies such as developing hierarchical conductive networks, constructing vertically aligned ion/electron transport channels, and enhancing packing density through compaction are required to ensure efficient charge transport throughout the thick electrode. Building on this foundation, developing dual-functional SEs that possess both Na^+ conductivity and reversible redox activity has emerged as a highly promising strategy. By enabling the originally inactive SE components to contribute partial capacity, this approach can effectively alleviate the trade-off between ionic conductivity and energy density. Overall, the rational design and optimization of composite cathode microstructures are indispensable prerequisites for realizing ASSSBs with high energy density, superior rate performance, and long cycle life.

4.2. Critical Challenges of Oxide SE-Based ASSSBs

Oxide SEs exhibit high thermodynamic stability, a wide electrochemical stability window, and excellent environmental and thermal stability, rendering them ideal candidates for high-safety ASSSBs. However, their high mechanical strength and rough surface characteristics present significant challenges for achieving intimate interfacial contact.[29] As shown in **Figure 11**, we summarized the challenges faced by oxide SEs in ASSSBs.

In all-solid-state systems, the rigidity of the interface becomes particularly pronounced when oxide CAMs are paired with oxide SEs.[203] During the fabrication of composite cathodes, the oxide SE particles—typically brittle ceramics—cannot be fully densified through high-temperature sintering or pressure-assisted compaction, resulting in the formation of initial porosity. During subsequent cycling, CAMs undergo volumetric expansion and contraction, while the rigid oxide SE is unable to effectively buffer these dimensional changes. This leads to localized stress concentration, further promoting the formation of pores, microcracks, and interfacial delamination. The presence of porosity and grain boundaries directly reduces the contact area between CAMs and SEs, thereby increasing the tortuosity of ionic transport pathways

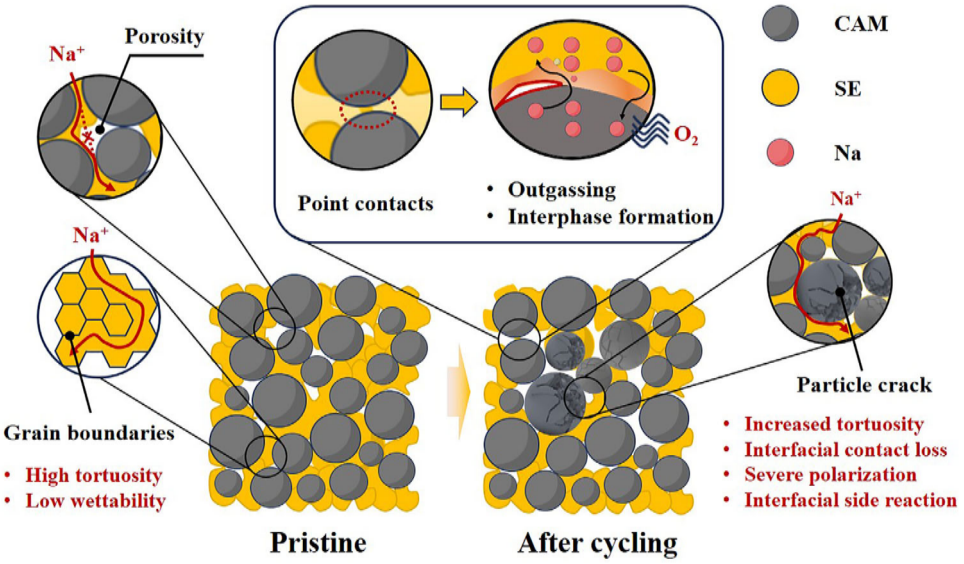

Figure 11. Schematic illustration of the critical challenges faced by oxide SE–based ASSSBs during electrode fabrication and after cycling.

and reducing the effective ionic conductivity within the cell.[204] Concurrently, the accumulation of pores contributes to an increase in interfacial impedance. Initially, insufficient contact results in high interfacial resistance, and as porosity continues to develop during cycling, interfacial impedance rises further. This not only weakens the charge transfer efficiency between the CAM and the SE but may also induce local overpotentials and side reactions, accelerating capacity decay.[205]

Although co-sintering strategies have been proposed to improve interfacial contact, their effectiveness in enhancing ion/electron transport pathways and charge transfer efficiency remains limited.[53] For instance, Noguchi et al. fabricated a ASSSB using screen printing and hot-pressing techniques with NVP as the CAM and NZSP as the SE.[206] While no significant interfacial side reaction products were observed after 50 cycles, severe capacity decay occurred within the first five cycles due to loss of effective contact area between NVP and NZSP, leading to increased internal resistance. Lalère et al. employed field-assisted sintering technology/spark plasma sintering (SPS) to sinter electrodes and integrated NVP/NZSP/NVP cells at 900°C, obtaining dense self-supporting trilayer structures with good mechanical properties.[207] The battery operated at 1.8 V and achieved 85% of the theoretical capacity at 0.1C. However, volume changes in the NVP lattice during Na^+ insertion/extraction still inevitably led to macroscopic crack formation. Evidently, for dual-oxide systems, co-sintering cannot resolve interfacial contact failure due to the rigid nature of the particles, while potentially introducing additional issues such as secondary phase formation and significantly increased manufacturing costs.

4.3. Critical Challenges of Sulfide SE-Based ASSSBs

Most sulfide SEs, such as $Na_{10}GeP_2S_{12}$ and NPS, are limited by narrow electrochemical stability windows (typically below 3.0 V vs Na^+/Na), which leads to severe interfacial electrochemical incompatibility when paired with high-voltage oxide CAMs (as shown in **Figure 12**a).[208] Both theoretical calculations and experimental characterizations indicate that when the operating voltage exceeds ≈2.5 V, these SEs undergo oxidative decomposition, generating high-resistance interfacial products including elemental S, PS_x, P_2S_5, S—O and P—O bond-containing compounds.[7,209] These products generally function as both ionic and electronic insulators, forming a resistive layer at the interface that impedes Na^+ migration, resulting in significant irreversible capacity loss and rapid performance degradation. Taking the NPS/$NaCrO_2$ system as an example, theoretical predictions indicate that interfacial reactions generate Na_3PO_4, $NaCrS_2$, and the intermediate phase Na_3PSO_3. This mechanism has been experimentally verified: ASSSBs assembled with this system can only maintain a limited capacity of ≈60 mAh g^{-1}.[210] The observed degradation behavior closely resembles the formation mechanism of interfacial resistance layers in all-solid-state lithium-ion batteries (ASSLBs, e.g., $LiCoO_2$/Li_2S-P_2S_5 systems), both arising from continuous interfacial element exchange and the formation of stable impurity phases.[25,211] Therefore, although high-voltage oxide CAMs can enhance energy density, their practical application in sulfide-based ASSSBs requires interface engineering strategies to suppress these spontaneous interfacial reactions and improve long-term cycling stability.

To mitigate severe interfacial side reactions, low-working-potential (≤3 V vs Na^+/Na) transition metal sulfide CAMs—such as Na_2S, TiS_2, FeS_2, Sb_2S_4, and MoS_2—are widely employed in sulfide-based ASSSB systems owing to their high theoretical capacities, excellent interfacial compatibility with SEs, and intrinsically fast ionic/electronic conductivities.[111,212–215] These materials possess chemical potentials similar to those of sulfide SEs, theoretically ensuring good interfacial compatibility. However, in practical systems, significant volume changes lead to interfacial contact issues that still markedly limit their performance

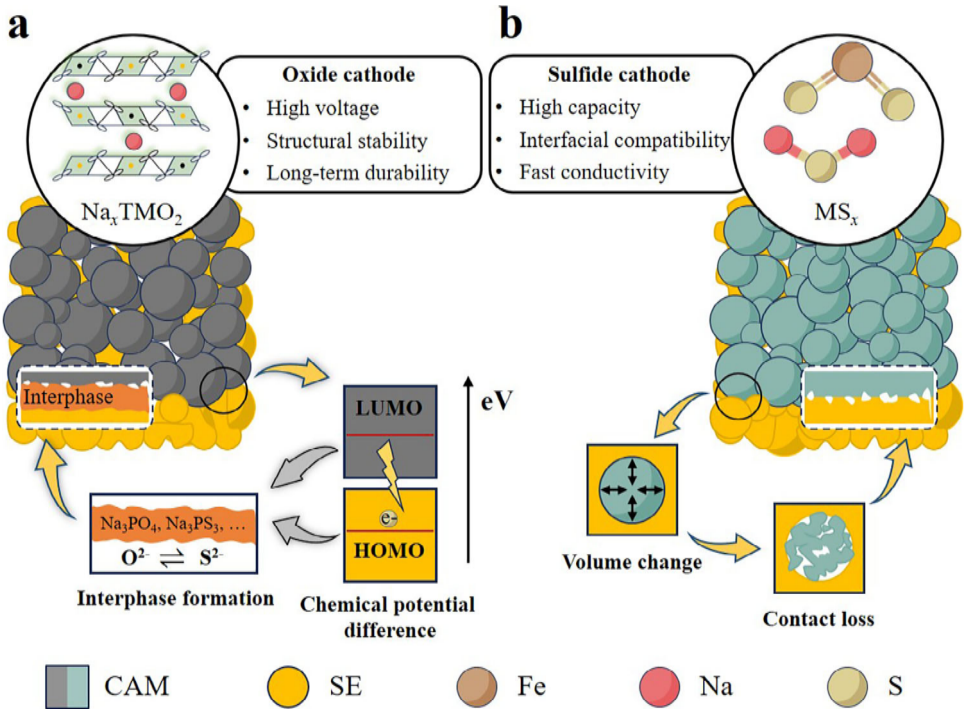

Figure 12. Schematic illustration of the challenges faced by sulfide SE–based ASSSBs when coupled with a) oxide or b) sulfide CAMs.

(Figure 12b). For instance, Hayashi et al. pioneered the development of room-temperature rechargeable ASSSBs using inorganic SEs, yet the practical capacity of TiS_2 cathodes reached only ≈40% of their theoretical value.[11] This low utilization is primarily attributed to insufficient solid-solid interfacial contact, indicating that further optimization of ion transport pathways through electrode structure design and interface engineering remains essential.

In summary, the main challenges of sulfide SE systems include: on one hand, high-voltage oxide CAMs induce interfacial chemical reactions and the formation of high-resistance layers, limiting capacity and cycling life; on the other hand, even low-voltage cathodes are constrained by insufficient physical contact with the SE, which significantly reduces CAMs utilization. Effective interface engineering and electrode structure optimization are thus critical to achieving high performance and long-term stability in sulfide-based ASSSBs.

4.4. Critical Challenges of Other Electrolyte-Based ASSSBs

In ASSSBs, hydride and halide SEs exhibit fundamentally similar interfacial challenges when paired with CAMs (As shown in **Figure 13**). Hydride SEs, owing to their narrow electrochemical stability window (<2.5 V vs Na^+/Na), are prone to interfacial oxidative decomposition when coupled with high-voltage CAMs (e.g., layered oxides), thereby forming high-impedance interfacial layers.[167,216] Clear evidence has been reported in ASSLB systems: when $LiBH_4$ is employed as the SE in combination with a $LiCoO_2$ cathode, the cell undergoes irreversible decomposition after ≈30 cycles.[217] Raman spectroscopy reveals that, alongside the attenuation of $LiCoO_2$ characteristic peaks, new signals corresponding to Co_3O_4 and CoO(OH) emerge, indicating that $LiBH_4$ readily reacts with the charged state of $Li_{1-x}CoO_2$. This interfacial side reaction leads to a dramatic increase in interfacial resistance, from an initial value of ≈400 Ω to nearly 10,000 Ω after

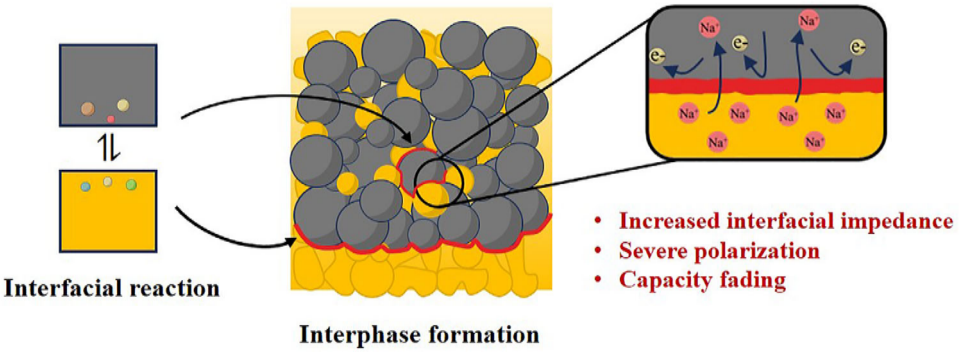

Figure 13. Interfacial side reactions between halide and hydride SEs and CAMs.

30 cycles, ultimately causing rapid performance degradation. These findings demonstrate that hydride SEs suffer from pronounced chemical instability when interfaced with high-voltage CAMs.

In contrast, halide SEs possess a high oxidation potential (>3.5 V vs Na^+/Na) and are therefore typically paired with high-voltage CAM (i.e., oxide CAMs). However, they can still face various interfacial challenges.[218] For instance, during the charging process, halide SEs can react with highly reactive O species released from layered oxide CAMs. These processes can lead to interfacial chemical instability, the formation of electronically insulating byproduct layers, or alterations in the cathode surface structure, thereby increasing interfacial resistance and reducing cycling stability. Relevant studies in Li^+ systems provide valuable insights. For example, during the 4.3 V phase transition, O_2 released from NCM85 can react chemically with $Li_{5/2}Y_{1/2}Zr_{1/2}Cl_6$, forming YOCl with limited chemical stability, which results in significant capacity decay during cycling.[219] Similarly, $Li_{2.6}Zr_{0.4}Ho_{0.6}Cl_6$ undergoes chemical reaction and decomposition when exposed to O_2 at voltages above 4.6 V.[220]

These lithium-based studies offer important guidance for Na SEs, indicating that analogous chemical and electrochemical degradation mechanisms may occur at the interface between high-voltage CAM and halide electrolytes. By controlling interfacial reactions, forming stable interphase products, and optimizing electrode-electrolyte contact, it is possible to improve the cycling stability and high-voltage tolerance of ASSSBs.

5. Ideal Cathode and Optimization Strategies: Interfacial Engineering and Materials Development

The solid-solid contact and chemical compatibility at the cathode-electrolyte interface present significant challenges. Ion diffusion and charge transfer heavily depend on the physical contact between the active materials, the electronic conductive network, and the SE on the cathode side. Chemical compatibility, on the other hand, is determined by the overlap of the electrochemical windows of the SE and the CAM. Given the varying physicochemical properties of different SEs, the interface issues they encounter are also distinct. For instance, sulfide-based SEs suffer from poor air stability and a narrow electrochemical stability window, making the resolution of (electro)chemical compatibility between the SE and the CAM a primary concern. In contrast, oxide-based SEs exhibit high mechanical strength and chemical stability, which shifts the focus to addressing contact issues at the interface.

In summary, an ideal cathode interface should possess characteristics of tight physical contact and wide (electro)chemical stability. Such features can effectively prevent the continuous degradation of both the electrode and the electrolyte, thereby ensuring stable battery's capacity and cycle performance. Therefore, resolving the interface challenges between the CAM and the SE is pivotal to advancing the development of ASSSBs.

This section provides a comprehensive review of the challenges faced at the interfaces between different types of SEs and CAMs. The discussion is organized around optimization strategies, including homogenization, coating, the construction of intermediate layers, and materials development (**Figure 14**).

5.1. Homogenization Engineering

In ASSSBs, homogenization engineering optimizes material composition, interfacial properties, and structural design to effectively address challenges such as interfacial mismatch, low ionic conductivity, and mechanical heterogeneity. This approach ultimately enhances battery performance and stability.

5.1.1. Homogenization of Material Composition

SEs and CAMs offer a diverse range of combinations, resulting in various composite systems. However, significant differences in their physicochemical properties often lead to undesirable interfacial reactions. For instance, sulfide-based SEs exhibit a limited electrochemical stability window and a chemical potential mismatch with oxide CAMs, causing issues such as thermodynamic instability and elemental interdiffusion upon contact. To mitigate severe interfacial side reactions, CAMs with anions identical to those in the SE can be selected to achieve a homogeneous composite cathode. Consequently, transition metal sulfides such as Sb_2S_3, FeS_2, and MoS_2—which share similar sulfide frameworks and exhibit low operating potentials ($\leq$ 3 V vs Na/Na^+)—have been extensively explored for sulfide-based ASSSBs.[111,148,212–214,221]

The similar chemical potentials of these transition metal sulfides and sulfide SEs ensure superior interfacial compatibility. Furthermore, their relatively weak M—S bonds facilitate improved electrochemical reversibility.[222] Hayashi et al. first fabricated a room-temperature rechargeable ASSSBs using NPS as the SE, although the achieved capacity was only ≈40% of the theoretical value of the TiS_2 cathode.[11] This limited utilization of CAMs was likely due to insufficient contact at the cathode/electrolyte interface. To address this, particularly for SEs and CAMs with low elastic moduli, nanosizing strategies have been employed to enhance interfacial contact and reduce ion transport distances within the composite cathode. Yue et al. developed composite cathodes by ball-milling nanosized and micron-sized Na_2S with NPS-C, forming NPS–nanosized Na_2S-C (NPS–nano-Na_2S-C) and NPS–micron-sized Na_2S-C (NPS–micron-Na_2S-C), respectively.[111] Electrochemical testing of Na-Sn-C|NPS|NPS–Na_2S-C cells revealed that NPS–nano-Na_2S-C exhibited superior capacity retention and rate performance compared to NPS–micron-Na_2S-C. Specifically, after 50 cycles, the reversible capacities of NPS–nano-Na_2S-C and NPS–micron-Na_2S-C were 438.4 and 103 mAh g^{-1}, respectively (**Figure 15a**). At current densities of 10, 20, 50, and 100 mA g^{-1}, NPS–nano-Na_2S-C delivered specific capacities of 1026, 944, 724, and 559 mAh g^{-1}, significantly outperforming NPS–micron-Na_2S-C, which exhibited 448, 261, 182, and 85 mAh g^{-1}, respectively. These experimental results confirm that nanosized NPS–Na_2S-C composites exhibit enhanced reaction kinetics, improved cycling stability, and higher active material utilization. Clearly, a homogeneous distribution and intimate contact among the CAM, ionic conductor, and electronic conductor facilitate uniform electrochemical reactions, leading to higher Coulombic efficiency and reversible capacity.

Another effective strategy to reduce interfacial resistance between the electrode and electrolyte is the in situ fabrication of

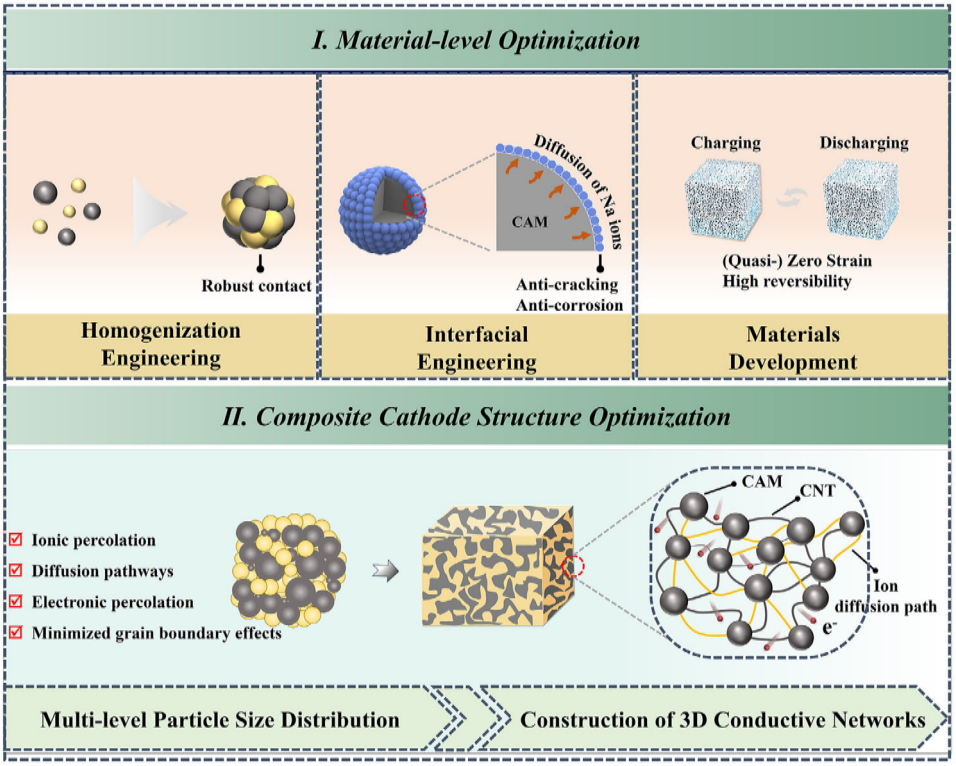

Figure 14. Optimization Strategies for ASSSB Cathode Interfaces.

composite materials containing both CAM and SE. For example, Wan et al. employed an in situ liquid-phase coating method to anchor nanosized $Na_{2.9}PS_{3.95}Se_{0.05}$ onto $Fe_{1-x}S$ nanorods. Scanning electron microscope (SEM), transmission electron microscopy (TEM), and scanning TEM (STEM) analyses confirmed the uniform and dense coating of $Na_{2.9}PS_{3.95}Se_{0.05}$ on the $Fe_{1-x}S$ surface, forming a $Fe_{1-x}S@Na_{2.9}PS_{3.95}Se_{0.05}$ core–shell structure.[223] As shown in Figure 15b, the $Fe_{1-x}S@Na_{2.9}PS_{3.95}Se_{0.05}$|Na ASSSB exhibited high capacity, and remarkable cycling stability, achieving an energy density of 910.6 Wh kg^{-1}, a power density of 201.6 W kg^{-1}, and an initial Coulombic efficiency of 89.6%. Similarly, Mo_6S_8 coated with NPS via a solution-based method demonstrated stable cycling performance over 500 cycles at 60 °C.[224] Fan et al. synthesized Na_2S–NPS–CMK-3 composite cathodes via an in situ casting and annealing process.[225] Compared to Na_2S–NPS–CMK-3 composites prepared by ball-milling, the in situ casting method resulted in tighter contact among Na_2S, NPS, and CMK-3, leading to higher capacity and improved cycling stability, as illustrated in Figure 15c.

5.1.2. Co-Sintering and In Situ Interface Construction

Oxide SEs are characterized by high thermodynamic stability and a wide electrochemical stability window. However, their rigid and rough surfaces often result in poor interfacial contact, which significantly hinders Na^+ diffusion kinetics across the interface. Furthermore, the 3D volume changes of CAMs during charge-discharge cycling exacerbate interfacial degradation, leading to rapid performance deterioration.[205] To optimize interfacial contact, the most commonly employed strategies involve co-sintering or in situ interface construction techniques.[53] For instance, Noguchi et al. fabricated composite electrodes via screen printing and hot pressing, incorporating NVP as the CAM and NZSP as the SE in a symmetric cell configuration.[206] Although no significant interfacial side reaction products were detected after 50 cycles, the progressive loss of effective contact area between NVP and NZSP resulted in increased internal resistance and severe capacity degradation. Similarly, Lalère et al. employed SPS to sinter the electrode and integrate an NVP/NZSP/NVP cell at 900 °C, yielding a dense, self-supporting trilayer structure with excellent mechanical properties.[207] This battery operated at 1.8 V and achieved 85% of the theoretical capacity at 0.1C. However, inevitable unit cell volume changes during Na^+ (de)intercalation led to the formation of macroscopic cracks in the electrode, ultimately compromising battery performance. These findings highlight the inherent limitations of co-sintering in inorganic SEs due to the rigid nature of their constituent particles. Additionally, this approach may introduce further complications, such as the formation of undesired secondary phases. To address these challenges, pulsed laser deposition (PLD) has been explored as a method for directly sputtering cathode thin films onto electrolyte surfaces. For example, Kehne et al. utilized PLD to deposit an Na_xCoO_2 cathode layer onto a $Na_{3.4}Sc_{0.4}Zr_{1.6}Si_2PO_{12}$ electrolyte, achieving a tightly bonded thin-film cathode/electrolyte interface.[101] Post-cycling microstructural analysis of the interface revealed no signs of delamination, voids, or cavities. In another study, in

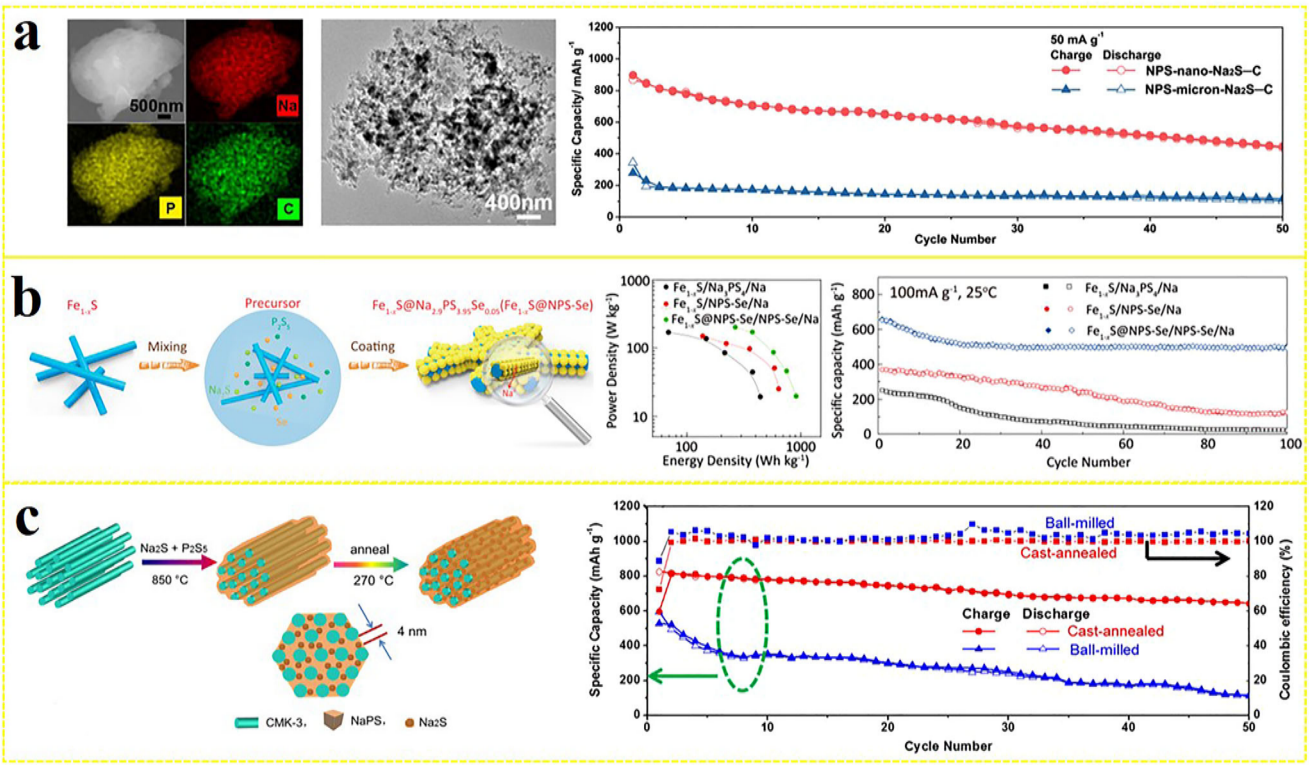

Figure 15. a) SEM image and elemental mappings of Na, P, and C as well as TEM image for the NPS-nano-Na_2S–C nanocomposite cathode (left), and corresponding to cycling performance (right). Reproduced with permission.[111] Copyright 2017, American Chemical Society. b) Schematic diagram of the preparation of $Fe_{1-x}S@Na_{2.9}PS_{3.95}Se_{0.05}$ and corresponding to Ragone plot of the batteries and Cycling performance of the batteries under a current density of 100 mA g^{-1}. Reproduced with permission.[223] Copyright 2018, American Chemical Society. c) Schematic illustration of the synthesis of cast-annealed Na_2S-NPS-C composite cathode and Cycling properties of ball-milled Na_2S-NPS-C composite and cast-annealed Na_2S-NPS-C nanocomposite cathodes at a current of 50 mA g^{-1}. Reproduced with permission.[225] Copyright 2018, American Chemical Society.

situ X-ray photoelectron spectroscopy (XPS) was employed to investigate interfacial formation during $NaCoO_2$ thin-film deposition onto Na-β''-Al_2O_3 and $Na_{3.3}Sc_{0.3}Zr_{1.7}(SiO_4)_2(PO_4)$ SEs.[226] While severe interfacial reactions were observed between Na-β''-Al_2O_3 and the cathode, only slight reductions in Zr and Sc content were detected near the cathode-side interface of $Na_{3.3}Sc_{0.3}Zr_{1.7}(SiO_4)_2(PO_4)$, suggesting minimal interfacial interactions between $NaCoO_2$ and $Na_{3.3}Sc_{0.3}Zr_{1.7}(SiO_4)_2(PO_4)$. This indicates that the deposition process does not induce significant interfacial reactions, making this interface promising for reducing cathode-side overpotential. While thin-film electrodes effectively resolve interfacial contact issues and achieve exceptionally low electrode/electrolyte interfacial resistance,[227,228] certain limitations must be acknowledged. First, the absence of interfacial failure phenomena—such as cracking—observed in thin-film electrode cells is likely due to the limited content of CAMs. As a result, the stress generated during Na^+ insertion and extraction may not reach the critical threshold required to induce interfacial strain, thereby avoiding significant microstructural changes. Second, thin-film electrodes typically lack electronic and ionic conductive additives, which significantly constrains the selection of compatible CAMs. Only materials with intrinsically high electronic and ionic conductivities, such as $NaCoO_2$, are generally suitable for such designs. Lastly, the inherently low areal loading of thin-film electrodes imposes a limitation on the achievable capacity of the cell, posing a challenge for practical and commercial applications.[229]

A rationally designed electrolyte and electrode structure can also improve interfacial contact. For example, Lan et al. developed a chemical infiltration method to introduce an NVP precursor solution into the porous structure of $Na_{3.4}Zr_2Si_{2.4}P_{0.6}O_{12}$ electrolyte, enabling the in situ construction of a 3D composite electrode.[230] This design led to the formation of a nanoscale NVP layer tightly bonded to the SE scaffold, thereby facilitating rapid Na^+ transport. At the same time, the residual open porosity left in the structure played a beneficial role in accommodating volume changes during cycling, helping to mitigate interfacial stress accumulation and preserve mechanical integrity.

5.2. Interfacial Phase Engineering

In ASSSBs, interfacial phase engineering effectively addresses key issues such as mechanical stress-induced failure and electrochemical side reactions by controlling the chemical and physical properties of the CAM-SE interface.[231] By designing stable transition layers, optimizing interface microstructures, and introducing elastic or highly conductive interfacial phases, the interfacial stability, ion transport efficiency, and cycling performance of solid-state batteries can be significantly improved.

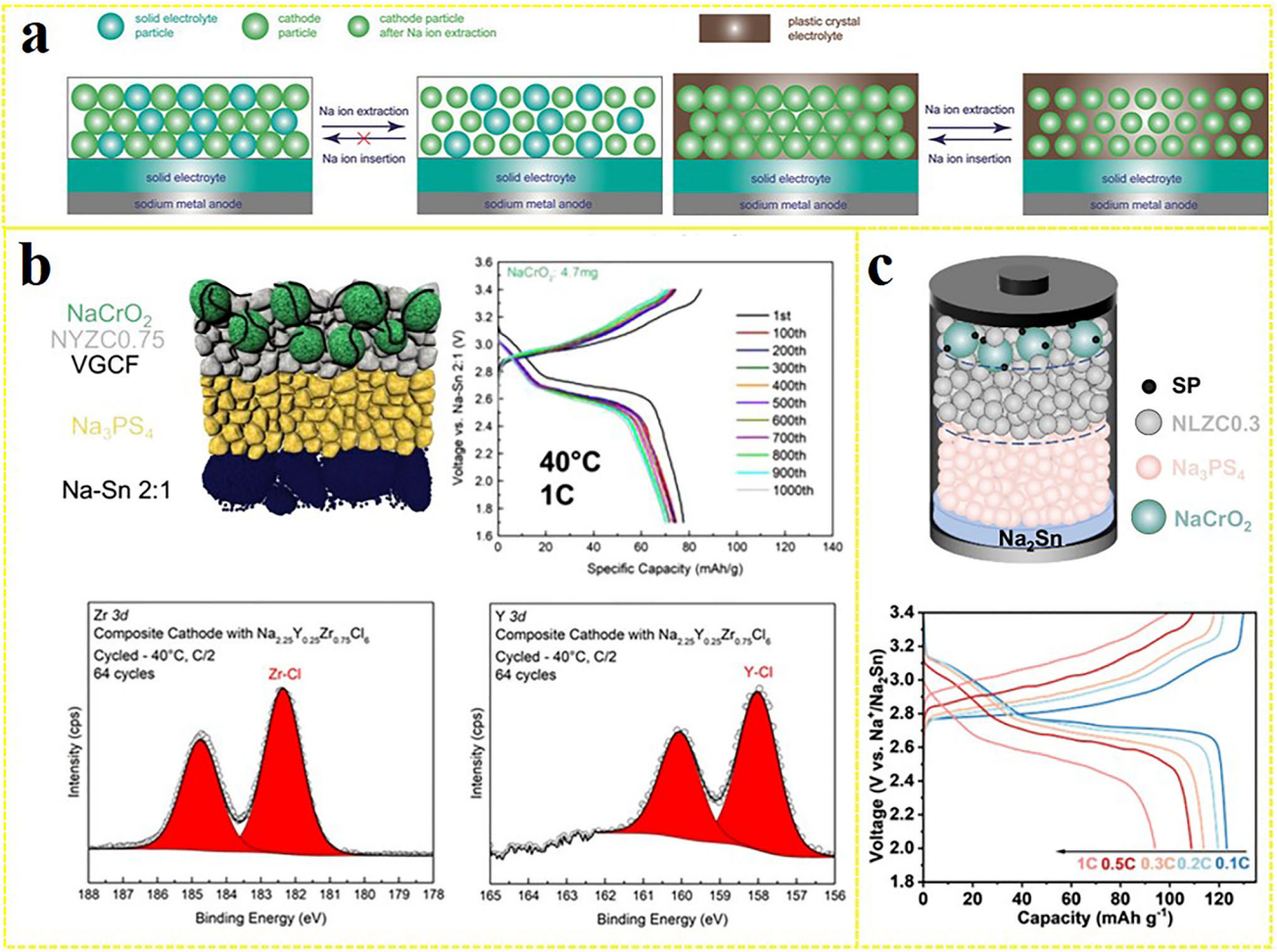

Figure 16. a) Schematic diagrams of ASSSBs with $Na_2Zr_2Si_2PO_{12}$ particles (left) or plastic-crystal electrolyte (right) in the cathode. Reproduced with permission.[205] Copyright 2017, Wiley-VCH. b) ($NaCrO_2$: $Na_{2.25}Y_{0.25}Zr_{0.75}Cl_6$: VGCF)/NPS/$Na_2Sn$ cell schematic and charge–discharge curves for selected cycles at 40 °C and 1 C and XPS spectra of the cycled $Na_{2.25}Y_{0.25}Zr_{0.75}Cl_6$-containing Composite Cathode, Zr 3d and Y 3d binding energies for the composite cathode cycled at 40 °C and C/2. Reproduced with permission.[35] Copyright 2021, Nature Publishing Group. c) Configuration of ASSSB with NLZC0.3-HM as SEs and charge-discharge profiles at different currents (0.1C, 0.2C, 0.3C, 0.5C, 1C between 2 and 3.4 V vs Na/Na^+, 30 °C). Reproduced with permission.[167] Copyright 2024, Nature Publishing Group.

5.2.1. Interface Layers

To address severe interfacial issues in ASSSBs, plasticizers or highly extensible polymers are commonly used as interface coatings or composite components in the cathode to improve interfacial contact and provide buffer space for volume changes. For example, Gao et al. introduced a plastic-crystal Na^+-electrolyte interphase composed of succinonitrile complexed with a sodium salt between the SE NZSP and the CAM NVP.[205] Compared to cells without the plastic-crystal Na^+-electrolyte, those incorporating the plastic-crystal electrolyte exhibited a higher exchange current density (8.67 vs 3.35 mA cm^{-2}), indicating that the integration of the plastic-crystal electrolyte accelerated the electrochemical reaction rate, i.e., reduced the charge transfer impedance, enabling a discharge capacity of 77 mAh g^{-1} at 5C. As shown in **Figure 16a**, the stable cycling performance and excellent rate capability are attributed to the ability of the plastic-crystal Na^+-electrolyte to permeate and contact most of the CAM, where it undergoes reversible deformation with volume changes of the active particles, maintaining interfacial contact during repeated charge-discharge cycles. Furthermore, the combination of flexible polymer electrolytes and high ionic conductivity electrolytes to prepare composite electrolytes has been demonstrated to effectively enhance Na^+ conductivity, suppress dendrite formation, improve interfacial wettability, and reduce interface-related issues.[232] Wu et al. combined a polymer (polyethylene oxide, PEO) and an ion conductor material (Ga-doped $Na_2Zn_2TeO_6$, NZTO) to fabricate a highly flexible and highly ion-conductive composite SE, which effectively ensured good electrode/electrolyte contact and low resistance.[233] In the study conducted by Kim et al., a conductive polymer electrolyte (Na-SPE) composed of a mixture of PEO, sodium salt, and an ionic liquid was successfully integrated with a NASICON-type SE for use in seawater batteries.[234] Although not strictly a solid-state battery, this system demonstrates the potential of polymer–inorganic hybrids to alleviate interfacial challenges in solid-state configurations. Chi et al. discovered that a

composite cathode of pyrene-4,5,9,10-tetraone-poly(ethylene oxide) (PTO-PEO) exhibited a uniform, dense structure and formed a tight contact interface with the Na-β''-Al_2O_3 electrolyte.[235] This composite cathode demonstrated excellent electrochemical performance, achieving an initial discharge capacity of 362 mAh g^{-1} and 95% Coulombic efficiency in a Na-based battery. When there is a significant disparity in properties between the CAM and the SE, it is crucial to avoid direct contact between the SE and the CAM to ensure unaffected electrochemical performance. For instance, the FeS_2|polydopamine-$Na_{3.4}Zr_{1.9}Zn_{0.1}Si_{2.2}P_{0.8}O_{12}$|Na all-solid-state battery reported by Yang et al. exhibited high performance (236.5 mAh g^{-1} at 0.1C for 100 cycles).[34] This performance was attributed to the introduction of a polydopamine (PDA) layer, which not only acted as a buffer layer for volume changes but also ensured the structural integrity and tightness of the interface during cycling. However, it should be noted that although polymers can buffer volume changes and improve wettability, their limited electrochemical stability window (below 3.7 V vs Na^+/Na) limits their application in high-voltage ASSSBs.[236]

An ideal interfacial layer should exhibit not only thinness, uniformity, and excellent wettability but also demonstrate superior ionic conductivity and robust resistance to high-voltage oxidative decomposition. In the $NaCrO_2$-NPS|Na-Sn full battery, the NPS electrolyte was oxidized, resulting in the formation of elemental sulfur, PS_x compounds, and P—O bond-containing compounds.[35] To obtain a stable cathode/electrolyte interface, Wu et al. selected the stable $Na_{2.25}Y_{0.25}Zr_{0.75}Cl_6$ (NYZC0.75) in combination with $NaCrO_2$ as the CAM (Figure 16b).[35] Under room-temperature conditions, the battery exhibited a first-cycle Coulombic efficiency of 97.6%. Even at 40°C, it demonstrated stable electrochemical performance with a capacity retention of 89.3% after 1C cycling for 1000 cycles. Furthermore, XPS analysis showed no evidence of electrochemical decomposition products, indicating that NYZC0.75 effectively protected NPS from oxidation by $NaCrO_2$. In another study, a $NaCrO_2$|NLZC0.3-HM|NPS|Na_2Sn ASSSB with a buffer layer of $Na_{0.7}La_{0.7}Zr_{0.3}Cl_4$ (NLZC0.3-HM) exhibited an initial discharge capacity of 123 mAh g^{-1} (0.1C, 30°C) and maintained a high capacity of 94 mAh g^{-1} at 1C (Figure 16c).[167] Similarly, Lin et al. demonstrated an ASSSB employing a $Na_{0.85}Mn_{0.5}Ni_{0.4}Fe_{0.1}O_2$ (NMNFO) and a Na_2O_2-$HfCl_4$-based SE, achieving an initial discharge capacity of 125.5 mAh g^{-1} at 0.1C and a Coulombic efficiency exceeding 99.9%, which is comparable to the performance of liquid-phase batteries using the same NMNFO cathode.[36] This demonstrates that the use of high-voltage-stable sodium halide materials as a buffer layer between oxide CAMs and SEs can effectively resolve interface issues and enhance overall battery performance.

As the understanding of the degradation drivers at the cathode/electrolyte interface deepens, it has been suggested that to avoid anion exchange reactions, elements such as Sb, Ge, Sn, or as can be used to completely or partially substitute phosphorus (P) in sulfide SEs. Alternatively, poly-anionic cathode materials with stable PO_4 groups, such as NVP or $NaFePO_4$, can be utilized.[237]

5.2.2. Non-Solid Interfacial Layer Construction

Introducing small amounts of liquid phases capable of conducting Na^+, such as organic liquid electrolytes or ionic liquids, at the cathode/electrolyte interface can fill uncontacted voids and convert the non-contact state into a solid-liquid-solid interfacial mode, thereby enhancing Na^+ transport kinetics.[238,239] Liu et al. constructed an ion-electron conductive network by incorporating functional ionic liquid, N-butylN-methylpyrrolidinium bis(fluorosulfonyl)imide, PY14FSI, and conductive carbon, which was coated onto the CAM, transforming point contacts between solid particles into area contacts (**Figure 17a**).[98] This resulted in high-rate cycling stability, with a capacity retention of 90% after 10,000 cycles at 6C in a Na-β''-Al_2O_3-based electrolyte and $Na_{0.66}Ni_{0.33}Mn_{0.67}O_2$ cathode. Following this, the use of the N-methyl-N-propylpiperidinium-bis(fluorosulfonyl) imide, PP13FSI, ionic liquid also demonstrated satisfactory effects on interface optimization (Figure 17b).[102] While organic liquid electrolytes can be used as interface wetting agents, they are less effective than non-volatile, highly stable ionic liquids. For example, Zhang et al. found that using an ethylene carbonate-dimethyl carbonate $NaPF_6$ salt ($NaPF_6$/EC-DMC) solution as an interface wetting agent reduced interface resistance to tens of Ohms and significantly lowered polarization.[102] However, organic liquid electrolytes tend to volatilize or decompose during cycling, limiting their passivation effect over time. This is reflected in a sharp capacity drop after ≈250 cycles. Moreover, it is important to note that the effectiveness of liquid-phase additives largely depends on their wetting behavior and viscosity on the solid surface.[240,241] Vogl et al. found that protic ionic liquid electrolytes, when combined with NVP, achieved excellent performance in SIBs, but this effect was not observed when used with $Na_{0.67}Mn_{0.89}Mg_{0.11}O_2$, highlighting the limited applicability of liquid-phase additives.[242]

5.3. Materials Development

The development of ASSSBs relies on the advancement of new CAMs, SEs, and innovative material design strategies to overcome key challenges such as interface stability, ion/electron conductivity, and mechanical compatibility. For CAMs, it is essential to develop high-voltage, zero-strain materials with excellent electronic and ionic conductivity. These properties contribute to improved interfacial stability and enhanced redox kinetics. For SEs, improvements in ionic conductivity, optimization of interface contact, and enhancement of chemical stability are necessary to reduce interfacial impedance and side reactions. Of particular interest is the emerging direction of "all-in-one" integrated cathode materials, which incorporate both ionic and electronic conduction functions within a single material. This approach effectively circumvents heterogeneous interface issues while significantly improving electrode energy density and structural stability. Through multi-level material innovations, interface optimization, and synergistic nanostructuring effects, ASSSBs can achieve higher energy density, longer cycle life, and improved safety, thereby advancing the development of next-generation energy storage technologies.

5.3.1. Novel Cathode Materials

The stability of the CAM/SE interface represents a major challenge for ASSSBs. For CAMs, the development of zero-strain

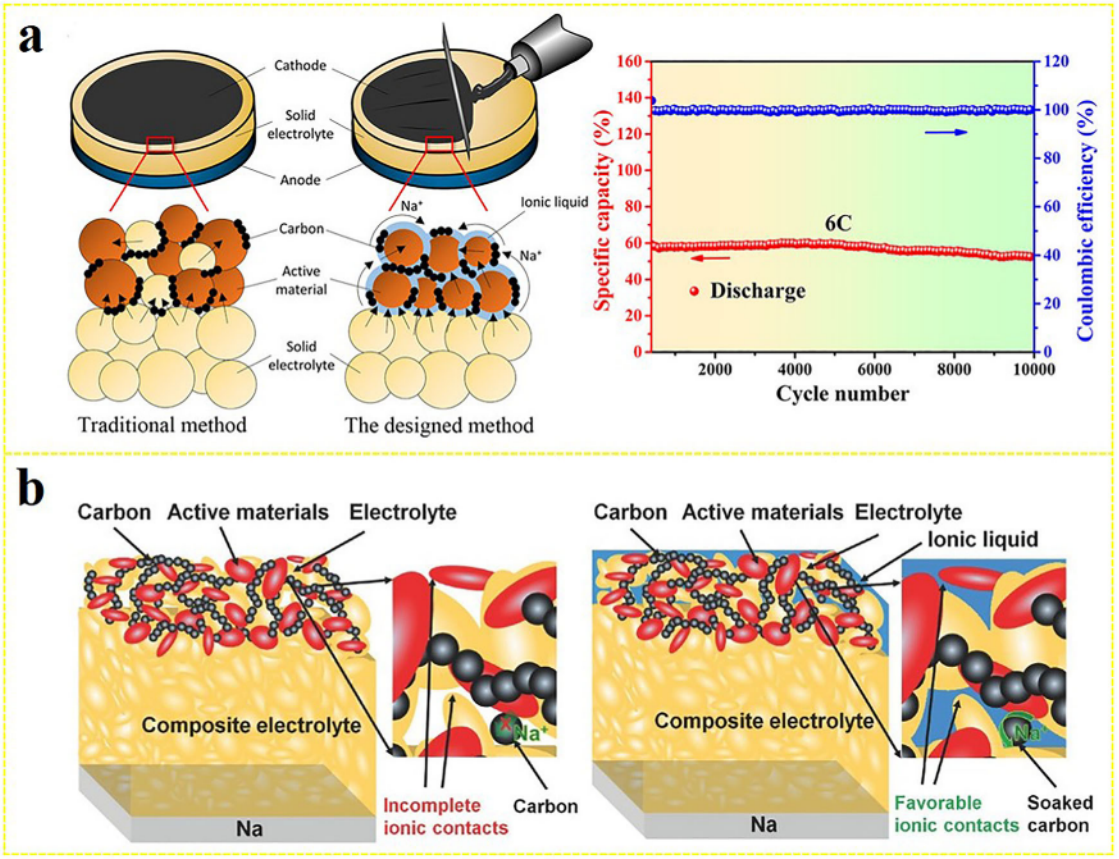

Figure 17. a) Schematic diagrams of a conventional sintering type and the designed new type ASSSB based on an inorganic ceramic electrolyte (left), and new type ASSSB corresponding to long-term cycling performance (right). Reproduced with permission.[98] Copyright 2016, Wiley-VCH. b) Schematic representation of the NVP/SE/Na and NVP/IL/SE/Na solid-state batteries. Reproduced with permission.[102] Copyright 2017, Wiley-VCH.

materials is essential to minimize lattice volume changes during Na^+ insertion and extraction, effectively preventing material structure collapse and degradation of interfacial contact, thereby significantly extending battery life. Additionally, stable crystal structures help maintain efficient ion transport channels, enhancing rate performance and enabling fast charging and discharging. Notably, "all-in-one" integrated cathode materials, which inherently combine both ionic and electronic conduction, fundamentally circumvent issues associated with heterogeneous interfaces while simultaneously simplifying electrode structure and improving energy density. The integration of zero-strain characteristics with the "all-in-one" design concept holds significant promise for substantially extending battery cycle life. Therefore, both categories of materials are critically important for constructing highly stable and reliable ASSSBs.

PBAs are typical zero-strain cathode materials for SIBs. For instance, Jing et al. enhanced the reversibility and kinetics of redox reactions in FeVO-PBA cathodes by leveraging the d-d interactions between late-transition metal (Fe) and early-transition metal (V) to achieve charge compensation, while simultaneously improving electronic conductivity and structural stability, with a maximum unit cell volume change of only 1.74%.[129] Furthermore, NASICON-structured materials also exhibit zero-strain characteristics. For example, $NaTi_2(PO_4)_3$ has been extensively studied in liquid-phase SIBs due to its minimal volume variation during Na^+ insertion/extraction.[243,244] Zhao et al. developed a $NaTi_2(PO_4)_3$-gel composite electrode that tightly adheres to dense Na-β/β''-Al_2O_3 ceramic membranes, achieving low interfacial polarization between the cathode and electrolyte.[103] Beyond conventional frameworks, high-entropy strategies have recently emerged as an effective method to further improve cathode performance. Jin et al. successfully synthesized a high-entropy $Na_{3.4}VMn_{0.2}Fe_{0.2}Al_{0.3}Cr_{0.3}(PO_4)_3$ via a sol-gel method.[245] By exploiting entropy-driven multi-cation redox reactions, enabled multi-electron transfer reactions. Notably, this high-entropy strategy not only enhanced specific capacity and energy density, but also demonstrated exceptional zero-strain behavior, with a volume change of merely 1.33% during cycling.

For Na^+ layered cathodes, irreversible phase transitions and volume expansion can be mitigated by restricting the charge/discharge cutoff voltage or introducing pillar ions (e.g., K^+, Mg^{2+}, and Zn^{2+}) into the alkali metal layer.[246–248] For instance, Chu et al. enhanced the structural stability and optimized the electrochemical performance of layered cathodes through a Na-site pinning strategy with controlled defect introduction.[249] A 2.5% Fe^{3+} occupancy in the Na sites of $Na_{0.67}Mn_{0.5}Co_{0.5-x}Fe_xO_2$ effectively suppresses interlayer sliding and improves structural stability, achieving an ultralow volume variation of only

0.6% while maintaining continuous 2D channels for Na^+ transport. To simultaneously achieve high capacity and near-zero-strain characteristics, Wu et al. designed a P2-type dual-site substituted $Na_{0.7}Li_{0.03}[Mg_{0.15}Li_{0.07}Mn_{0.75}]O_2$ (NMLMO).[250] Density functional theory (DFT) calculations and in situ characterizations revealed that Li in the transition metal layer forms localized Na-O-Li configurations to enhance capacity, while Li in the alkali metal layer acts as rigid LiO_6 pillars to eliminate the P2-OP4 and P2-P′2 phase transitions during cycling. Benefiting from this dual-site synergy, the NMLMO cathode delivers a high specific capacity of 266 mAh g^{-1} and exhibits a single-phase solid-solution reaction mechanism across a broad voltage range of 1.5-4.6 V, accompanied by a lattice volume change of merely 1.2%.

Further development of zero-strain CAMs for SIBs can also be guided by theoretical simulations. Drawing from the development experiences of Li^+ cathodes, Zhao et al. systematically studied the effects of transition metal chemistry, cation ordering, Li-site occupancy, redox-inert substances, anion substitution, and cation migration on volume changes of cathode materials. They established general principles for designing low-strain cathodes based on FCC anion framework materials.[251] Additionally, materials such as spinel $Li_4Ti_5O_{12}$, $LiCrTiO_4$, and $LiY(MoO_4)_2$, which exhibit negligible volume changes during charge-discharge cycling, may serve as analogs for exploring sodium-ion CAMs.[252–254]

The recently developed halide material $Li_{1.3}Fe_{1.2}Cl_4$ in lithium-based systems demonstrates remarkable potential for the "all-in-one" design concept.[255] This material exhibits not only excellent mixed Li^+/e^- conductivity (2.28×10^{-4} and 6.98×10^{-5} S cm^{-1}, respectively) but also unique dynamic mechanical properties and self-healing capabilities. These characteristics provide valuable guidance for developing corresponding "all-in-one" materials in ASSSB systems.

To date, most of the reported CAMs have a crystalline structure, with amorphous CAMs being relatively limited. The open and random structure of amorphous materials can provide additional stable sites for cations, enhancing capacity and improving cycling performance. Nagata et al. proposed that the use of sodium oxyacid to promote the amorphization of transition metal layered oxides is an effective approach to obtain new high-capacity materials.[256] Experimental results show that by co-ball milling $Na_{0.7}CoO_2$ with $NaNO_3$, an amorphous structure of $80Na_{0.7}CoO_2{\cdot}20NaNO_3$ can be obtained, improving both ion conductivity and deformability. When compared to $Na_{0.7}CoO_2$ crystalline materials, this material shows higher discharge voltages and larger capacities (**Figure 18a**).

Compared to mainstream inorganic cathode materials, organic cathodes offer advantages such as abundant resources, low cost, and environmental friendliness, eliminating the dependence on scarce metals. Their tunable redox potential and mechanical flexibility facilitate the formation of stable and tight electrode-electrolyte interfaces, making them highly promising as cathode materials.[165,257] In 2018, Chi et al. first reported $Na_4C_6O_6$ as a cathode material.[47] The $Na_4C_6O_6$|NPS|$Na_{15}Sn_4$ full battery delivered a specific capacity of 184 mAh g^{-1} and an energy density of 395 Wh kg^{-1}, maintaining 70% of its capacity after 400 cycles at 0.2C (Figure 18b). XRD and XPS analysis of the cycled cathode showed no new peaks, further confirming the excellent physical and chemical stability between $Na_4C_6O_6$ and NPS. To further enhance energy density, the researchers subsequently reported a quinone, pyrene-4,5,9,10-tetraone (PTO) cathode material, demonstrating superior theoretical capacity (409 mAh g^{-1}) and elevated operating potential (2.2 V vs Na^+/Na).[116] Batteries based on PTO composite cathodes achieved an energy density of up to 587 Wh kg^{-1} and retained 89% capacity after 500 cycles at 0.3C. As shown in Figure 18c, in situ EIS revealed reversible interfacial resistance evolution during cycling, primarily observed as a reversible increase in the Warburg coefficient (A_w) during charging and a reversible decrease during discharging. Ex situ XPS and ToF-SIMS results further confirmed that this reversible behavior was primarily attributed to the highly reversible interactions between NPS and the resistive phase within the voltage range of 1.1–3.1 V. Furthermore, the relatively low Young's modulus exhibited by PTO (4.2 ± 0.2 GPa) contributed to effective stress redistribution during cyclic loading while ensuring consistent interfacial adhesion. Therefore, the reversible resistance and tight contact at the electrode-electrolyte interface collectively contributed to the outstanding battery performance. To prevent nucleophilic attack on the redox-active quinone groups, Ji et al. designed poly-(anthraquinonyl sulfide)-graphene (PAQS-G) with a stable polymer framework.[258] The chemically protected quinone groups demonstrated better chemical compatibility with sulfide electrolytes. After 300 cycles at 60°C, the PAQS-G cathode maintained a capacity retention of 95.5%. In conclusion, organic cathodes with moderate redox potentials can achieve electrochemically stable cathode-electrolyte interfaces, while their low Young's modulus ensures tight interface contact during cycling. These advantages together contribute to exceptional battery performance.

5.3.2. Novel SEs

Hydride SEs have emerged as a promising research direction for ASSSBs due to their high Na^+ conductivity, excellent chemical stability, and mechanical flexibility. Yoshida et al. discovered that ball milling $Na_2B_{10}H_{10}$ and $Na_2B_{12}H_{12}$ in a 1:3 molar ratio resulted in the highest ionic conductivity (**Figure 19a**).[259] A ASSSB employing $Na_2B_{10}H_{10}$-$3Na_2B_{12}H_{12}$ as the electrolyte and TiS_2 as the cathode demonstrated a high specific capacity of 237 mAh g^{-1}, approaching the theoretical value of $NaTiS_2$. When complex hydrides are applied in ASSSBs, considerations beyond ionic conductivity, such as chemical and electrochemical stability, become crucial. Duchêne et al. employed $Na_2(B_{12}H_{12})_{0.5}(B_{10}H_{10})_{0.5}$ as a SE and utilized an infiltration-based cathode fabrication method to form a stable interface with a $NaCrO_2$ cathode, enabling reversible and stable cycling at 3.25 V (Figure 19b).[99] Subsequently, they reported a method for crystallizing closo-borate SEs directly from solution and applied them to battery electrodes by infiltrating porous cathode materials (Figure 19c).[260] Experimental results revealed that $Na_4(B_{12}H_{12})(B_{10}H_{10})$ crystallized within the open voids of the electrodes, exhibiting a suitable crystal structure that provided high ionic conductivity (1 mS cm^{-1} at 25°C) and ensured effective contact with the CAM. An ASSSB using $NaCrO_2$ as the infiltrated cathode achieved stable high-rate cycling at 5C (4.5 mA cm^{-2}). Moreover, constructing stable cathode-electrolyte phases has proven effective in optimizing interfacial performance and expanding the electrochemical stability window of SEs at high voltages. When $Na_4(CB_{11}H_{12})_2(B_{12}H_{12})$

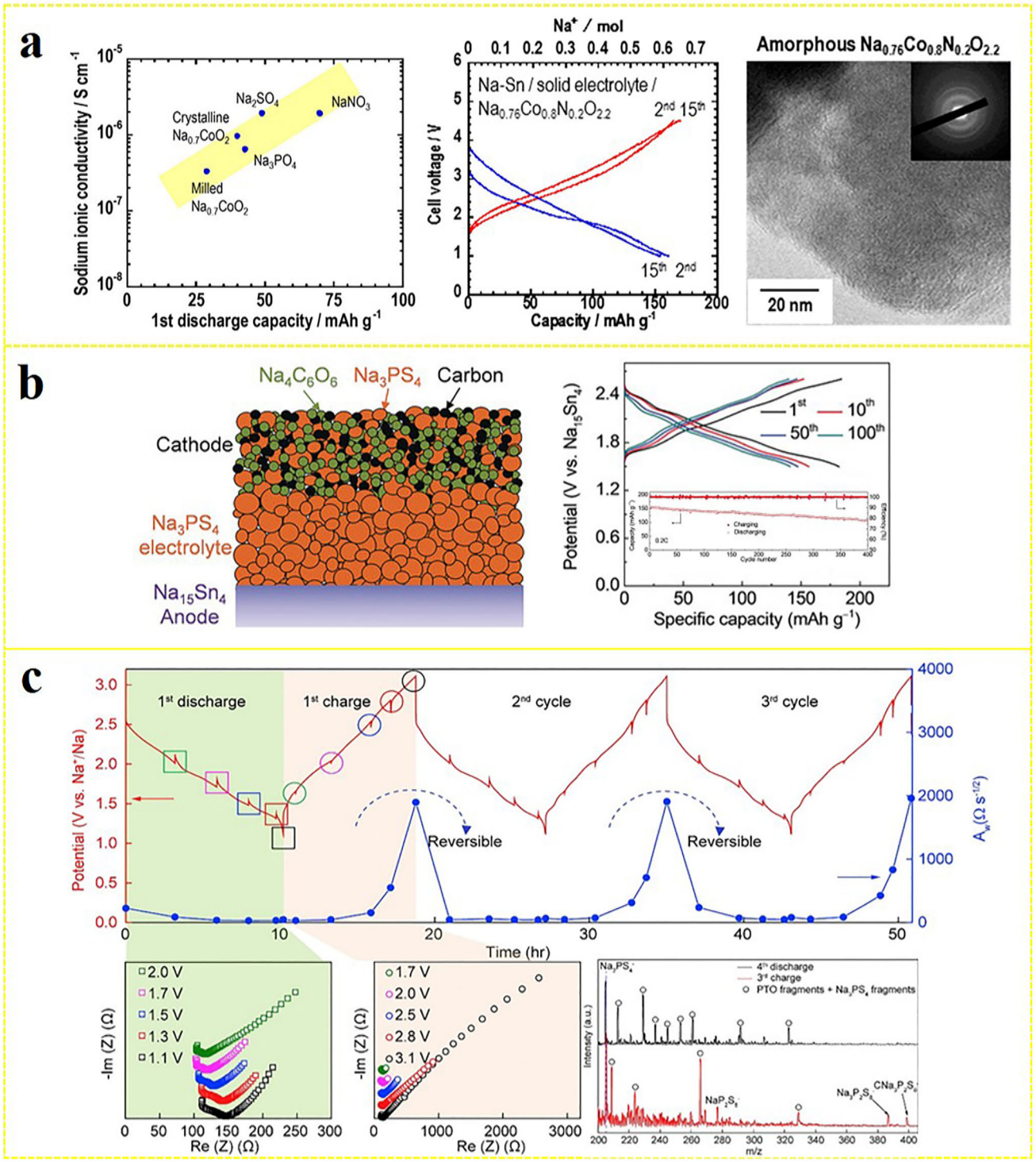

Figure 18. a) HR-TEM image and electron diffraction pattern, Na^+ conductivity vs first discharge capacity of the $Na_{0.7}CoO_2$–Na_xMO_y (M = N, S, or P) active materials, milled $Na_{0.7}CoO_2$, and crystalline $Na_{0.7}CoO_2$ and Charge–discharge curves for the cell prepared using a composite electrode of $Na_{0.76}Co_{0.8}N_{0.2}O_{2.2}$ and NPS Reproduced with permission.[256] Copyright 2018, American Chemical Society. b) Schematic of the ASSSBs and charge/discharge voltage profiles for selected cycles at 0.1C at 60 °C (Inset: Capacity and coulombic efficiency vs cycle number at 0.2C at 60 °C). Reproduced with permission.[47] Copyright 2018, John Wiley and Sons Ltd. c) Intermittent galvanostatic voltage profile for the first three cycles, and Warburg coefficient is extracted from the low-frequency impedance spectra. ToF-SIMS spectra of the composite cathodes at fully discharged and charged states. Reproduced with permission.[116] Copyright 2019, Cell press.

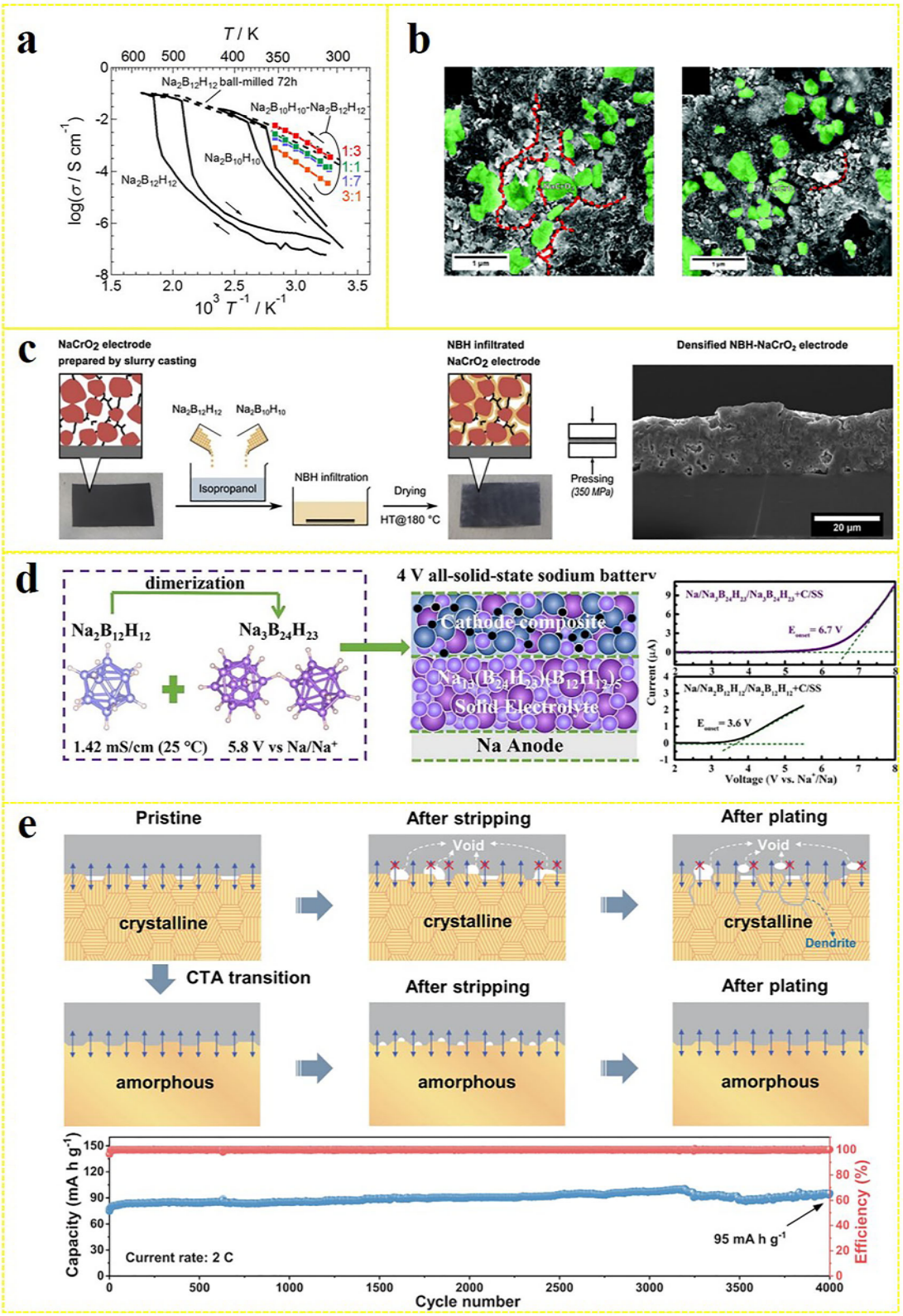

Figure 19. a) Na^+ conductivities for $Na_2B_{10}H_{10}$-$Na_2B_{12}H_{12}$ pseudo-binary complex hydride with various molar ratios ball-milled for 5 h. Different symbols denote $Na_2B_{10}H_{10}$-$Na_2B_{12}H_{12}$ molar ratios of 3:1(orange), 1:1(green), 1:3(red), and 1:7(blue). Reproduced with permission.[259] Copyright 2017, American Institute of Physics. b) Top-view SEM images of the mixed and impregnated cathode mixtures after pressing into a pellet. Cathode particles and cracks are highlighted by green areas and red lines, respectively. Reproduced with permission.[99] Copyright 2017, Royal Society of Chemistry.

was used as the SE, $[B_{12}H_{12}]^{2-}$ decomposed into electrochemically inactive products below 4.2 V, while $[CB_{11}H_{12}]^{-}$ remained intact, ensuring sufficient ionic conductivity.[107] This strategy effectively passivated the interface for 4V-class cathodes and prevented impedance growth during cycling. Previous studies indicated that a co-cross-linked borohydride electrolyte, $Na_2B_{20}H_{18}$, exhibited a wider electrochemical stability window compared to its monomeric form, $Na_2B_{10}H_{10}$, suggesting that the interconnection of borane clusters enhances electrochemical oxidation stability.[261] Inspired by this, Jin et al. developed a $Na_3B_{24}H_{23}$-$5Na_2B_{12}H_{12}$ SE for 4V-class ASSSBs. A $Na[Ni_{1/3}Fe_{1/3}Mn_{1/3}]O_2|Na$ battery incorporating this electrolyte exhibited an 84% capacity retention after 100 cycles at 0.1C within the voltage range of 2.0–4.2 V at 60 °C (Figure 19d).[262] Additionally, He et al. were the first to report $Na_2NH_2B_{12}H_{12}$, which crystallizes in the $Pna2_1$ space group. As demonstrated by CV testing, this material exhibited an impressive electrochemical stability window of 10V, providing new possibilities for the development of higher-voltage ASSSBs.[263]

Beyond the development of novel SEs, identifying new working mechanisms for SEs is equally significant. Sun et al. proposed a promising transition mechanism, in which an in situ electrochemically induced crystalline-to-amorphous transformation (CTA) occurs from the surface to the bulk of the SE. This transformation is primarily driven by lattice stress generated during repeated Na^+ transport, leading to the conversion of crystalline $Na_5SmSi_4O_{12}$ into its amorphous form (Figure 19e).[264] Benefiting from the enhanced ionic transport and superior interfacial properties provided by the amorphous $Na_5SmSi_4O_{12}$, the $Na|Na_5SmSi_4O_{12}|NVP$ battery exhibited an outstanding cycle life exceeding 4000 cycles, with both coulombic efficiency and capacity retention reaching 100%. Furthermore, the initial coulombic efficiency of 99% indicated the absence of irreversible side reactions between $Na_5SmSi_4O_{12}$ and either the sodium anode or the NVP cathode.

5.4. Optimization of Composite Cathodes

Composite cathodes play a crucial role in ASSSBs, as each component plays a distinct yet interdependent role: the CAMs serve as the primary host for Na^+ storage; conductive additives establish electronic percolation pathways; binders maintain structural cohesion; and SEs ensure effective ionic transport. The rational design and synergistic integration of these components are essential to realize high ion/electron conductivity, low interfacial impedance, and robust mechanical integrity. Although many CAMs exhibit moderate intrinsic electronic conductivity, conductive carbon additives are typically introduced to establish a continuous electronic network. This approach enhances current homogeneity, suppresses localized overcharging, and improves rate capability. However, the type and amount of carbon introduced must be carefully controlled, as carbon additives can catalyze interfacial decomposition of sulfide SEs, thereby accelerating battery degradation. For instance, Han et al. reported that excessive carbon incorporation into LGPS (at a carbon-to-LGPS weight ratio of 25:75) resulted in severe LGPS decomposition.[265] Oh et al. further investigated composite electrodes comprising acetylene black and LGPS, where CV measurements revealed continuous oxidation currents at the interface. The formation of decomposition products was found to hinder electron and/or Li^+ transport within the composite material.[189] Zhang et al. systematically studied the effects of different carbon additive types and mass fractions on the electrochemical behavior of solid-state batteries.[187] Compared with carbon-free electrodes, carbon-containing composite cathodes exhibited an additional sloping voltage profile before the 3.3 V plateau during the first charge cycle, which was attributed to severe oxidation of the SE at the onset of charging. XPS analysis further demonstrated that carbon at the CAM/SE interface facilitated the accelerated electrochemical decomposition of the SE by driving lithium with a lower chemical potential deeper into the electrolyte, thereby expanding the decomposition region. Collectively, these findings indicate that carbon additives in sulfide-based ASSSBs promote the electrochemical degradation of SEs, ultimately compromising battery cycle life. These results also highlight another critical issue associated with ASSSBs: SEs within composite cathodes decompose at any location where they come into contact with electronic pathways, such as current collectors. Since decomposition reactions predominantly occur at the surfaces of carbon additives or cathode particles, an ideal approach would be to minimize the exposure of SEs to conductive surfaces while maintaining long-range electronic pathways between the electrode material and the current collector.[266] One effective strategy involves selecting carbon materials with low specific surface areas (e.g., carbon nanotubes or vapor-grown carbon fibers) to slow down the decomposition kinetics of SEs.[187]

In composite cathodes for ASSSBs, binders primarily enhance mechanical stability and optimize interfacial contact. They improve adhesion between CAMs, SEs, and conductive additives, preventing particle detachment. Furthermore, the chemical stability of binders determines their tolerance under high-voltage conditions, helping to mitigate side reactions that could compromise interface stability. An appropriate binder not only facilitates electrode fabrication and film formation but also reduces side reactions at the interface, ultimately enhancing the electrochemical performance of the battery.

Given the distinct roles and properties of each component in composite cathodes, their design should adhere to the following principles: 1) CAMs determine energy density and rate capability. Optimization of their particle size and morphology improves interfacial contact and reaction kinetics. 2) SEs provide ionic

c) Schematic diagram illustrating the fabrication of $NaCrO_2$ electrodes infiltrated with the $Na_4(B_{12}H_{12})(B_{10}H_{10})$ SE by solution processing and the cross sectional SEM image of the densified $Na_4(B_{12}H_{12})(B_{10}H_{10})$-infiltrated $NaCrO_2$ electrode is also shown. Reproduced with permission.[260] Copyright 2020, Elsevier. d) Schematic illustration for the preparation of $Na_3B_{24}H_{23}$-based SE and 4 V all-solid-state $Na[Ni_{1/3}Fe_{1/3}Mn_{1/3}]O_2$/SE/Na battery and Linear sweep voltammograms of $Na_3B_{24}H_{23}$ and $Na_2B_{12}H_{12}$ with a scan rate of 10 μV s^{-1} at 60 °C. Reproduced with permission.[262] Copyright 2023, Elsevier. e) Schematic illustration of interface morphology evolution during sodium plating/stripping and long-term cycle life at 2C-rate. Reproduced with permission.[264] Copyright 2023, Nature.

pathways. Their distribution and volume fraction must balance ionic conductivity with overall electrode conductivity; insufficient content hinders ion transport, whereas excessive content can impair electronic conduction. 3) Conductive additives enhance electronic conductivity, but their concentration must be carefully controlled to prevent excessive interference with ion transport pathways and to mitigate electrolyte decomposition. 4) Binders ensure structural stability and interface adhesion. Their compatibility with both SEs and CAMs is crucial to minimizing interfacial impedance and avoiding undesirable reactions.

At the microstructural level, various design strategies can be employed to optimize ion and electron transport pathways, such as uniform distribution structures and core-shell architectures. For instance, constructing 3D ion-electron networks can maximize transport efficiency, reduce polarization effects, and enhance rate performance. Additionally, interfacial engineering strategies-such as coatings or surface modifications—can mitigate interfacial side reactions, further improving battery stability. Overall, the structural design of composite cathodes should comprehensively consider conductivity, interfacial stability, and mechanical integrity to achieve high-performance ASSSBs.

6. Summary and Outlook

6.1. Summary: Challenges and Strategies in ASSSBs

ASSSBs represent a crucial development direction for next-generation energy storage technologies, with their performance primarily constrained by the intrinsic characteristics and interfacial issues of three major electrolyte systems.

1) **Oxide SEs** have been widely applied in ASSSBs due to their excellent air stability, superior chemical and electrochemical stability, high oxidative potential (typically exceeding 4.5 V vs Na^+/Na), and fast ionic transport capability. By employing high-temperature sintering or melting techniques, relatively stable cathode–electrolyte interfaces can be constructed, leading to favorable electrochemical performance. However, the intrinsically high rigidity of oxide electrolytes poses severe interfacial contact challenges for practical applications. When paired with rigid oxide CAMs such as NVP, the high mechanical modulus of both components (generally >100 GPa) makes it difficult to achieve sufficient solid–solid interfacial contact, resulting in significant interfacial impedance. During electrochemical cycling, the intrinsic volume change of the cathode induces continuous stress accumulation at the rigid interface, ultimately leading to interfacial contact failure and capacity fading. Introducing a small amount of ionic liquid at the interface can effectively mitigate interfacial delamination and the resulting discontinuity of ion transport pathways, thereby significantly enhancing electrochemical performance and cycling stability.
2) **Sulfide SEs**, featuring much higher ionic conductivities (e.g., $Na_{2.88}Sb_{0.88}W_{0.12}S_4$, σ_{ion} = 32 mS cm^{-1}) and softer mechanical characteristics (Young's modulus: ≈10–20 GPa) compared with oxide SEs, are expected to enable batteries with superior fast-charging/discharging capability and enhanced mechanical stability at solid–solid interfaces. However, their relatively narrow electrochemical stability window (typically below 3.0 V vs Na^+/Na) remains a major bottleneck for practical applications. When paired with high-voltage oxide CAMs (e.g., $NaCrO_2$, >3.0 V vs Na^+/Na), the SE undergoes oxidative decomposition at the interface, producing electronically insulating products such as S, P_2S_5, and Na_3PO_4. These products accumulate to form barrier layers that hinder Na^+ transport across the interface.[35] Even when employing transition metal sulfide CAMs with lower operating potentials (≤3.0 V vs Na^+/Na), such as TiS_2 and FeS_2, to enhance interfacial affinity and suppress side reactions, the issue of interfacial contact failure still persists, leading to reduced utilization of CAMs. This indicates that further optimization of electrode architecture and interface engineering is still required to improve ion transport pathways and enhance overall electrochemical performance.
3) **Hydride and halide SEs** present unique advantages and challenges among emerging electrolyte systems. Hydride electrolytes (e.g., $Na_2B_{12}H_{12}$), while exhibiting excellent thermal stability and ionic conductivity, are limited by their narrow electrochemical window (<2.5 V vs Na^+/Na) for matching with high-voltage cathodes. Halide electrolytes (e.g., Na_3YCl_6) demonstrate relatively wide electrochemical windows (>3.5 V vs Na^+/Na) and tunable ionic conductivity. Meanwhile, their relatively high mechanical hardness (modulus >20 GPa) necessitates high-temperature processing for solid-solid interface contact, while interfacial space-charge layer effects further increase ion transport resistance.

The complexity and diversity of these interfacial issues indicate that a single solution strategy cannot be universally applied across all electrolyte systems. Future research requires developing precise interface regulation strategies tailored to different system characteristics: for oxide systems, the focus should be on developing flexible interlayers and stress-buffering structures; for sulfide systems, there is an urgent need to construct stable interface protection layers and compositionally graded transition layers; and for hydride and halide systems, efforts should focus on reducing cost and improving air stability. Through multi-level, multi-scale interface engineering innovations, combined with advanced characterization techniques and theoretical modeling, ASSSBs will advance steadily toward high energy density and long cycle life.

6.2. Outlook: Toward Interface-Optimized and Mechanically Stable ASSSBs

During battery operation, nearly all classes of SEs—including oxides, sulfides, halides, and hydride—undergo interfacial redox reactions, forming a CEI. Although the CEI can help mitigate side reactions, its typically low ionic conductivity often impedes Na^+ transport. Furthermore, interfacial engineering faces two core challenges: 1) the increased system complexity due to the introduction of additional interphase layers, and 2) the cost and technical difficulty associated with fabricating homogeneous, defect-free interphases.

In summary, the future development of ASSSBs relies on the synergistic integration of materials innovation, interfacial optimization, and mechanical design. By deepening the

understanding of interfacial processes and implementing coordinated structural strategies—particularly leveraging "all-in-one" material designs to fundamentally eliminate interface issues, combined with advanced interfacial engineering techniques—it is promising to realize high-energy-density, long-life, and safe ASSSBs suitable for next-generation energy storage systems.

1) **Toward Optimized Materials for ASSSBs**. To achieve high-performance ASSSBs, further optimization and development of all battery component materials are essential. For SEs, the goal is to simultaneously realize higher ionic conductivity, enhanced mechanical flexibility, and improved chemical stability. Various structural and compositional strategies can be employed to achieve these properties, including high-entropy design to increase lattice disorder, amorphization to suppress grain boundary resistance to ion migration, and the development of composite electrolyte systems that balance ionic transport with mechanical compliance. For CAMs, it is crucial to enhance capacity while maintaining structural stability, with the ideal goal of achieving a "zero-strain" structure. Structural and compositional optimization, nanostructuring, and elemental gradient engineering can effectively mitigate stress accumulation and accommodate volume changes. Furthermore, the development of bifunctional cathodes capable of conducting both ions and electrons can significantly reduce the fraction of electrochemically inactive components, thereby maximizing the energy density potential of ASSSBs. In addition, technological innovations targeting materials are particularly important, such as the development of "all-in-one" integrated CAMs.
2) **Toward Interfacial Stability ASSSBs**. To construct highly stable interfaces, it is essential to ensure a rational pairing between CAMs and SEs. While pursuing high capacity and superior ionic conductivity, both chemical and mechanical compatibility between the two components must be maintained to prevent interfacial reactions and contact degradation. The introduction of stable interfacial layers with excellent mechanical properties and high ionic conductivity can further enhance interfacial contact and overall electrochemical performance. Computational modeling and high-throughput screening techniques play a vital role in interfacial material design, enabling the prediction of interfacial reactions and guiding the rational selection of compatible materials. In addition, systematic optimization of the composite cathode structure and composition is equally critical. A delicate balance must be achieved among energy density, charge-transfer kinetics, and structural stability of the CAMs. By integrating advanced in situ and ex situ characterization techniques, the intrinsic structure–property–stability correlations can be elucidated, providing theoretical guidance for interfacial optimization. Meanwhile, the development of scalable and uniformly dense composite electrode fabrication processes will lay a solid foundation for realizing high-energy-density and long-term stable ASSSBs.
3) **Toward Practical Applications: Pouch Cell and Full-Cell Architectures for ASSSBs**. For the practical deployment of ASSSBs, the transition from lab-scale symmetric or half-cell configurations to full-cell and pouch-type architectures remains a critical step. Current research has largely focused on optimizing solid electrolytes, electrode materials, and their interfaces under idealized conditions; however, the scale-up introduces additional complexities, including electrode thickness, areal capacity, and mechanical integrity of large-format cells. In particular, achieving uniform pressure distribution and stable electrode/electrolyte contact in pouch cells poses significant challenges, as the rigidity of oxide-based solid electrolytes and the mechanical fragility of sulfide-based ones may lead to interfacial degradation or crack formation during long-term cycling. Furthermore, the development of practical full-cell systems requires carefully matched cathode/anode pairs with compatible electrochemical potentials, minimized side reactions, and stable interphases to ensure both energy density and cycling stability. To date, only a limited number of ASSSB pouch cells have been demonstrated, often operating under relatively low current densities and moderate cycling conditions, highlighting the gap between laboratory feasibility and practical requirements.

Moving forward, integrating scalable electrode fabrication methods, optimizing stack pressure management, and engineering robust interfacial architectures will be essential. Ultimately, advancing ASSSBs toward commercial-level pouch cells and full-cell designs will require a balance between electrochemical performance, mechanical reliability, and cost-effectiveness, offering a promising pathway for next-generation sustainable energy storage systems.

Acknowledgements

This work was supported by Research Start-up Fund of Nanjing Normal University (184080H201B41) and a Research Start-up Fund of Southeast University (RF1028624081). S.P. acknowledges the support from the Helmholtz Association.

Open access funding enabled and organized by Projekt DEAL.

Conflict of Interest

The authors declare no conflict of interest.

Keywords

composite cathodes, fabrication, Na-ion, next generation cathodes, solid state batteries

Received: July 8, 2025
Revised: October 8, 2025
Published online:

[1] H. Kwon, J. Baek, H.-T. Kim, *Energy Storage Mater.* **2023**, *55*, 708.
[2] J. Janek, W. G. Zeier, *Nat. Energy* **2016**, *1*, 16141.
[3] Y. Zhao, K. R. Adair, X. Sun, *Energy Environ. Sci.* **2018**, *11*, 2673.
[4] C. Zhao, L. Liu, X. Qi, Y. Lu, F. Wu, J. Zhao, Y. Yu, Y. Hu, L. Chen, *Adv. Energy Mater.* **2018**, *8*, 1703012.
[5] R. Usiskin, Y. Lu, J. Popovic, M. Law, P. Balaya, Y.-S. Hu, J. Maier, *Nat. Rev. Mater.* **2021**, *6*, 1020.
[6] X.-B. Cheng, C.-Z. Zhao, Y.-X. Yao, H. Liu, Q. Zhang, *Chem* **2019**, *5*, 74.

[7] Y. Tian, T. Shi, W. D. Richards, J. Li, J. C. Kim, S.-H. Bo, G. Ceder, *Energy Environ. Sci.* **2017**, *10*, 1150.
[8] G. Liu, J. Yang, J. Wu, Z. Peng, X. Yao, *Adv. Mater.* **2024**, *36*, 2311475.
[9] Q. Ma, M. Guin, S. Naqash, C.-L. Tsai, F. Tietz, O. Guillon, *Chem. Mater.* **2016**, *28*, 4821.
[10] Z. Zhu, I.-H. Chu, Z. Deng, S. P. Ong, *Chem. Mater.* **2015**, *27*, 8318.
[11] A. Hayashi, K. Noi, A. Sakuda, M. Tatsumisago, *Nat. Commun.* **2012**, *3*, 856.
[12] A. Hayashi, N. Masuzawa, S. Yubuchi, F. Tsuji, C. Hotehama, A. Sakuda, M. Tatsumisago, *Nat. Commun.* **2019**, *10*, 5266.
[13] M. Duchardt, U. Ruschewitz, S. Adams, S. Dehnen, B. Roling, *Angew. Chem., Int. Ed.* **2018**, *57*, 1351.
[14] H. Wan, J. P. Mwizerwa, F. Han, W. Weng, J. Yang, C. Wang, X. Yao, *Nano Energy* **2019**, *66*, 104109.
[15] Y. Yang, S. Yang, X. Xue, X. Zhang, Q. Li, Y. Yao, X. Rui, H. Pan, Y. Yu, *Adv. Mater.* **2024**, *36*, 2308332.
[16] W. Hou, X. Guo, X. Shen, K. Amine, H. Yu, J. Lu, *Nano Energy* **2018**, *52*, 279.
[17] S. Schweidler, M. Botros, F. Strauss, Q. Wang, Y. Ma, L. Velasco, G. Cadilha Marques, A. Sarkar, C. Kübel, H. Hahn, J. Aghassi-Hagmann, T. Brezesinski, B. Breitung, *Nat. Rev. Mater.* **2024**, *9*, 266.
[18] Y. Ma, Y. Ma, Q. Wang, S. Schweidler, M. Botros, T. Fu, H. Hahn, T. Brezesinski, B. Breitung, *Energy Environ. Sci.* **2021**, *14*, 2883.
[19] L.-J. Jhang, D. Wang, A. Silver, X. Li, D. Reed, D. Wang, *Nano Energy* **2023**, *105*, 107995.
[20] Y. Ma, H. Du, S. Zheng, Z. Zhou, H. Zhang, Y. Ma, S. Passerini, Y. Wu, *Energy Storage Mater.* **2025**, *79*, 104295.
[21] Y. Dong, Z. Zhou, Y. Ma, H. Zhang, F. Meng, Y. Wu, Y. Ma, *ACS Energy Lett.* **2024**, *9*, 5096.
[22] Z. Zhou, Y. Ma, T. Brezesinski, B. Breitung, Y. Wu, Y. Ma, *Energy Environ. Sci.* **2025**, *18*, 19.
[23] L. Xu, S. Tang, Y. Cheng, K. Wang, J. Liang, C. Liu, Y.-C. Cao, F. Wei, L. Mai, *Joule* **2018**, *2*, 1991.
[24] K. Takada, N. Ohta, L. Zhang, K. Fukuda, I. Sakaguchi, R. Ma, M. Osada, T. Sasaki, *Solid State Ionics* **2008**, *179*, 1333.
[25] A. Sakuda, A. Hayashi, M. Tatsumisago, *Chem. Mater.* **2010**, *22*, 949.
[26] Z. Zhang, Y. Shao, B. Lotsch, Y.-S. Hu, H. Li, J. Janek, L. F. Nazar, C.-W. Nan, J. Maier, M. Armand, L. Chen, *Energy Environ. Sci.* **2018**, *11*, 1945.
[27] H. Che, S. Chen, Y. Xie, H. Wang, K. Amine, X.-Z. Liao, Z.-F. Ma, *Energy Environ. Sci.* **2017**, *10*, 1075.
[28] Y.-F. Yu Yao, J. T. Kummer, *J. Inorg. Nucl. Chem.* **1967**, *29*, 2453.
[29] Y. Lu, L. Li, Q. Zhang, Z. Niu, J. Chen, *Joule* **2018**, *2*, 1747.
[30] H. Y-P, *Mater. Res. Bull.* **1976**, *11*, 173.
[31] M. Jansen, U. Henseler, *J. Solid State Chem.* **1992**, *99*, 110.
[32] H. Oguchi, M. Matsuo, S. Kuromoto, H. Kuwano, S. Orimo, *J. Appl. Phys.* **2012**, *111*, 036102.
[33] T. J. Udovic, M. Matsuo, A. Unemoto, N. Verdal, V. Stavila, A. V. Skripov, J. J. Rush, H. Takamura, S. Orimo, *Chem. Commun.* **2014**, *50*, 3750.
[34] J. Yang, G. Liu, M. Avdeev, H. Wan, F. Han, L. Shen, Z. Zou, S. Shi, Y.-S. Hu, C. Wang, X. Yao, *ACS Energy Lett.* **2020**, *5*, 2835.
[35] E. A. Wu, S. Banerjee, H. Tang, P. M. Richardson, J.-M. Doux, J. Qi, Z. Zhu, A. Grenier, Y. Li, E. Zhao, G. Deysher, E. Sebti, H. Nguyen, R. Stephens, G. Verbist, K. W. Chapman, R. J. Clément, A. Banerjee, Y. S. Meng, S. P. Ong, *Nat. Commun.* **2021**, *12*, 1256.
[36] X. Lin, S. Zhang, M. Yang, B. Xiao, Y. Zhao, J. Luo, J. Fu, C. Wang, X. Li, W. Li, F. Yang, H. Duan, J. Liang, B. Fu, H. Abdolvand, J. Guo, G. King, X. Sun, *Nat. Mater.* **2025**, *24*, 83.
[37] J. Huang, K. Wu, G. Xu, M. Wu, S. Dou, C. Wu, *Chem. Soc. Rev.* **2023**, *52*, 4933.
[38] H. Si, J. Ma, X. Xia, Q. Wang, S. Geng, L. Fu, *Chem. – Eur. J.* **2025**, *31*, 202403247.
[39] Y. Zheng, Y. Yao, J. Ou, M. Li, D. Luo, H. Dou, Z. Li, K. Amine, A. Yu, Z. Chen, *Chem. Soc. Rev.* **2020**, *49*, 8790.
[40] X. Feng, H. Fang, N. Wu, P. Liu, P. Jena, J. Nanda, D. Mitlin, *Joule* **2022**, *6*, 543.
[41] X. He, Y. Zhu, Y. Mo, *Nat. Commun.* **2017**, *8*, 15893.
[42] T. Famprikis, P. Canepa, J. A. Dawson, M. S. Islam, C. Masquelier, *Nat. Mater.* **2019**, *18*, 1278.
[43] Y. Gao, A. M. Nolan, P. Du, Y. Wu, C. Yang, Q. Chen, Y. Mo, S.-H. Bo, *Chem. Rev.* **2020**, *120*, 5954.
[44] Z. Deng, T. P. Mishra, E. Mahayoni, Q. Ma, A. J. K. Tieu, O. Guillon, J.-N. Chotard, V. Seznec, A. K. Cheetham, C. Masquelier, G. S. Gautam, P. Canepa, *Nat. Commun.* **2022**, *13*, 4470.
[45] J. B. Goodenough, Y. Kim, *Chem. Mater.* **2010**, *22*, 587.
[46] Q. Zhou, J. Ma, S. Dong, X. Li, G. Cui, *Adv. Mater.* **2019**, *31*, 1902029.
[47] X. Chi, Y. Liang, F. Hao, Y. Zhang, J. Whiteley, H. Dong, P. Hu, S. Lee, Y. Yao, *Angew. Chem., Int. Ed.* **2018**, *57*, 2630.
[48] S. Wang, Q. Bai, A. M. Nolan, Y. Liu, S. Gong, Q. Sun, Y. Mo, *Angew. Chem., Int. Ed.* **2019**, *58*, 8039.
[49] Z. Xu, X. Chen, K. Liu, R. Chen, X. Zeng, H. Zhu, *Chem. Mater.* **2019**, *31*, 7425.
[50] V. Lacivita, Y. Wang, S.-H. Bo, G. Ceder, *J. Mater. Chem. A* **2019**, *7*, 8144.
[51] W. D. Richards, L. J. Miara, Y. Wang, J. C. Kim, G. Ceder, *Chem. Mater.* **2016**, *28*, 266.
[52] S. Ferrer-Nicomedes, A. Mormeneo-Segarra, N. Vicente-Agut, A. Barba-Juan, *J. Mater. Chem. A* **2025**, *13*, 12439.
[53] T. Wei, Y. Gong, X. Zhao, K. Huang, *Adv. Funct. Mater.* **2014**, *24*, 5380.
[54] K. B. Hueso, M. Armand, T. Rojo, *Energy Environ. Sci.* **2013**, *6*, 734.
[55] S. C. Ligon, M.-C. Bay, M. V. F. Heinz, C. Battaglia, T. Graule, G. Blugan, *Materials* **2020**, *13*, 433.
[56] X. Lu, G. Xia, J. P. Lemmon, Z. Yang, *J. Power Sources* **2010**, *195*, 2431.
[57] Z. Yang, J. Zhang, M. C. W. Kintner-Meyer, X. Lu, D. Choi, J. P. Lemmon, J. Liu, *Chem. Rev.* **2011**, *111*, 3577.
[58] K. Li, Y. Yang, X. Zhang, S. Liang, *J. Mater. Sci.* **2020**, *55*, 8435.
[59] C. Zhu, J. Xue, *J. Alloys Compd.* **2012**, *517*, 182.
[60] T. J. Whalen, G. J. Tennenhouse, C. Meyer, *J. Am. Ceram. Soc.* **1974**, *57*, 497.
[61] H. Park, K. Jung, M. Nezafati, C.-S. Kim, B. Kang, *ACS Appl. Mater. Interfaces* **2016**, *8*, 27814.
[62] J. B. Goodenough, H. Y.-P. Hong, J. A. Kafalas, *Mater. Res. Bull.* **1976**, *11*, 203.
[63] S. Liu, C. Zhou, Y. Wang, W. Wang, Y. Pei, J. Kieffer, R. M. Laine, *ACS Appl. Mater. Interfaces* **2020**, *12*, 3502.
[64] Y. Lu, J. A. Alonso, Q. Yi, L. Lu, Z. L. Wang, C. Sun, *Adv. Energy Mater.* **2019**, *9*, 1901205.
[65] Q. Ma, C.-L. Tsai, X.-K. Wei, M. Heggen, F. Tietz, J. T. S. Irvine, *J. Mater. Chem. A* **2019**, *7*, 7766.
[66] T. Krauskopf, S. P. Culver, W. G. Zeier, *Inorg. Chem.* **2018**, *57*, 4739.
[67] N. Wang, K. Yang, L. Zhang, X. Yan, L. Wang, B. Xu, *J. Mater. Sci.* **2018**, *53*, 1987.
[68] C. Wang, J. Liang, J. T. Kim, X. Sun, *Sci. Adv.* **2022**, *8*, adc9516.
[69] H. Kwak, J. Lyoo, J. Park, Y. Han, R. Asakura, A. Remhof, C. Battaglia, H. Kim, S.-T. Hong, Y. S. Jung, *Energy Storage Mater.* **2021**, *37*, 47.
[70] D. Park, K. Kim, G. H. Chun, B. C. Wood, J. H. Shim, S. Yu, *J. Mater. Chem. A* **2021**, *9*, 23037.
[71] Y. Qie, S. Wang, S. Fu, H. Xie, Q. Sun, P. Jena, *J. Phys. Chem. Lett.* **2020**, *11*, 3376.
[72] J. Liang, X. Li, K. R. Adair, X. Sun, *Acc. Chem. Res.* **2021**, *54*, 1023.
[73] S. Yu, K. Kim, B. C. Wood, H.-G. Jung, K. Y. Chung, *J. Mater. Chem. A* **2022**, *10*, 24301.
[74] H. Kwak, S. Wang, J. Park, Y. Liu, K. T. Kim, Y. Choi, Y. Mo, Y. S. Jung, *ACS Energy Lett.* **2022**, *7*, 1776.

[75] R. Schlem, A. Banik, M. Eckardt, M. Zobel, W. G. Zeier, *ACS Appl. Energy Mater.* **2020**, *3*, 10164.
[76] A. Inoishi, A. Nojima, M. Tanaka, M. Suyama, S. Okada, H. Sakaebe, *Chem. – Eur. J.* **2023**, *29*, 202301586.
[77] J. L. Souquet, *Annu. Rev. Mater. Sci.* **1981**, *11*, 211.
[78] X. Chi, Y. Zhang, F. Hao, S. Kmiec, H. Dong, R. Xu, K. Zhao, Q. Ai, T. Terlier, L. Wang, L. Zhao, L. Guo, J. Lou, H. L. Xin, S. W. Martin, Y. Yao, *Nat. Commun.* **2022**, *13*, 2854.
[79] R. Mohtadi, S. Orimo, *Nat. Rev. Mater.* **2016**, *2*, 16091.
[80] Z. Lu, F. Ciucci, *Chem. Mater.* **2017**, *29*, 9308.
[81] L. Duchêne, A. Remhof, H. Hagemann, C. Battaglia, *Energy Storage Mater.* **2020**, *25*, 782.
[82] W. S. Tang, M. Matsuo, H. Wu, V. Stavila, W. Zhou, A. A. Talin, A. V. Soloninin, R. V. Skoryunov, O. A. Babanova, A. V. Skripov, A. Unemoto, S. Orimo, T. J. Udovic, *Adv. Energy Mater.* **2016**, *6*, 1502237.
[83] W. S. Tang, A. Unemoto, W. Zhou, V. Stavila, M. Matsuo, H. Wu, S. Orimo, T. J. Udovic, *Energy Environ. Sci.* **2015**, *8*, 3637.
[84] T. J. Udovic, M. Matsuo, W. S. Tang, H. Wu, V. Stavila, A. V. Soloninin, R. V. Skoryunov, O. A. Babanova, A. V. Skripov, J. J. Rush, A. Unemoto, H. Takamura, S. Orimo, *Adv. Mater.* **2014**, *26*, 7622.
[85] J. Cuan, Y. Zhou, T. Zhou, S. Ling, K. Rui, Z. Guo, H. Liu, X. Yu, *Adv. Mater.* **2019**, *31*, 1803533.
[86] J. Wu, R. Zhang, Q. Fu, J. Zhang, X. Zhou, P. Gao, C. Xu, J. Liu, X. Guo, *Adv. Funct. Mater.* **2021**, *31*, 2008165.
[87] S. Kim, H. Oguchi, N. Toyama, T. Sato, S. Takagi, T. Otomo, D. Arunkumar, N. Kuwata, J. Kawamura, S. Orimo, *Nat. Commun.* **2019**, *10*, 1081.
[88] Y. Sadikin, M. Brighi, P. Schouwink, R. Černý, *Adv. Energy Mater.* **2015**, *5*, 1501016.
[89] N. T. Hahn, T. J. Seguin, K.-C. Lau, C. Liao, B. J. Ingram, K. A. Persson, K. R. Zavadil, *J. Am. Chem. Soc.* **2018**, *140*, 11076.
[90] J. B. Varley, K. Kweon, P. Mehta, P. Shea, T. W. Heo, T. J. Udovic, V. Stavila, B. C. Wood, *ACS Energy Lett.* **2017**, *2*, 250.
[91] W. S. Tang, K. Yoshida, A. V. Soloninin, R. V. Skoryunov, O. A. Babanova, A. V. Skripov, M. Dimitrievska, V. Stavila, S. Orimo, T. J. Udovic, *ACS Energy Lett.* **2016**, *1*, 659.
[92] W. S. Tang, M. Matsuo, H. Wu, V. Stavila, A. Unemoto, S. Orimo, T. J. Udovic, *Energy Storage Mater.* **2016**, *4*, 79.
[93] R. Jalem, B. Gao, H.-K. Tian, Y. Tateyama, *J. Mater. Chem. A* **2022**, *10*, 2235.
[94] G. Deysher, Y.-T. Chen, B. Sayahpour, S. W.-H. Lin, S.-Y. Ham, P. Ridley, A. Cronk, E. A. Wu, D. H. S. Tan, J.-M. Doux, J. A. S. Oh, J. Jang, L. H. B. Nguyen, Y. S. Meng, *ACS Appl. Mater. Interfaces* **2022**, *14*, 47706.
[95] S. Wang, X. Xu, C. Cui, C. Zeng, J. Liang, J. Fu, R. Zhang, T. Zhai, H. Li, *Adv. Funct. Mater.* **2022**, *32*, 2108805.
[96] J. Hou, T. Zhu, G. Wang, R. Cheacharoen, W. Sun, X. Lei, Q. Yuan, D. Sun, J. Zhao, *Carbon Energy* **2024**, *6*, 628.
[97] M. Jin, D. Xu, Z. Su, R. Liu, M. Xiang, Y. Cheng, R. Wu, Y. Guo, *Adv. Mater.* **2025**, 07809.
[98] L. Liu, X. Qi, Q. Ma, X. Rong, Y.-S. Hu, Z. Zhou, H. Li, X. Huang, L. Chen, *ACS Appl. Mater. Interfaces* **2016**, *8*, 32631.
[99] L. Duchêne, R.-S. Kühnel, E. Stilp, E. Cuervo Reyes, A. Remhof, H. Hagemann, C. Battaglia, *Energy Environ. Sci.* **2017**, *10*, 2609.
[100] H. Hou, Q. Xu, Y. Pang, L. Li, J. Wang, C. Zhang, C. Sun, *Adv. Sci.* **2017**, *4*, 1700072.
[101] P. Kehne, C. Guhl, Q. Ma, F. Tietz, L. Alff, R. Hausbrand, P. Komissinskiy, *J. Power Sources* **2019**, *409*, 86.
[102] Z. Zhang, Q. Zhang, J. Shi, Y. S. Chu, X. Yu, K. Xu, M. Ge, H. Yan, W. Li, L. Gu, Y. Hu, H. Li, X. Yang, L. Chen, X. Huang, *Adv. Energy Mater.* **2017**, *7*, 1601196.
[103] K. Zhao, Y. Liu, S. Zhang, S. He, N. Zhang, J. Yang, Z. Zhan, *Electrochem. Commun.* **2016**, *69*, 59.
[104] J. Li, G. Du, T. Huang, F. Zhang, M. Xie, Y. Qi, S.-J. Bao, M. Xu, *Energy Technol.* **2020**, *8*, 2000494.
[105] R. P. Rao, H. Chen, L. L. Wong, S. Adams, *J. Mater. Chem. A* **2017**, *5*, 3377.
[106] J.-K. Kim, Y. J. Lim, H. Kim, G.-B. Cho, Y. Kim, *Energy Environ. Sci.* **2015**, *8*, 3589.
[107] R. Asakura, D. Reber, L. Duchêne, S. Payandeh, A. Remhof, H. Hagemann, C. Battaglia, *Energy Environ. Sci.* **2020**, *13*, 5048.
[108] G. Du, M. Tao, J. Li, T. Yang, W. Gao, J. Deng, Y. Qi, S. Bao, M. Xu, *Adv. Energy Mater.* **2020**, *10*, 1903351.
[109] H. Gao, S. Xin, L. Xue, J. B. Goodenough, *Chem* **2018**, *4*, 833.
[110] S. Fan, M. Lei, H. Wu, J. Hu, C. Yin, T. Liang, C. Li, *Energy Storage Mater.* **2020**, *31*, 87.
[111] J. Yue, F. Han, X. Fan, X. Zhu, Z. Ma, J. Yang, C. Wang, *ACS Nano* **2017**, *11*, 4885.
[112] G. Xiong, M. Wu, X. Wu, Z. Wen, *Chem. Eng. J.* **2024**, *497*, 154444.
[113] Q. Yu, J. Hu, X. Nie, Y. Zeng, C. Li, *ACS Nano* **2024**, *18*, 5790.
[114] Q. Yu, Y. Xu, J. Hu, Y. Sun, Y. Zeng, X. Nie, Y. Zhao, C. Li, *Energy Storage Mater.* **2024**, *73*, 103795.
[115] Q. Yu, J. Hu, Y. Xu, R. Cao, S. Chen, C. Li, *Angew. Chem., Int. Ed.* **2025**, *64*, 202425503.
[116] F. Hao, X. Chi, Y. Liang, Y. Zhang, R. Xu, H. Guo, T. Terlier, H. Dong, K. Zhao, J. Lou, Y. Yao, *Joule* **2019**, *3*, 1349.
[117] Z. Song, Y. Qian, T. Zhang, M. Otani, H. Zhou, *Adv. Sci.* **2015**, *2*, 1500124.
[118] M. S. Chae, H. J. Kim, H. Bu, J. Lyoo, R. Attias, B. Dlugatch, M. Oliel, Y. Gofer, S. Hong, D. Aurbach, *Adv. Energy Mater.* **2020**, *10*, 2000564.
[119] J. Billaud, R. J. Clément, A. R. Armstrong, J. Canales-Vázquez, P. Rozier, C. P. Grey, P. G. Bruce, *J. Am. Chem. Soc.* **2014**, *136*, 17243.
[120] H. Pan, X. Lu, X. Yu, Y. Hu, H. Li, X. Yang, L. Chen, *Adv. Energy Mater.* **2013**, *3*, 1186.
[121] Y. Liu, Y. Qiao, W. Zhang, Z. Li, X. Ji, L. Miao, L. Yuan, X. Hu, Y. Huang, *Nano Energy* **2015**, *12*, 386.
[122] X. Liu, S. Li, Y. Zhu, X. Zhang, Y. Su, M. Li, H. Li, B. Chen, Y. Liu, Y. Xiao, *Adv. Funct. Mater.* **2025**, *35*, 2414130.
[123] H. Pan, Y.-S. Hu, L. Chen, *Energy Environ. Sci.* **2013**, *6*, 2338.
[124] N. A. Katcho, J. Carrasco, D. Saurel, E. Gonzalo, M. Han, F. Aguesse, T. Rojo, *Adv. Energy Mater.* **2017**, *7*, 1601477.
[125] L. Liu, X. Li, S. Bo, Y. Wang, H. Chen, N. Twu, D. Wu, G. Ceder, *Adv. Energy Mater.* **2015**, *5*, 1500944.
[126] P. Wang, M. Weng, Y. Xiao, Z. Hu, Q. Li, M. Li, Y. Wang, X. Chen, X. Yang, Y. Wen, Y. Yin, X. Yu, Y. Xiao, J. Zheng, L. Wan, F. Pan, Y. Guo, *Adv. Mater.* **2019**, *31*, 1903483.
[127] Q. Ni, Y. Bai, F. Wu, C. Wu, *Adv. Sci.* **2017**, *4*, 1600275.
[128] Y. Fang, L. Xiao, X. Ai, Y. Cao, H. Yang, *Adv. Mater.* **2015**, *27*, 5895.
[129] Z. Jing, L. Kong, M. Mamoor, L. Wang, B. Zhang, B. Wang, Y. Zhai, F. Wang, G. Qu, Y. Kong, D. Wang, L. Xu, *J. Am. Chem. Soc.* **2025**, *147*, 3702.
[130] Z. Zhou, Y. Dong, Y. Ma, H. Zhang, F. Meng, Y. Ma, Y. Wu, *SusMat* **2025**, *5*, 265.
[131] L. Wang, J. Song, R. Qiao, L. A. Wray, M. A. Hossain, Y.-D. Chuang, W. Yang, Y. Lu, D. Evans, J.-J. Lee, S. Vail, X. Zhao, M. Nishijima, S. Kakimoto, J. B. Goodenough, *J. Am. Chem. Soc.* **2015**, *137*, 2548.
[132] H.-W. Lee, R. Y. Wang, M. Pasta, S. W Lee, N. Liu, Y. Cui, *Nat. Commun.* **2014**, *5*, 5280.
[133] H. Zhang, Y. Gao, J. Peng, Y. Fan, L. Zhao, L. Li, Y. Xiao, W. K. Pang, J. Wang, S. Chou, *Angew. Chem., Int. Ed.* **2023**, *62*, 202303953.
[134] Y. Ma, Y. Ma, S. L. Dreyer, Q. Wang, K. Wang, D. Goonetilleke, A. Omar, D. Mikhailova, H. Hahn, B. Breitung, T. Brezesinski, *Adv. Mater.* **2021**, *33*, 2101342.
[135] Y. You, H. Yao, S. Xin, Y. Yin, T. Zuo, C. Yang, Y. Guo, Y. Cui, L. Wan, J. B. Goodenough, *Adv. Mater.* **2016**, *28*, 7243.
[136] Y. Jiang, S. Yu, B. Wang, Y. Li, W. Sun, Y. Lu, M. Yan, B. Song, S. Dou, *Adv. Funct. Mater.* **2016**, *26*, 5315.

[137] Y. Ma, Y. Hu, Y. Pramudya, T. Diemant, Q. Wang, D. Goonetilleke, Y. Tang, B. Zhou, H. Hahn, W. Wenzel, M. Fichtner, Y. Ma, B. Breitung, T. Brezesinski, *Adv. Funct. Mater.* **2022**, *32*, 2202372.
[138] Y. He, S. L. Dreyer, T. Akçay, T. Diemant, R. Mönig, Y. Ma, Y. Tang, H. Wang, J. Lin, S. Schweidler, M. Fichtner, H. Hahn, T. Brezesinski, B. Breitung, Y. Ma, *ACS Nano* **2024**, *18*, 24441.
[139] Y. He, S. L. Dreyer, Y. Ting, Y. Ma, Y. Hu, D. Goonetilleke, Y. Tang, T. Diemant, B. Zhou, P. M. Kowalski, M. Fichtner, H. Hahn, J. Aghassi-Hagmann, T. Brezesinski, B. Breitung, Y. Ma, *Angew. Chem., Int. Ed.* **2024**, *63*, 202315371.
[140] J. Peng, W. Zhang, Q. Liu, J. Wang, S. Chou, H. Liu, S. Dou, *Adv. Mater.* **2022**, *34*, 2108384.
[141] Y. Lu, L. Wang, J. Cheng, J. B. Goodenough, *Chem. Commun.* **2012**, *48*, 6544.
[142] Y. Xiao, S. H. Lee, Y. Sun, *Adv. Energy Mater.* **2017**, *7*, 1601329.
[143] Z. Pan, Y. Yan, N. Cui, J. Xie, Y. Zhang, W. Mu, C. Hao, *Adv. Mater. Interfaces* **2018**, *5*, 1701481.
[144] Y. Liao, K.-S. Park, P. Xiao, G. Henkelman, W. Li, J. B. Goodenough, *Chem. Mater.* **2013**, *25*, 1699.
[145] X. Ou, X. Xiong, F. Zheng, C. Yang, Z. Lin, R. Hu, C. Jin, Y. Chen, M. Liu, *J. Power Sources* **2016**, *325*, 410.
[146] F. Xie, L. Zhang, Q. Gu, D. Chao, M. Jaroniec, S.-Z. Qiao, *Nano Energy* **2019**, *60*, 591.
[147] Y. V. Lim, X. L. Li, H. Y. Yang, *Adv. Funct. Mater.* **2021**, *31*, 2006761.
[148] D. Y. W. Yu, P. V. Prikhodchenko, C. W. Mason, S. K. Batabyal, J. Gun, S. Sladkevich, A. G. Medvedev, O. Lev, *Nat. Commun.* **2013**, *4*, 2922.
[149] Z. Hu, Q. Liu, S. Chou, S. Dou, *Adv. Mater.* **2017**, *29*, 1700606.
[150] H. Arai, S. Okada, Y. Sakurai, J. Yamaki, *J. Power Sources* **1997**, *68*, 716.
[151] M. Nishijima, I. D. Gocheva, S. Okada, T. Doi, J. Yamaki, T. Nishida, *J. Power Sources* **2009**, *190*, 558.
[152] F. Wang, R. Robert, N. A. Chernova, N. Pereira, F. Omenya, F. Badway, X. Hua, M. Ruotolo, R. Zhang, L. Wu, V. Volkov, D. Su, B. Key, M. S. Whittingham, C. P. Grey, G. G. Amatucci, Y. Zhu, J. Graetz, *J. Am. Chem. Soc.* **2011**, *133*, 18828.
[153] J. Kohl, D. Wiedemann, S. Nakhal, P. Bottke, N. Ferro, T. Bredow, E. Kemnitz, M. Wilkening, P. Heitjans, M. Lerch, *J. Mater. Chem.* **2012**, *22*, 15819.
[154] G. Lieser, V. Winkler, H. Geßwein, L. De Biasi, S. Glatthaar, M. J. Hoffmann, H. Ehrenberg, J. R. Binder, *J. Power Sources* **2015**, *294*, 444.
[155] D. Peng, R. Li, K. Xu, R. Si, Z. Zhang, Y.-S. Hu, *ACS Energy Lett.* **2025**, *10*, 1421.
[156] B. Kim, G. Jeong, A. Kim, Y. Kim, M. G. Kim, H. Kim, Y. Kim, *Adv. Energy Mater.* **2016**, *6*, 1600862.
[157] X. Zhan, J. P. Sepulveda, X. Lu, J. F. Bonnett, N. L. Canfield, T. Lemmon, K. Jung, D. M. Reed, V. L. Sprenkle, G. Li, *Energy Storage Mater.* **2020**, *24*, 177.
[158] G. Li, X. Lu, J. Y. Kim, V. V. Viswanathan, K. D. Meinhardt, M. H. Engelhard, V. L. Sprenkle, *Adv. Energy Mater.* **2015**, *5*, 1500357.
[159] X. Lu, G. Li, J. Y. Kim, J. P. Lemmon, V. L. Sprenkle, Z. Yang, *Energy Environ. Sci.* **2013**, *6*, 1837.
[160] D. Li, W. Tang, C. Y. Yong, Z. H. Tan, C. Wang, C. Fan, *ChemSusChem* **2020**, *13*, 1991.
[161] Z. Song, H. Zhou, *Energy Environ. Sci.* **2013**, *6*, 2280.
[162] X. Xiang, K. Zhang, J. Chen, *Adv. Mater.* **2015**, *27*, 5343.
[163] G. Milczarek, O. Inganäs, *Science* **2012**, *335*, 1468.
[164] J. Tarascon, *ChemSusChem* **2008**, *1*, 777.
[165] Q. Zhao, Y. Lu, J. Chen, *Adv. Energy Mater.* **2017**, *7*, 1601792.
[166] L. Zhu, Y. Shen, M. Sun, J. Qian, Y. Cao, X. Ai, H. Yang, *Chem. Commun.* **2013**, *49*, 11370.
[167] C. Fu, Y. Li, W. Xu, X. Feng, W. Gu, J. Liu, W. Deng, W. Wang, A. M. M. Abeykoon, L. Su, L. Zhu, X. Wu, H. Xiang, *Nat. Commun.* **2024**, *15*, 4315.
[168] L. Li, J. Yao, R. Xu, Q. Lin, X. Yan, C. Yu, L. Zhang, *Energy Storage Mater.* **2023**, *63*, 103016.
[169] P. W. Jaschin, C. R. Tang, E. D. Wachsman, *Energy Environ. Sci.* **2024**, *17*, 727.
[170] X. Wang, J. Chen, D. Wang, Z. Mao, *Nat. Commun.* **2021**, *12*, 7109.
[171] B. Liang, Y. Lv, H. Wang, B. Li, S. Zhao, L. Zheng, Y. Huang, Z. Hong, *Energy Storage Mater.* **2024**, *73*, 103804.
[172] S. Kmiec, P. Vanaphuti, A. Manthiram, *J. Mater. Chem. A* **2024**, *12*, 3006.
[173] Y. Wang, X. Zhao, J. Jin, Q. Shen, Y. Hu, X. Song, H. Li, X. Qu, L. Jiao, Y. Liu, *J. Am. Chem. Soc.* **2023**, *145*, 22708.
[174] A. Grimaud, W. T. Hong, Y. Shao-Horn, J.-M. Tarascon, *Nat. Mater.* **2016**, *15*, 121.
[175] H. Ren, Y. Li, Q. Ni, Y. Bai, H. Zhao, C. Wu, *Adv. Mater.* **2022**, *34*, 2106171.
[176] X. Zhang, Y. Qiao, S. Guo, K. Jiang, S. Xu, H. Xu, P. Wang, P. He, H. Zhou, *Adv. Mater.* **2019**, *31*, 1807770.
[177] Q. Wu, S. Xiong, F. Li, A. Matic, *Batteries Supercaps* **2023**, *6*, 202300321.
[178] R. Koerver, W. Zhang, L. De Biasi, S. Schweidler, A. O. Kondrakov, S. Kolling, T. Brezesinski, P. Hartmann, W. G. Zeier, J. Janek, *Energy Environ. Sci.* **2018**, *11*, 2142.
[179] L. Wang, T. Liu, T. Wu, J. Lu, *Nature* **2022**, *611*, 61.
[180] C. Xu, K. Märker, J. Lee, A. Mahadevegowda, P. J. Reeves, S. J. Day, M. F. Groh, S. P. Emge, C. Ducati, B. Layla Mehdi, C. C. Tang, C. P. Grey, *Nat. Mater.* **2021**, *20*, 84.
[181] Y. Zou, Y. Tang, Q. Zheng, H. Zhang, Y. Yan, J. Xue, S. Zhou, J. Xu, W. Yin, H. Liao, Y. Qiao, J. Bao, S. Sun, *Adv. Funct. Mater.* **2024**, *34*, 2406068.
[182] J. Billaud, G. Singh, A. R. Armstrong, E. Gonzalo, V. Roddatis, M. Armand, T. Rojo, P. G. Bruce, *Energy Environ. Sci.* **2014**, *7*, 1387.
[183] T. Zhang, M. Ren, Y. Huang, F. Li, W. Hua, S. Indris, F. Li, *Angew. Chem., Int. Ed.* **2024**, *63*, 202316949.
[184] F. Strauss, T. Bartsch, L. De Biasi, A.-Y. Kim, J. Janek, P. Hartmann, T. Brezesinski, *ACS Energy Lett.* **2018**, *3*, 992.
[185] S. Wenzel, T. Leichtweiss, D. Krüger, J. Sann, J. Janek, *Solid State Ionics* **2015**, *278*, 98.
[186] R. Koerver, F. Walther, I. Aygün, J. Sann, C. Dietrich, W. G. Zeier, J. Janek, *J. Mater. Chem. A* **2017**, *5*, 22750.
[187] W. Zhang, T. Leichtweiß, S. P. Culver, R. Koerver, D. Das, D. A. Weber, W. G. Zeier, J. Janek, *ACS Appl. Mater. Interfaces* **2017**, *9*, 35888.
[188] K. Yoon, J.-J. Kim, W. M. Seong, M. H. Lee, K. Kang, *Sci. Rep.* **2018**, *8*, 8066.
[189] G. Oh, M. Hirayama, O. Kwon, K. Suzuki, R. Kanno, *Chem. Mater.* **2016**, *28*, 2634.
[190] T. Shi, Q. Tu, Y. Tian, Y. Xiao, L. J. Miara, O. Kononova, G. Ceder, *Adv. Energy Mater.* **2020**, *10*, 1902881.
[191] M. B. Dixit, A. Parejiya, N. Muralidharan, R. Essehli, R. Amin, I. Belharouak, *Energy Storage Mater.* **2021**, *40*, 239.
[192] Y. Liu, X. An, K. Yang, J. Ma, J. Mi, D. Zhang, X. Cheng, Y. Li, Y. Ma, M. Liu, F. Kang, Y.-B. He, *Energy Environ. Sci.* **2024**, *17*, 344.
[193] S. Farzanian, J. Vazquez Mercado, I. Shozib, N. Sivadas, V. Lacivita, Y. Wang, Q. H. Tu, *ACS Appl. Energy Mater.* **2023**, *6*, 9615.
[194] P. Minnmann, F. Strauss, A. Bielefeld, R. Ruess, P. Adelhelm, S. Burkhardt, S. L. Dreyer, E. Trevisanello, H. Ehrenberg, T. Brezesinski, F. H. Richter, J. Janek, *Adv. Energy Mater.* **2022**, *12*, 2201425.
[195] W. Xie, Z. Deng, Z. Liu, T. Famprikis, K. T. Butler, P. Canepa, *Adv. Energy Mater.* **2024**, *14*, 2304230.
[196] Y. Ma, R. Zhang, Y. Ma, T. Diemant, Y. Tang, S. Payandeh, D. Goonetilleke, D. Kitsche, X. Liu, J. Lin, A. Kondrakov, T. Brezesinski, *Chem. Mater.* **2024**, *36*, 2588.
[197] J. Jamnik, J. Maier, *Phys. Chem. Chem. Phys.* **2001**, *3*, 1668.
[198] Y. Wang, G. Li, K. Shen, E. Tian, *Mater. Res. Express* **2021**, *8*, 025508.

[199] M. Samiee, B. Radhakrishnan, Z. Rice, Z. Deng, Y. S. Meng, S. P. Ong, J. Luo, *J. Power Sources* **2017**, *347*, 229.
[200] A. Lindner, S. Both, W. Menesklou, S. Hein, T. Danner, A. Latz, U. Krewer, *Batter. Supercaps* **2024**, *7*, 202400503.
[201] S. A. Han, J. H. Suh, M.-S. Park, J. H. Kim, *Electrochem. Energy Rev.* **2025**, *8*, 5.
[202] M. Alabdali, F. M. Zanotto, V. Viallet, V. Seznec, A. A. Franco, *Curr. Opin. Electrochem.* **2022**, *36*, 101127.
[203] S. Choi, M. Jeon, J. Ahn, W. D. Jung, S. M. Choi, J.-S. Kim, J. Lim, Y.-J. Jang, H.-G. Jung, J.-H. Lee, B.-I. Sang, H. Kim, *ACS Appl. Mater. Interfaces* **2018**, *10*, 23740.
[204] G. Bucci, B. Talamini, A. Renuka Balakrishna, Y.-M. Chiang, W. C. Carter, *Phys. Rev. Mater.* **2018**, *2*, 105407.
[205] H. Gao, L. Xue, S. Xin, K. Park, J. B. Goodenough, *Angew. Chem., Int. Ed.* **2017**, *56*, 5541.
[206] Y. Noguchi, E. Kobayashi, L. S. Plashnitsa, S. Okada, J. Yamaki, *Electrochim. Acta* **2013**, *101*, 59.
[207] F. Lalère, J. B. Leriche, M. Courty, S. Boulineau, V. Viallet, C. Masquelier, V. Seznec, *J. Power Sources* **2014**, *247*, 975.
[208] V. S. Kandagal, M. D. Bharadwaj, U. V. Waghmare, *J. Mater. Chem. A* **2015**, *3*, 12992.
[209] H. Tang, Z. Deng, Z. Lin, Z. Wang, I.-H. Chu, C. Chen, Z. Zhu, C. Zheng, S. P. Ong, *Chem. Mater.* **2018**, *30*, 163.
[210] A. Hayashi, K. Noi, N. Tanibata, M. Nagao, M. Tatsumisago, *J. Power Sources* **2014**, *258*, 420.
[211] N. Ohta, K. Takada, I. Sakaguchi, L. Zhang, R. Ma, K. Fukuda, M. Osada, T. Sasaki, *Electrochem. Commun.* **2007**, *9*, 1486.
[212] Z. Yu, S. Shang, J. Seo, D. Wang, X. Luo, Q. Huang, S. Chen, J. Lu, X. Li, Z. Liu, D. Wang, *Adv. Mater.* **2017**, *29*, 1605561.
[213] Y. Li, S. Halacoglu, V. Shreyas, W. Arnold, X. Guo, Q. Dou, J. B. Jasinski, B. Narayanan, H. Wang, *Chem. Eng. J.* **2022**, *434*, 134679.
[214] Y. Li, W. Arnold, S. Halacoglu, J. B. Jasinski, T. Druffel, H. Wang, *Adv. Funct. Mater.* **2021**, *31*, 2101636.
[215] A. L. Santhosha, P. K. Nayak, K. Pollok, F. Langenhorst, P. Adelhelm, *J. Phys. Chem. C* **2019**, *123*, 12126.
[216] K. Yamamoto, Y. Iriyama, T. Asaka, T. Hirayama, H. Fujita, C. A. J. Fisher, K. Nonaka, Y. Sugita, Z. Ogumi, *Angew. Chem., Int. Ed.* **2010**, *49*, 4414.
[217] K. Takahashi, K. Hattori, T. Yamazaki, K. Takada, M. Matsuo, S. Orimo, H. Maekawa, H. Takamura, *J. Power Sources* **2013**, *226*, 61.
[218] Y. Gong, C. Zhao, D. Wang, X. Wang, Z. Wang, Y. Wu, Y. Xia, Q. Jing, Y. Ji, Y. Jiang, J. Liang, X. Li, T. Jiang, X. Sun, X. Zhai, H. Sun, X. Sun, *Energy Storage Mater.* **2025**, *74*, 103980.
[219] I. Kochetkov, T.-T. Zuo, R. Ruess, B. Singh, L. Zhou, K. Kaup, J. Janek, L. Nazar, *Energy Environ. Sci.* **2022**, *15*, 3933.
[220] L. Zhou, T. Zuo, C. Li, Q. Zhang, J. Janek, L. F. Nazar, *ACS Energy Lett.* **2023**, *8*, 3102.
[221] S.-K. Park, J. Lee, S. Bong, B. Jang, K. Seong, Y. Piao, *ACS Appl. Mater. Interfaces* **2016**, *8*, 19456.
[222] D. Chao, C. Zhu, P. Yang, X. Xia, J. Liu, J. Wang, X. Fan, S. V. Savilov, J. Lin, H. J. Fan, Z. X. Shen, *Nat. Commun.* **2016**, *7*, 12122.
[223] H. Wan, J. P. Mwizerwa, X. Qi, X. Liu, X. Xu, H. Li, Y.-S. Hu, X. Yao, *ACS Nano* **2018**, *12*, 2809.
[224] J. Yue, X. Zhu, F. Han, X. Fan, L. Wang, J. Yang, C. Wang, *ACS Appl. Mater. Interfaces* **2018**, *10*, 39645.
[225] X. Fan, J. Yue, F. Han, J. Chen, T. Deng, X. Zhou, S. Hou, C. Wang, *ACS Nano* **2018**, *12*, 3360.
[226] C. Guhl, P. Kehne, Q. Ma, F. Tietz, P. Komissinskiy, W. Jaegermann, R. Hausbrand, *Electrochim. Acta* **2018**, *268*, 226.
[227] H. Kawasoko, S. Shiraki, T. Suzuki, R. Shimizu, T. Hitosugi, *ACS Appl. Mater. Interfaces* **2018**, *10*, 27498.
[228] J. Li, C. Ma, M. Chi, C. Liang, N. J. Dudney, *Adv. Energy Mater.* **2015**, *5*, 1401408.
[229] S. Moitzheim, B. Put, P. M. Vereecken, *Adv. Mater. Interfaces* **2019**, *6*, 1900805.
[230] T. Lan, C.-L. Tsai, F. Tietz, X.-K. Wei, M. Heggen, R. E. Dunin-Borkowski, R. Wang, Y. Xiao, Q. Ma, O. Guillon, *Nano Energy* **2019**, *65*, 104040.
[231] S. Lou, F. Zhang, C. Fu, M. Chen, Y. Ma, G. Yin, J. Wang, *Adv. Mater.* **2021**, *33*, 2000721.
[232] X. Yu, L. Xue, J. B. Goodenough, A. Manthiram, *ACS Mater. Lett.* **2019**, *1*, 132.
[233] J.-F. Wu, Z.-Y. Yu, Q. Wang, X. Guo, *Energy Storage Mater.* **2020**, *24*, 467.
[234] Y. Kim, M. Künzel, D. Steinle, X. Dong, G.-T. Kim, A. Varzi, S. Passerini, *Energy Environ. Sci.* **2022**, *15*, 2610.
[235] X. Chi, F. Hao, J. Zhang, X. Wu, Y. Zhang, S. Gheytani, Z. Wen, Y. Yao, *Nano Energy* **2019**, *62*, 718.
[236] Z. Gadjourova, Y. G. Andreev, D. P. Tunstall, P. G. Bruce, *Nature* **2001**, *412*, 520.
[237] X. Feng, P. Chien, Z. Zhu, I. Chu, P. Wang, M. Immediato-Scuotto, H. Arabzadeh, S. P. Ong, Y. Hu, *Adv. Funct. Mater.* **2019**, *29*, 1807951.
[238] W. Li, Z. Yao, S. Zhang, X. Wang, X. Xia, C. Gu, J. Tu, *Chem. Eng. J.* **2021**, *421*, 127788.
[239] Q. Li, X. Ye, H. Yu, C. Du, W. Sun, W. Liu, H. Pan, X. Rui, *Chin. Chem. Lett.* **2022**, *33*, 2663.
[240] S. Ito, A. Unemoto, H. Ogawa, T. Tomai, I. Honma, *J. Power Sources* **2012**, *208*, 271.
[241] I. Delcheva, J. Ralston, D. A. Beattie, M. Krasowska, *Adv. Colloid Interface Sci.* **2015**, *222*, 162.
[242] T. Vogl, C. Vaalma, D. Buchholz, M. Secchiaroli, R. Marassi, S. Passerini, A. Balducci, *J. Mater. Chem. A* **2016**, *4*, 10472.
[243] Z. Li, D. Young, K. Xiang, W. C. Carter, Y. Chiang, *Adv. Energy Mater.* **2013**, *3*, 290.
[244] C. Wu, P. Kopold, Y.-L. Ding, P. A. Van Aken, J. Maier, Y. Yu, *ACS Nano* **2015**, *9*, 6610.
[245] C. Jin, Y. Wang, X. Zhao, J. Jin, Z. Li, X. Qu, L. Jiao, Y. Liu, *Adv. Funct. Mater.* **2025**, *35*, 2422101.
[246] C. Wang, L. Liu, S. Zhao, Y. Liu, Y. Yang, H. Yu, S. Lee, G.-H. Lee, Y.-M. Kang, R. Liu, F. Li, J. Chen, *Nat. Commun.* **2021**, *12*, 2256.
[247] Q.-C. Wang, J.-K. Meng, X.-Y. Yue, Q.-Q. Qiu, Y. Song, X.-J. Wu, Z.-W. Fu, Y.-Y. Xia, Z. Shadike, J. Wu, X.-Q. Yang, Y.-N. Zhou, *J. Am. Chem. Soc.* **2019**, *141*, 840.
[248] K. Zhang, D. Kim, Z. Hu, M. Park, G. Noh, Y. Yang, J. Zhang, V. W. Lau, S.-L. Chou, M. Cho, S.-Y. Choi, Y.-M. Kang, *Nat. Commun.* **2019**, *10*, 5203.
[249] S. Chu, C. Zhang, H. Xu, S. Guo, P. Wang, H. Zhou, *Angew. Chem., Int. Ed.* **2021**, *60*, 13366.
[250] Z. Wu, Y. Ni, S. Tan, E. Hu, L. He, J. Liu, M. Hou, P. Jiao, K. Zhang, F. Cheng, J. Chen, *J. Am. Chem. Soc.* **2023**, *145*, 9596.
[251] X. Zhao, Y. Tian, Z. Lun, Z. Cai, T. Chen, B. Ouyang, G. Ceder, *Joule* **2022**, *6*, 1654.
[252] W. K. Pang, V. K. Peterson, N. Sharma, J.-J. Shiu, S. Wu, *Chem. Mater.* **2014**, *26*, 2318.
[253] H. Yu, S. Qian, L. Yan, P. Li, X. Lin, M. Luo, N. Long, M. Shui, J. Shu, *Electrochim. Acta* **2016**, *212*, 84.
[254] N. Peng, X. Cheng, H. Yu, H. Zhu, T. Liu, R. Zheng, M. Shui, Y. Xie, J. Shu, *Energy Storage Mater.* **2019**, *21*, 297.
[255] J. Fu, C. Wang, S. Wang, J. W. Reid, J. Liang, J. Luo, J. T. Kim, Y. Zhao, X. Yang, F. Zhao, W. Li, B. Fu, X. Lin, Y. Hu, H. Su, X. Hao, Y. Gao, S. Zhang, Z. Wang, J. Liu, H. Abdolvand, T.-K. Sham, Y. Mo, X. Sun, *Nature* **2025**, *643*, 111.
[256] Y. Nagata, K. Nagao, M. Deguchi, A. Sakuda, A. Hayashi, H. Tsukasaki, S. Mori, M. Tatsumisago, *Chem. Mater.* **2018**, *30*, 6998.
[257] Y. Jing, Y. Liang, S. Gheytani, Y. Yao, *Nano Energy* **2017**, *37*, 46.
[258] W. Ji, X. Zhang, L. Xin, A. Luedtke, D. Zheng, H. Huang, T. Lambert, D. Qu, *Energy Storage Mater.* **2022**, *45*, 680.

[259] K. Yoshida, T. Sato, A. Unemoto, M. Matsuo, T. Ikeshoji, T. J. Udovic, S. Orimo, *Appl. Phys. Lett.* **2017**, *110*, 103901.
[260] L. Duchêne, D. H. Kim, Y. B. Song, S. Jun, R. Moury, A. Remhof, H. Hagemann, Y. S. Jung, C. Battaglia, *Energy Storage Mater.* **2020**, *26*, 543.
[261] Z. Yang, M. Jin, S. Cheng, X. Ma, Z. Qin, J. Zhang, Y. Yang, Y. Guo, *J. Mater. Chem. A* **2022**, *10*, 7186.
[262] M. Jin, S. Cheng, Z. Yang, Y. Luo, Y. Guo, *Chem. Eng. J.* **2023**, *455*, 140904.
[263] L. He, H. Lin, H.-F. Li, Y. Filinchuk, J. Zhang, Y. Liu, M. Yang, Y. Hou, Y. Deng, H.-W. Li, H. Shao, L. Wang, Z. Lu, *J. Power Sources* **2018**, *396*, 574.
[264] G. Sun, C. Lou, B. Yi, W. Jia, Z. Wei, S. Yao, Z. Lu, G. Chen, Z. Shen, M. Tang, F. Du, *Nat. Commun.* **2023**, *14*, 6501.
[265] F. Han, Y. Zhu, X. He, Y. Mo, C. Wang, *Adv. Energy Mater.* **2016**, *6*, 1501590.
[266] D. H. S. Tan, A. Banerjee, Z. Chen, Y. S. Meng, *Nat. Nanotechnol.* **2020**, *15*, 170.

Gaoming Sun is currently a Ph.D. candidate under the supervision of Prof. Yanjiao Ma at the School of Chemistry and Materials Science, Nanjing Normal University. His research primarily focuses on sulfide-based solid-state batteries. Prior to his doctoral studies, he earned his master's degree from the School of Materials Science and Engineering, Nanjing Tech University, where he conducted research on electrochemical catalysis for small molecule conversion under the guidance of Prof. Jun Wang.

Yuan Ma has been a professor at Southeast University, China, since 2023. His research centers on all-solid-state battery applications and the development of next-generation battery materials for electrochemical energy storage. Before joining Southeast University, he completed a postdoctoral fellowship under the mentorship of Prof. Janek and Dr. Brezesinski at the Institute of Nanotechnology, Karlsruhe Institute of Technology (KIT), Germany. Earlier, in 2019, he earned his Ph.D. under the supervision of Prof. Passerini at the Helmholtz Institute Ulm/KIT.

Hehe Zhang received his Ph.D. degree in materials science and engineering from Xiamen University in 2023. He then joined the School of Energy and Mechanical Engineering at Nanjing Normal University as an associate research fellow. His research focuses on new electrode material preparation technology and unravelling the intricate failure mechanism of sodium/potassium-ion batteries.

Shengan Wu received his B.S. degree in Applied Chemistry (2018) and his M.S. degree in Chemical Engineering (2021) from Central South University. He obtained his Ph.D. degree in Energy Science from Kyoto University, Japan, in 2025. He is currently an associate research fellow at Nanjing Normal University. His research interests focus on advanced electrolyte systems and anode-free sodium batteries.

Shiyong Chu received his Ph.D. degree from the College of Chemical Engineering at Nanjing Tech University in 2019, and then he worked as a postdoctoral researcher and a research fellow at Nanjing University (2019–2024). He is currently working as an associate professor at Nanjing Normal University. His current interests include solid-state batteries, sodium-ion batteries, and related energy-storage materials.

Stefano Passerini Professor, is Principal Scientist at the Center for Transport Technologies of the Austrian Institute of Technology, and Distinguished Senior Fellow at Karlsruhe Institute of Technology. His research focuses on the basic understanding and development of materials for high-energy batteries and supercapacitors, with the goal to create sustainable energy storage systems from environmentally friendly and available materials and processes. He has been awarded the Research Award of the Electrochemical Society Battery Division, and nominated Fellow of the International Society of Electrochemistry (2016) and the Electrochemical Society Inc (2020). Since 2019 he is a member of the Leopoldina German Academy of Science.

Yanjiao Ma is a professor at Nanjing Normal University. Previously, she was a postdoctoral researcher at the Institute of Nanotechnology at Karlsruhe Institute of Technology (KIT), specializing in high-entropy materials for batteries and mesostructured metal oxide thin films. She earned her Ph.D. in Physical Chemistry from Helmholtz Institute Ulm/KIT. in 2019, focusing on nanostructured materials for alkali-ion batteries. Her current research interests focus on high-entropy strategies for optimizing electrode materials and electrolytes, with applications in both liquid- and solid-state battery systems.